THE UNIVERSITY OF TEXAS AT AUSTIN
CENTER FOR TRANSPORTATION RESEARCH

TECHNICAL REPORT 0-7071-1
TxDOT PROJECT NUMBER 0-7071

Evaluate Geophysical Methods to Detect Underground Voids

Loukas Kallivokas
Mingwei Cai
Tairan Li

June 2023

Published June 2024

https://library.ctr.utexas.edu/ctr-publications/0-7071-1.pdf







Technical Report Documentation Page

1. Report No. FHWA/TX-23/0-7071-1	2. Government Accession No.	3. Recipient's Catalog No.
4. Title and Subtitle Evaluate Geophysical Methods to Detect Underground Voids		5. Report Date Submitted: June 2023; August 2023
		6. Performing Organization Code
7. Author(s) Mingwei Cai, PhD candidate Tairan Li, PhD candidate Loukas F. Kallivokas, PhD, PE, Professor		8. Performing Organization Report No. 0-7071
9. Performing Organization Name and Address Center for Transportation Research The University of Texas at Austin 3925 W. Braker Lane, 4th Floor Austin, TX 78759		10. Work Unit No. (TRAIS) 11. Contract or Grant No. 0-7071
12. Sponsoring Agency Name and Address Texas Department of Transportation Research and Technology Implementation Division 125 E. 11th Street Austin, TX 78701		13. Type of Report and Period Covered Technical Report September 2020 – July 2023 14. Sponsoring Agency Code
15. Supplementary Notes Project performed in cooperation with the Texas Department of Transportation and the Federal Highway Administration.		

16. Abstract

Four geophysical methods were comparatively assessed for their ability to detect subsurface anomalies/voids, namely, Electrical Resistivity Tomography (ERT), Multichannel Analysis of Surface Waves (MASW), Ground Penetrating Radar (GPR), and Full-Waveform Inversion (FWI).

We found that: a. ERT is well-suited for detecting and localizing subsurface anomalies, but may not be able to accurately size or characterize the material composition of an anomaly/void; b. MASW is unsuitable under most realistic field conditions; c. FWI appears suitable based on computational simulations, and would likely meet the demands of field conditions, but this capability was not tested; and d. GPR's ability in anomaly detection is very limited due to depth constraints, it lacks consistency, and depends highly on operator experience; even when detection is successful, sizing and characterizing the anomaly using GPR is infeasible.

Given field realities common to most infrastructure projects, we recommend the continued, but careful, use of ERT for detecting subsurface anomalies/voids. We also recommend that future research endeavors be concentrated on a. joint-inversion and multi-physics-based methods; b. software development.

17. Key Words Geophysical methods; Subsurface voids; ERT; MASW; FWI; GPR	18. Distribution Statement No restrictions. This document is available to the public through the National Technical Information Service, Alexandria, Virginia 22312; www.ntis.gov.

19. Security Classif. (of report) Unclassified	20. Security Classif. (of this page) Unclassified	21. No. of pages TBD [Total count excl. cover]	22. Price

Form DOT F 1700.7 (8-72) Reproduction of completed page authorized

THE UNIVERSITY OF TEXAS AT AUSTIN
CENTER FOR TRANSPORTATION RESEARCH

Evaluate Geophysical Methods to Detect Underground Voids

Mingwei Cai, PhD candidate, The University of Texas at Austin
Tairan Li, PhD candidate, The University of Texas at Austin

Loukas F. Kallivokas, PhD, PE, Professor, The University of Texas at Austin

CTR Technical Report:	0-7071
Report Date:	Submitted: June 2023
Project:	0-7071
Project Title:	Evaluate Geophysical Methods to Detect Underground Voids
Sponsoring Agency:	Texas Department of Transportation
Performing Agency:	Center for Transportation Research at The University of Texas at Austin

Project performed in cooperation with the Texas Department of Transportation

Disclaimers

Author's Disclaimer: The contents of this report reflect the views of the authors, who are responsible for the facts and the accuracy of the data presented herein. The contents do not necessarily reflect the official view or policies of the Texas Department of Transportation (TxDOT). This report does not constitute a standard, specification, or regulation.

Patent Disclaimer: There was no invention or discovery conceived or first actually reduced to practice in the course of or under this contract, including any art, method, process, machine manufacture, design or composition of matter, or any new useful improvement thereof, or any variety of plant, which is or may be patentable under the patent laws of the United States of America or any foreign country.

Acknowledgments

I wish to express my appreciation to the Texas Department of Transportation (TxDOT) for supporting this research study.

I wish to acknowledge the efforts of the Research Project Manager Joanne Steele to keep us on schedule (or at least trying to). I also wish to express my appreciation for the discussions we had during research meetings with many on the TxDOT team, including Clover Clamons, Sharad Dumre, Edward Galbavy, Tracey Janus, Jenny Li, Melissa Benavides, and Nicasio Lozano. I wish to particularly acknowledge Clover Clamons for her initiative in securing the field experiment sites. I also wish to acknowledge the contributions and discussions with the TxDOT GPR team that included Ruben Carrasco, Rick Salazar, and Juan Gonzalez.

I wish to further acknowledge the support of the following graduate students who assisted us during the field experiments: they donated their time and effort, even though they were not supported by the project: Jodie Crocker (UT), Joe Vantassel (UT), Michael Yust (UT), Istiakur Rahman (U of Arkansas), Sagar Barua (U of Arkansas).

Last, but not least, I wish to acknowledge the various contributions of Professor Brady Cox (formerly of UT, and currently at Utah State University), and Professor Clint Wood (University of Arkansas). Both Brady and Clint assisted in various aspects of the project, which included the field experiments and the data processing, without being supported by the project. I appreciate very much their assistance.

Loukas Kallivokas

Table of Contents

List of Tables

List of Figures

Chapter 1. Introduction

Texas Department of Transportation (TxDOT) Project 0-7071, entitled "Evaluate Geophysical Methods to Detect Underground Voids," is aimed at the comparative assessment of the effectiveness of four methods –herein termed *geophysical methods*– in detecting subsurface anomalies, with particular focus on underground voids.

In this report, we discuss the motivation for the geophysical methods' comparative assessment, the assessment methodology that we followed, and the conclusions we reached; the report is divided in five Chapters.

In Chapter 1, we provide an overview and discuss the motivation for undertaking the present study, we review the objectives and the scope of the project, and summarize the organization of the report.

1.1. Overview

The need for the accurate characterization of the near-surface soil deposits in terms of their spatially-varying properties is of paramount importance for most, if not all, infrastructure projects. Moreover, the need arises not only at the design stage, but is continually present throughout the lifetime of the infrastructure (e.g., bridge, highway, building, etc.) that is founded on the characterized deposits, since various evolving conditions (e.g. soil erosion, prolonged droughts, etc.) may alter the composition of the deposits, requiring their recharacterization.

Failure to accurately characterize the deposits during the design stages could result in costly construction delays when voids or other weakened patches of soil are unexpectedly encountered in the subsurface during construction. Problems with undetected subsurface anomalies could also arise post-construction, and stand to impact functionality and safety: this makes imperative the *continuous*, or, at a minimum, the *periodic* monitoring of suspected weakened subsurface zones, in order to avoid costly repairs and allow for timely interventions. In central Texas, in particular, caves and sinkholes are prevalent in the limestones that exist within karst regions known as the Edwards Plateau and the Balcones Fault Zone (Kastning 1987, Hunt et al. 2014). The fact that two of the four most populated metropolitan areas in Texas (Austin and San Antonio) lie within these karst regions (Figure 1.1) that are fraught with voids and caves accentuates the need for accurate

soil characterization, since transportation infrastructure projects in these areas are often adversely affected when subsurface voids are encountered during construction.

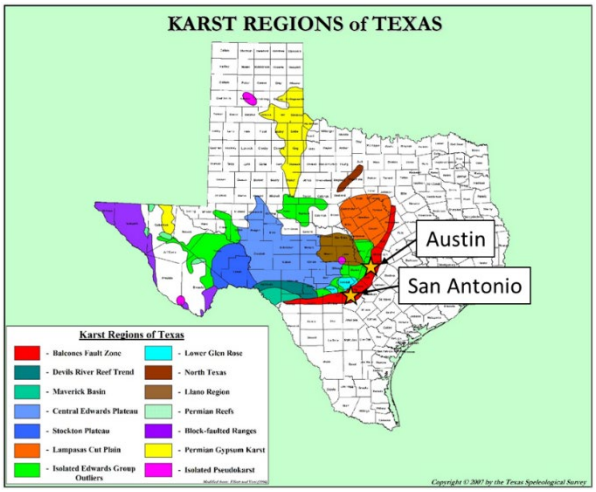

Figure 1.1: Map shows the karst regions of Texas. Note that karst geology, known to contain numerous subsurface voids and caves, exists beneath three of the top five population centers in Texas: Austin, El Paso, and San Antonio (modified from Karst Regions of Texas).

Characterization of the near-surface deposits requires that the soil deposits be described in terms of their properties. This is often, but not exclusively, achieved in terms of moduli, after the adoption of a suitable soil constitutive model. For example, under linear, elastic, and isotropic assumptions, soil can be described in terms of the pair of Lamé parameters, or the pair of Young's modulus and Poisson's ratio, or the pair of shear and compressional velocities, or other suitable descriptor pair (of which there are many). The soil properties, irrespective of the selected descriptor pair, vary in space, along any three, mutually independent, spatial directions: characterization of the deposits requires that the properties become known at, theoretically, every material point of the subsurface (infinitely small resolution), and, practically, at distances dictated by a finite, user-defined and resource-dictated, resolution.

In general, *subsurface imaging* of the near-surface deposits is the process by which material properties are assigned to every image voxel of the subsurface volume of the geologic formation of interest, following their determination by a suitable methodology.

There are several suitable methods that, over time, have been devised for subsurface imaging, commonly referred to as *geophysical methods.* The overarching goal of TxDOT Project 0-7071 is to assess the effectiveness of various *geophysical methods* in detecting *subsurface anomalies/voids*.

The term "*subsurface anomalies"* is used to refer to regions of the probed geology whose morphology and material properties depart sharply from those of their surroundings.

Detection of a subsurface anomaly/void using geophysical methods that aim at the characterization of the near-surface deposits is achieved *indirectly*, following the mapping of properties to (points in) the subsurface: for example, a zone with fairly high electrical resistivity could be considered as occupied by a void, and, similarly, a zone with fairly low shear wave velocity and high compressional velocity could be considered as occupied by highly saturated soil.

The most typical set up of a geophysical method involves a source that is used to probe the targeted formation, and an array of sensors that is used to record the response of the formation to the probing source. In general, the formation's properties are subsequently deduced from an iterative process that attempts to match the recorded responses at the sensor locations to the responses computed based on *trial (guessed)* property distributions. The associated mathematical formalism iteratively updates the trial properties until the mismatch (misfit or difference) between the recorded and computed responses is minimized (or vanishes), in which case the last set of trial properties are pronounced to be the true properties of the formation. We note that geophysical methods that rest on this iterative process have a long history: their development has been primarily fueled by the quest for the discovery of subterranean pockets of mineral resources. However, despite considerable advances in all areas of relevance to geophysical methods, from sensors to data acquisition and computational processing, subsurface imaging remains by-and-large an open research problem. This is primarily due to the inherent physical limitations that prohibit the deployment of sensors in a manner that would completely envelope the probed geologic formation, thus aggravating the inherent ill-posedness of the associated mathematical/imaging problem. In short, the inability to surround the targeted formation with sensors limits the amount of data that can be collected, and, in general, limited data cannot reliably result in a unique subsurface image,

effectively allowing many different images to appear valid/true. The described difficulty is characteristic of all inverse problems[1] – and *subsurface imaging is an inverse problem*.

In summary, to comparatively evaluate geophysical methods for the detection of subsurface anomalies/voids, as requested under TxDOT Project 0-7071, is, effectively, a comparison of the capabilities of different inverse methods for imaging the subsurface.

1.2. Project Scope and Objectives

The project's scope is delineated by the geophysical methods in consideration: of the various geophysical methods, the following four methods are reviewed in the present study:

- Ground Penetrating Radar (GPR);
- Electrical Resistivity Tomography (ERT);
- Multi-channel Analysis of Surface Waves (MASW); and
- Full-Waveform Inversion (FWI).

Each of the geophysical methods is based on different physics: GPR uses electromagnetic waves to probe; ERT uses electrical currents; and MASW and FWI use mechanical waves (also termed elastic or stress waves) to probe. It is important to note that, because of the different underlying physics, the methods image different material properties. Specifically:

- ERT images the electrical resistivity or conductivity of the probed subsurface;
- MASW images the shear wave velocity of the subsurface; and
- FWI images the compressional and shear wave velocities, or the Lamé parameters of the subsurface.

GPR is a refraction method that does not image the subsurface in terms of a specific physical property, but instead produces images of the subsurface (radiograms) where the presence of strong

[1] In the parlance of inverse problems, the described difficulty refers to non-uniqueness or solution-multiplicity.

anomalies can be identified by an experienced operator, but, usually, without material characterizations.

We note that subsurface images obtained from methods that are based on different physics cannot be directly compared to each other, unless prior correlations between the different material properties (e.g., electric resistivity versus elastic moduli/wave velocities) have already been established.

It is also important to note that the comparative evaluations are carried out under a *single-physics* hypothesis, i.e., each geophysical method is assessed for its own capability to image the subsurface, and not synergistically with another method. While it is possible, and, in fact, desirable, to combine two geophysical methods to image the subsurface, such a *multi-physics-based* framework of subsurface imaging falls outside the project's scope.

The primary objective of the proposed research is to lend clarity on the applicability and limitations of each one of the four geophysical methods, while also arriving at recommendations for the most appropriate course of action when faced with site investigations aimed at detecting the presence of voids.

We note the following limitations:

- Detection of subsurface anomalies is limited to the near-surface deposits (i.e., to depths of approximately 10 m – 30 m) that are of relevance to foundation and geotechnical engineering applications, commonly associated with infrastructure projects.
- Each of the subsurface imaging methods requires deployment of sources and sensors. While it is possible to deploy sources and sensors deep within the volume of the probed geologic formation (e.g., in boreholes), such deployment is highly site-specific and, even when it is feasible, it is usually limited in spatial extent to be of importance to the imaging. Therefore, herein, we limit the review to developments pertaining to surface-deployed sources and sensor arrays only.
- Our evaluations are limited to flat ground surfaces only. While there is no theoretical impediment to using FWI or ERT in non-flat terrains, MASW is limited to flat terrains.

Moreover, we are unaware of robust software suites that could be used for the resolution of the inverse subsurface imaging problems based on either field or synthetic data collected on anomalous ground surfaces (and the development of such software is also outside the scope of the project) using either FWI or ERT.

1.3. Methodology

We begin with a literature review, and subsequently discuss the comparative evaluation, which includes two distinct approaches, namely, numerical studies using synthetic data, and studies using field-collected data.

The numerical studies using synthetic data were conducted in two spatial dimensions for the three geophysical methods, which can, upon inversion, lead to a subsurface map of the probed material property (ERT, MASW, and FWI). Both in-house developed software as well as commercially available software were used to conduct the studies based on synthetic data. No studies involving synthetic data for GPR were conducted[2].

Field experiments using all four geophysical methods were conducted at two sites. The field-collected data were subsequently processed for two out of the four methods (MASW and ERT). The GPR radiograms were readily available and did not require further processing, and are compared against the ERT and MASW processed field data. The FWI field-collected data were not processed, since such processing requires the development of 3D FWI inversion software, which, due to the short project duration, was not possible.

1.4. Report Organization

The remainder of the report is organized as follows: Chapter 2 presents the main findings of a literature review on the four geophysical methods. Chapter 3 describes the synthetic studies. Chapter 4 describes the field experiments, their findings, as well as the findings of validation studies. Lastly, Chapter 5 includes conclusions and recommendations.

[2] Per the agreement between TxDOT and the performing agency, only field GPR studies were to be conducted; the field GPR studies were under TxDOT's purview.

Chapter 2. Literature Review

In this Chapter we review the fundamental principles governing the methodology behind each of the geophysical methods under consideration. We also survey the literature for related developments to date.

2.1. Ground Penetrating Radar (GPR)

Ground Penetrating Radar (GPR) uses electromagnetic waves to probe the subsurface. Field-deployable GPR systems typically integrate an electromagnetic wave generator, an emitting and receiving antenna, a data storage unit, and a processor (Figure 2.1).

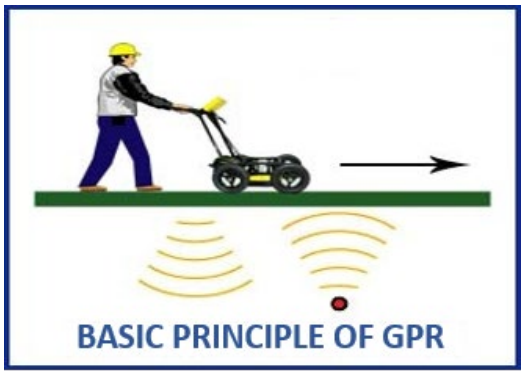

Figure 2.1: Schematic of a GPR field application (Global GPR Services, 2010)

The GPR system sends electromagnetic waves from a transmitting antenna: the waves travel through the ground at speeds that depend on the permittivity of the traversed material. The emitted wave spreads in the form of a narrow cone from the transmitting antenna, and travels downward until it hits a subsurface anomaly or a layer that has permittivity that differs from the permittivity of the overlain material. Then, part of the emitted electromagnetic wave is reflected back to the surface, where its trace is collected by the GPR system's receiving antenna (Daniels, 2000), and subsequently recorded (Figure 2.2).

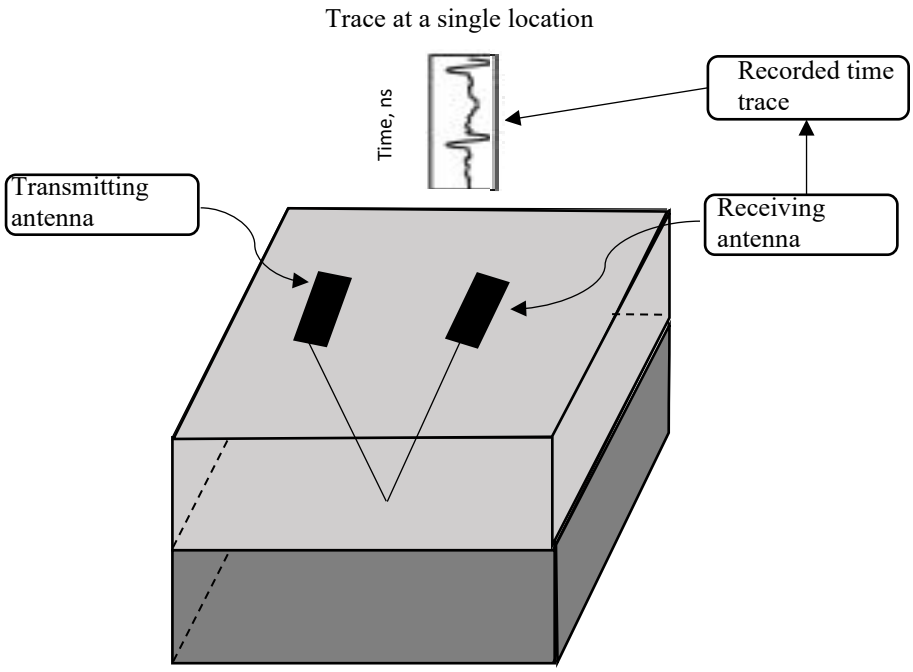

Figure 2.2: GPR pair of transmitting and receiving antennas: the wave emitted by the transmitting antenna is recorded at the receiving antenna

The recorded GPR trace exhibits two important characteristics: first, the recorded peak amplitude is smaller than the peak amplitude of the emitted pulse. This is due to the fact that wave amplitudes attenuate with distance as the wave travels away from the source because of, primarily, refraction, diffraction, reflection, and, more generally, scattering, which, in turn, result in the partitioning of the input wave energy among the reflection and scattering modalities. Thus, only a portion of the input energy, characterized by smaller amplitudes, is reflected back to the surface, where it is recorded at the receiving antenna. The second characteristic of the recorded time traces is a time lag between the transmitted and the reflected signals due to travel time.

In field applications, GPR measurements are made in either fixed-mode or moving-mode. In both modes, the transmitting and receiving antennas are moved by towing them over the ground at either discrete points along the surface, or continuously. In fixed-mode, the antennas are positioned at different points on the surface and discrete measurements are made, whereas in moving-mode the distance between the pair of antennas is kept fixed, but the antenna assembly is moved along the surface. The fixed-mode is more time-consuming, but affords greater control (e.g., antenna spacing

and orientation), whereas the moving mode allows for rapid data acquisition over broader coverage areas. In practice, it is often the case that a combination of both fixed- and moving-modes are used.

Irrespective of the preferred acquisition method (fixed-mode or moving-mode), it is important to note that using the recorded traces, GPR-based subsurface imaging could be realized based on two distinct approaches, which would, in general, result in different subsurface images:

- The recorded time traces, as the antennas move along the surface, are placed one next to the other, with the vertical axis denoting travel time (or depth if the background permittivity is known) (Figure 2.3). Then, the ensemble of the time traces, whether shown as a collection of individual traces, or interpolated to appear as a contour plot, form the most common display of GPR imaging data (radiograms). Such an image does not map a specific subsurface property: instead, it requires interpretation by experts to deduce the presence of subsurface anomalies. For example, if a hyperbola is formed in any part of the contour plot, it would be revealing a strong subsurface diffractor (i.e., a subsurface anomaly with different permittivity than that of its surroundings, whose approximate depth location could be deduced from the trace image).

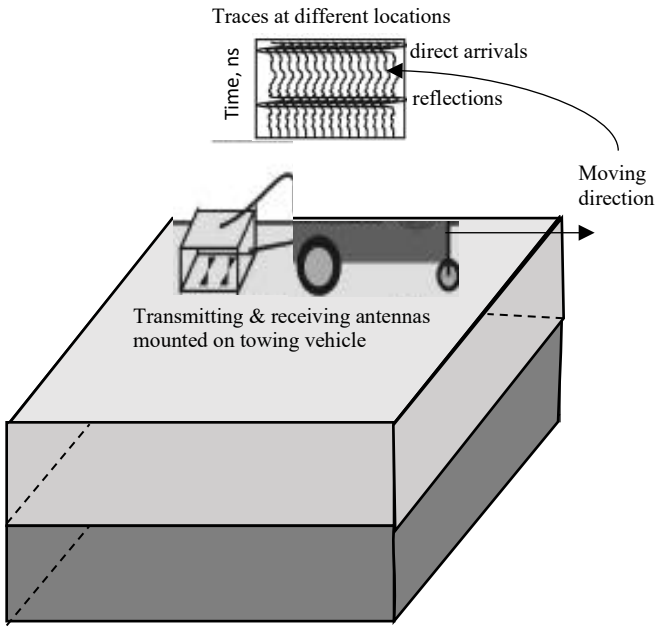

Figure 2.3: A conventional GPR trace plot consisting of staggered time traces placed one next to the other as the transmitting-receiving antenna ensemble is moving along a GPR survey line

For each line on the surface, along which the GPR antennas move, a two-dimensional plot of traces can be generated, effectively capturing reflections along a two-dimensional slice of the probed geologic formation. A three-dimensional representation of the subsurface is possible only by stitching together multiple two-dimensional slices, either parallel to each other, or perpendicular to each other, or both: for each slice, a separate GPR survey will have to take place on the ground surface. In short, the trace-based GPR imaging of the subsurface is *not* inherently three-dimensional.

We also note that, beyond denoising of the acquired traces, there is no need for any type of demanding computational post-processing to produce the trace-based maps. As such, the traced-based mapping is a very potent, yet inherently inaccurate approach.

- The recorded time traces contain information about the permittivity and the magnetic permeability of the subsurface. Therefore, they could be used in the context of a full-waveform-inversion (FWI) methodology, where Maxwell's equations are used to describe the propagation of electromagnetic waves, and the spatially-distributed permittivity and permeability are used as the inversion variables. Such an approach will readily produce three-dimensional subsurface images of the permittivity and the permeability. The full-waveform inversion approach is highly sophisticated and computationally demanding: it is almost identical to the full-waveform inversion approach for elastic waves discussed later in section 2.4, albeit tuned to electromagnetic wave propagation instead of elastic wave propagation. There are very few references in the literature of the use of GPR data to drive the FWI of electromagnetic waves for subsurface imaging; there are no references specifically targeting the detection of subsurface anomalies using FWI of electromagnetic waves.

While both of the aforementioned approaches harness the same GPR data, the resulting subsurface images could be very different: detection of subsurface anomalies using the traced-based imagery relies on subjective interpretations by experts, while the FWI-based imagery reconstructs the permittivity map of the subsurface from which anomaly detection can be done automatically, bypassing subjective judgements. It is only very recently (Luo et al., 2020) that an attempt has been made to reduce human subjectivity in the interpretation of GPR trace maps, by relying on

pattern recognition and the mining of existing databases with verified voids in known geologies; it is too early to be able to assess the success potential of such automated feature extraction tools.

Of critical importance to subsurface imaging is the operating frequency of the emitted electromagnetic pulse, which typically ranges from a few tens of MHz to a few GHz. In general, lower frequencies allow probing at larger depths, while higher frequencies limit the probing depth. Conversely, higher frequencies tend to improve the imaging resolution, allowing finer delineation of subsurface anomalies, whereas lower frequencies are less effective in imaging smaller anomalies. The probing depth may be further limited if the emitted waves meet materials of high electric conductivity along their path, since pockets of such materials would greatly attenuate the waves, making reflections off of them either imperceptible, or force them to compete with signal noise. For example, saturated deposits have higher conductivity than dry deposits, and may limit the penetration depth to as little as a few centimeters. By contrast, dry soils, limestone, etc., have lower conductivity resulting in lesser amplitude attenuation, which, in turn, allows for greater probing depth (up to 10 to 15 m). Similarly, as the soil becomes more clayey (higher water content), the depth of investigation is greatly reduced (Doolittle & Collins 1995). This can significantly affect the ability of GPR to define deep structure in clayey soils or other soil and rock types overlain by clay. In fact, the depth of investigation can be limited to less than 1 to 2 m if surficial clay soils are present (Gunton et al. 1988).

Overall, the probing depth, the minimum detectable anomaly size, the conductivity of the probed formation, and the source frequency are all interdependent. Figure 2.4 (adapted from www.usradar.com) relates the frequency range to the probing depth and to the detectable anomaly size, and clearly suggests competing trends: while lower frequencies allow for deeper probing, the maximum detectable anomaly size also increases.

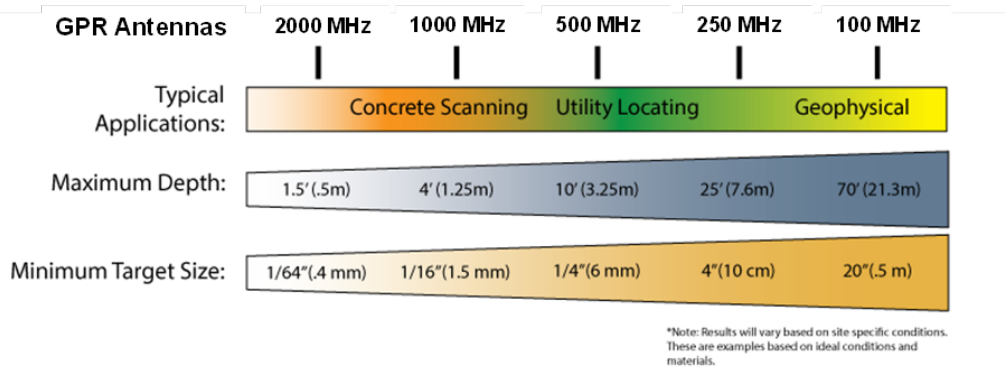

Figure 2.4: Approximate resolution and detection limits for various GPR antenna frequencies (modified from www.usradar.com)

The literature is rich in GPR field investigations. For example, GPR measurements were shown to be effective in delineating the boundaries of complex waste pits (Daniel et al., 1998). In northern Italy, GPR surveys were performed in order to detect joints and bedding planes in limestone (Pipan et al., 2003). GPR was also used in an attempt to detect pipelines, roots and smaller objects within shallow depths in urban environments (Grasmueck et al., 2016): a 500 MHz GPR survey was conducted over a 250 square meter surface area. The survey proved to be effective in detecting pipelines, but was only marginally effective in detecting roots, and other smaller, or irregularly-shaped objects (Figure 2.5). Excavation was used to validate the imaging results.

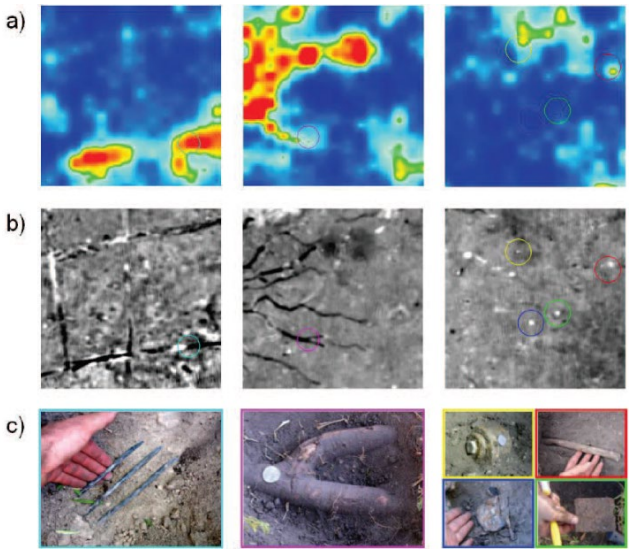

Figure 2.5: a) 500 MHZ GPR horizontal slice images; b) 3D migrated GPR images; c) Validation images (Grasmueck et al., 2016)

GPR was also used in archaeological sites in surveys aiming at the detection of buried artifacts within heterogeneous soil (Zhao et al., 2018) with reasonable success and without relying on prior information. In (Di Prinzio et al., 2010), GPR surveys were conducted to detect burrows in a levee. To improve the accuracy of the GPR survey, extensive site preparation was necessary, including surface vegetation removal, tree removal, and GPR calibration to account for previously known voids (burrows) (Figure 2.6). It was found that the probing frequency had to be adjusted to account for the irregularly-shaped burrows, and for different probing depths. In addition, the two sloping surfaces of the levee geometry greatly affected the accuracy of the measurements, while wave propagation was hindered by the conductivity of the levee's high-water content soil.

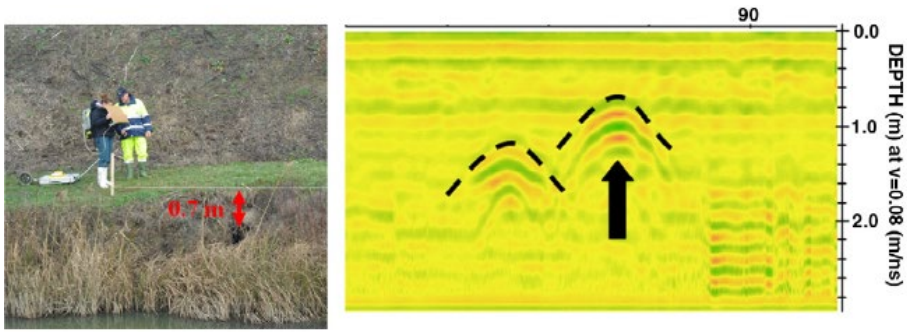

Figure 2.6: Burrow detection in levees (Di Prinzio et al., 2010)

When it comes to void detection, it is known that areas of several high-amplitude reflections in the trace-based GPR images is consistent with the location of voids. These series of high-amplitude multiples are usually attributed to the air-filled voids. The dominant characteristic of voids is the existence of a strong convex-shaped reflector at the top, combined with a low-frequency signal below it. Kofman (Kofman, 1994) attributed the high-amplitude reflections to the reverberation of the waves within the air-filled void. Thus, two questions arise: a. whether the probing frequency that causes the reverberation can be correlated to the void dimensions; and b. if such a correlation is possible, how to harness the effect for void detection. In (Kofman et al., 2006), the authors, following a series of laboratory experiments, concluded with two rules of thumb: that reverberation, and therefore the existence of strong reflections in the GPR trace data, is possible when: a. the void diameter is larger than the wavelength (in air) corresponding to the GPR probing frequency; and b. when the vertical dimension of the void is not much smaller than the horizontal dimension. However, while the conducted experiments and the provided reasoning strongly

support the conclusions, it is unclear how the observations can be used beyond interpretations. In other words, if the probing frequency can cause the reverberation for one specific void, thus resulting in a visible and easily interpreted effect in the GPR trace images, it is certain that it will have no effect for another void, effectively making its detection impossible. Thus, relying on the reverberation effect for void detection would require multiple GPR surveys, while sweeping over the entire frequency spectrum allowed by the electronics of the field antenna –a rather impractical solution.

GPR surveys were conducted by the Texas Department of Transportation – Maintenance Division, Pavement Analysis and Design Branch in at least three occasions in order to detect anomalies under the pavement. For example, GPR surveys were performed in Lufkin District along a river approach and abutment using a ground-coupled GPR (Figure 2.7).

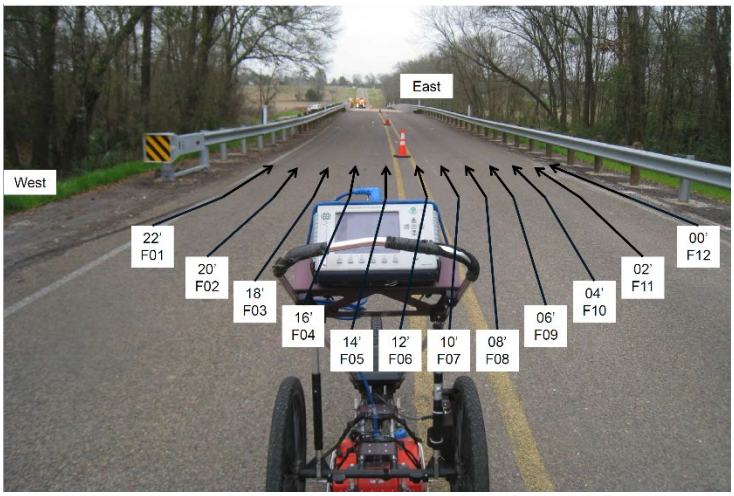

Figure 2.7: GPR survey lines, spaced 2 ft apart

The radiograms depicted in Figure 2.8 indicate the possible presence of voids.

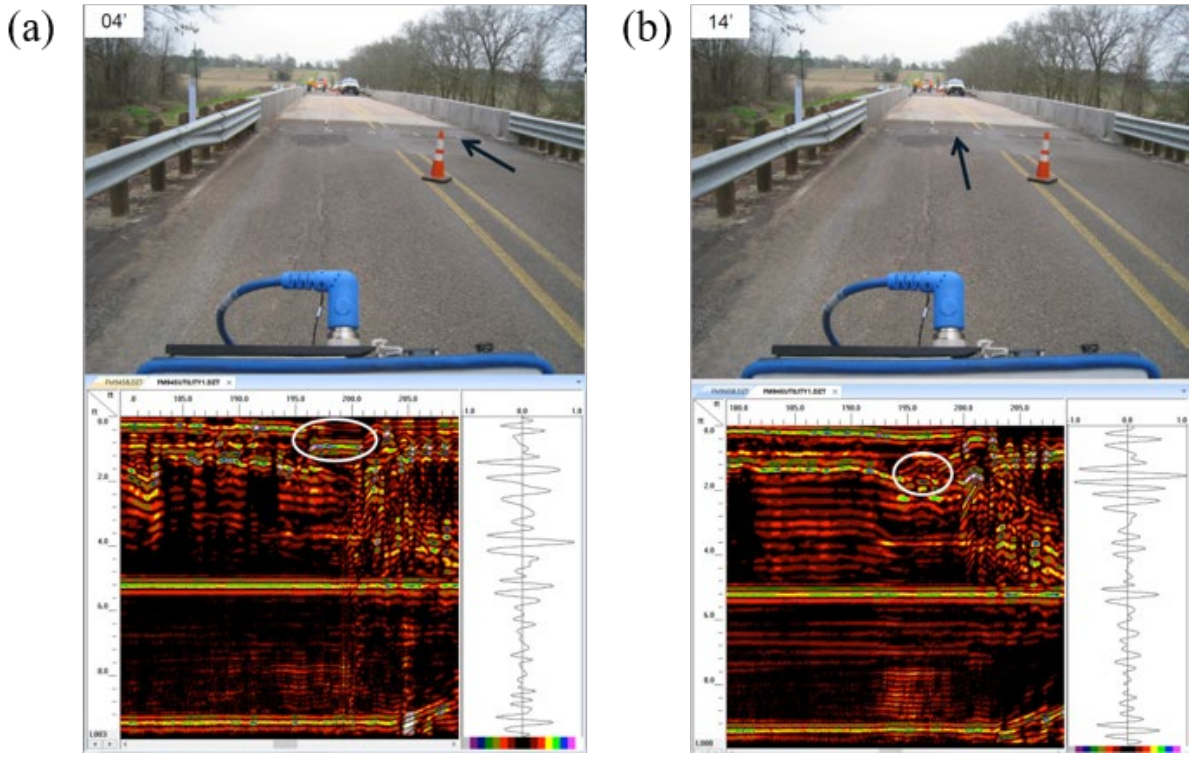

Figure 2.8: (a) Location of GPR survey 04 and associated trace image; (b) Location of GPR survey 14 and associated trace image. White circles indicate the presence of a potential void

Another GPR survey was conducted in 2016 on an interstate bridge overpass with potential settlement occurring in the embankment. The frequency of the GPR is selected as 200 MHz and 400 MHz, for detecting different area, showing in the Figure 2.9.

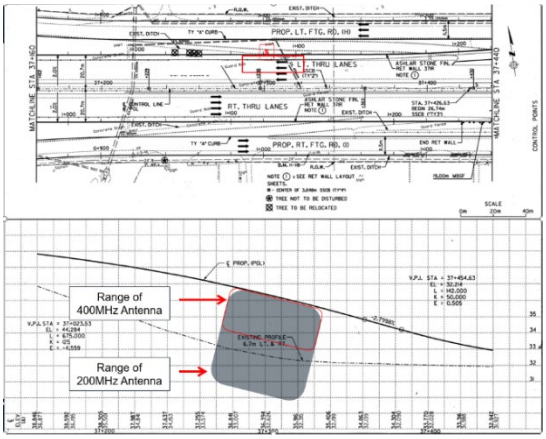

Figure 2.9: GPR survey using two different probing frequencies at 200 and 400 MHz

The GPR survey results indicate the possible location of a void or anomalous backfill, as shown in Figure 2.10; the width of the region is estimated by multiple parallel-line GPR surveys, since the trace imagery of the different surveys shows a similar negative parabola occurring at the same depth.

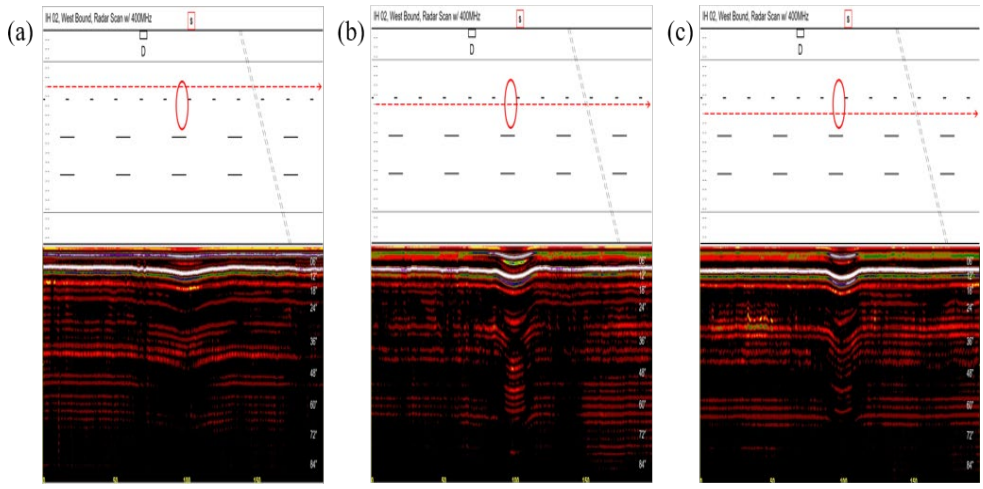

Figure 2.10: Trace plots of GPR survey using a probing frequency of 400 MHz

The conducted surveys also explored void detectability as a function of the probing frequency. Figure 2.11 shows the trace imagery resulting from two GPR surveys along the same line, which were conducted using two different antenna frequencies: it is clear that a subsurface anomaly is not detectable using the 200 MHz frequency, whereas it is detected when probing at 400 MHz.

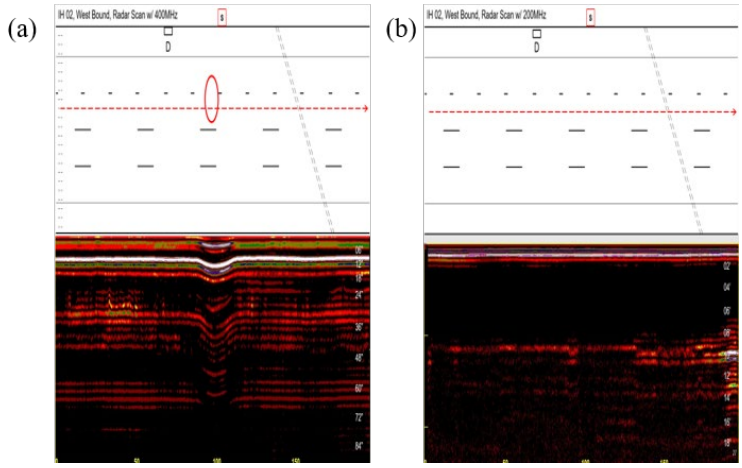

Figure 2.11: Comparison of two GPR surveys conducted using a 400 MHz antenna frequency (left) and a 200 MHz frequency (right). A strong reflection can be seen in the left figure, suggesting the presence of a void, whereas no such reflection is observable in the right figure.

It should be noted that GPR has been used in void and cave detection studies for over 20 years (e.g., Chamberlain et al. 2000, Kofman et al. 2006, Jeng and Chen 2012, Lai et al. 2018). While some studies have reported successful void detection, other studies have shown mixed results and/or failures. In a recent blind study of GPR-based void detection (Lai et al., 2018), the authors used a man-made sandy-soil test pit covering an area approximately 10 m by 20 m. The test pit contained six voids with diameters ranging from 0.6 to 1 m, at depths ranging from 0.6 to 1.6 m (i.e., relatively large voids in comparison to their depths). Seven independent contractors surveyed the site using GPR. In general, the results were not positive, with the best contractor locating three out of the six voids, and other contractors locating one or none of the voids. For example, the results from Service Provider A are shown in Figure 2.12. The colored/shaded circles are the known void locations in plan-view, while the black circles are the estimated locations of the voids: as it can be seen in Figure 2.12, all estimates were incorrect.

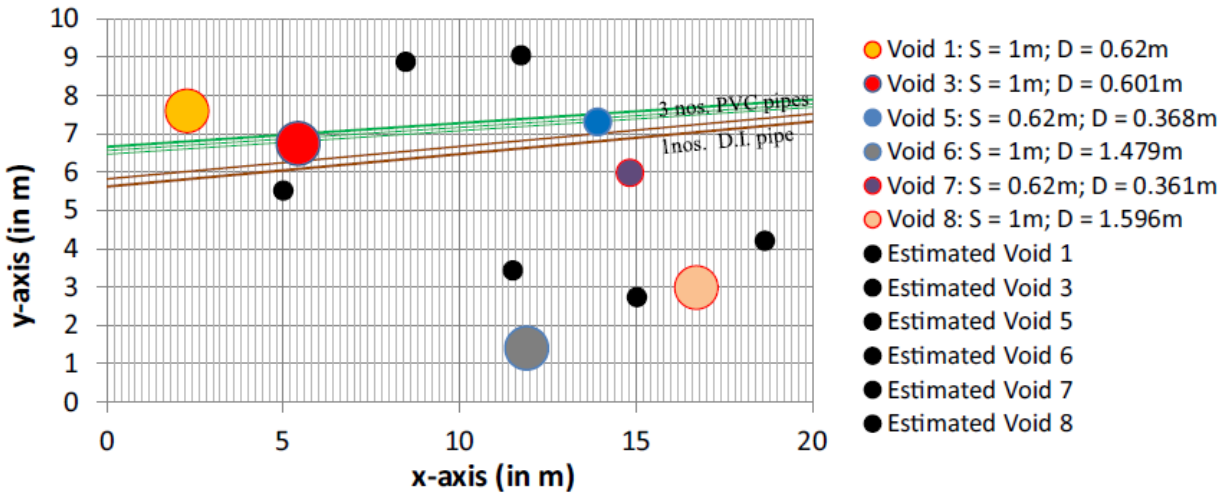

Figure 2.12: GPR void detection results obtained by Service Provider A in the Lai et al (2018) blind study. Note that this service provider located zero of the six voids correctly, while the best provider located three out of the six voids

In summary, the literature provides mixed evidence on the efficacy of Ground Penetrating Radar (in its trace-based form) as a subsurface anomaly detection method. Common observations derived from the literature survey, including limiting factors, are as follows:

- The ground surface must be flat, since the presence of surface topographic anomalies will affect the recorded signal.

- The ground surface must be dry, free of vegetation, and of other surface obstructions.
- The presence of water or of deposits with high water content, or, more generally, the presence of high conductivity materials, would attenuate the propagating waves. Any voids or other subsurface anomalies residing below the pockets or layers of higher conductivity will not be detected, effectively masked by the higher conductivity of the overlain layers.
- Ground-coupled GPR is preferred to air-coupled GPR due to additional attenuation and reflections that the air-coupled GPR introduces at the air-ground interface.
- Subsurface anomalies whose major dimension is oriented parallel to the ground surface are more easily detectable than anomalies oriented perpendicular to the ground surface.
- When detection is possible, the size of the detected subsurface void or anomaly depends greatly on the probing frequency, requiring that, at a minimum, the subsurface anomaly has a diameter at least as large as the wavelength corresponding to the transmitting antenna's frequency.
- The probing depth also depends on the transmitting antenna's frequency, with lower frequencies probing deeper than higher frequencies.

2.2. Electrical Resistivity Tomography (ERT)

Electrical Resistivity Tomography (ERT) uses the injection of currents to probe the subsurface.

The aim of the ERT is to image the subsurface in terms of the electrical resistivity of the probed geologic formation. Electrical resistivity (ρ) is a metric of a material's ability to conduct electric current. Conversely, the electrical conductivity (σ) is the reciprocal of the electrical resistivity, and it quantifies the ability of a material to resist electric current. In ERT, the differences in the electric resistivity of different materials is exploited to deduce the presence and type of subsurface anomalies.

In its simplest field implementation, ERT uses two electrodes connected to a current source (electrodes A and B in Figure 2.13) in order to inject current into the ground. Then, the voltage potential is measured at two other electrodes (electrodes M and N in Figure 2.13), also situated on the ground surface.

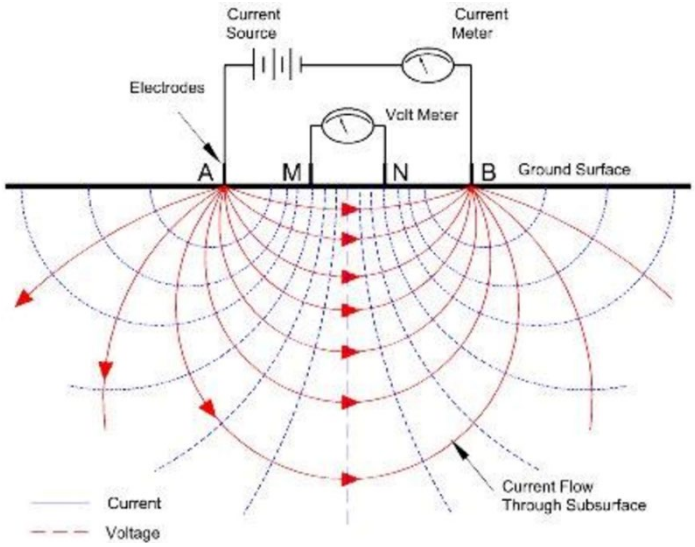

Figure 2.13: Schematic of the basic components of an Electrical Resistivity Tomography field implementation

Assuming that the subsurface is occupied by a homogeneous material, it can be shown that the subsurface's resistivity can be computed as (Samouëlian et al., 2005):

$$\rho = \frac{\Delta\phi}{I}\left[\frac{2\pi}{\left(\frac{1}{AM}\right)-\left(\frac{1}{BM}\right)-\left(\frac{1}{AN}\right)+\left(\frac{1}{BN}\right)}\right] \tag{2.1}$$

where $\Delta\phi$ is the measured potential difference between electrodes M and N, I is the intensity of the injected current, and AM, BM, AN, and BN denote the distances between electrodes A and M, B and M, A and N, and B and N, respectively.

Since, however, the subsurface is not homogeneous, Eq. (2.1) cannot account for the heterogeneity of the subsurface's resistivity. To take into account the heterogeneity, ERT appeals first to the Poisson equation describing the distribution of the potential $\phi \equiv \phi(x, y, z)$ in the subsurface; accordingly:

$$-\nabla \cdot [\sigma(x, y, z)\nabla\phi(x, y, z)] = I \cdot \delta\big(x - x_s, y - y_s, z - z_s\big) \tag{2.2}$$

In Eq. (2.2), $\sigma(x, y, z)$ denotes the spatially-varying subsurface conductivity, $\delta(x - x_s, y - y_s, z - z_s)$ denotes the three-dimensional Dirac function, and the triplet (x_s, y_s, z_s) denotes the coordinates of the current injection point. When the subsurface conductivity is known, Eq. (2),

subject to appropriate boundary conditions on the ground surface and in the far field, can be solved numerically to compute the distribution of the potential everywhere in the subsurface. Such a solution approach, i.e., when the material properties and the source term (right-hand side of Eq. (2.2)) are known, constitutes the, so-called, forward problem. However, in the imaging problem at hand, the conductivity is unknown; known, instead, is a single measurement of the potential difference between two electrodes on the ground surface. In fact, it is possible to increase the number of measurements by deploying additional electrodes on the ground surface, as depicted in Figure 2.14.

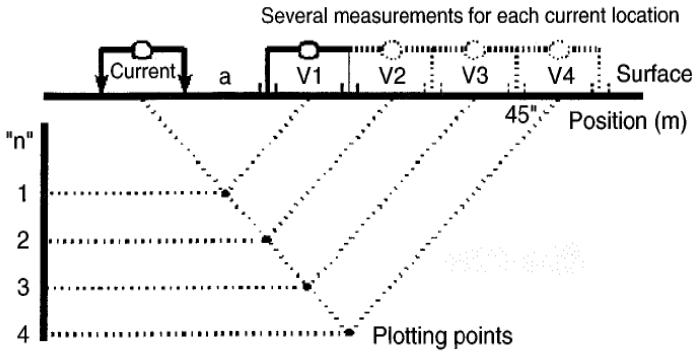

Figure 2.14: A dipole-dipole array, where several electrode pairs are used to measure potential differences for each injection pair of electrodes (Zhou et al., 2000)

Then, armed with a series of surface potential difference measurements, one seeks to uncover the spatial distribution of the subsurface conductivity $\sigma(x, y, z)$, by trying to minimize the misfit between the measured potential differences and the potential differences computed by assuming trial (guessed) distributions of the subsurface conductivity. Upon convergence, i.e., when the misfit is driven to a minimum, the converged subsurface conductivity is accepted as the true subsurface conductivity. Such a solution approach, where, with reference to Eq. (2), the unknowns become the coefficients $\sigma(x, y, z)$ of the partial-differential-equation, constitutes a, so-called, inverse problem.

Therefore, to obtain an image of the subsurface resistivity, the ERT requires the solution of an inverse problem in order to obtain the subsurface conductivity (again, the reciprocal of the resistivity), driven by discrete measurements of potential differences on the ground surface. As in all inverse problems, the initial guess, i.e., the first trial distribution of the subsurface conductivity

is of significance: Eq. (1) can be used to provide an initial estimate of the resistivity (and from it, of the conductivity) at select points in the subsurface, to seed the inversion.

Depending on the availability of electrodes, and subject to cost considerations, various array configurations can be accommodated in the field; depending on the array configuration, one-dimensional, two-dimensional, or three-dimensional ERT surveys can be conducted resulting in subsurface conductivity/resistivity images of the associated spatial dimensionality. Common array configurations include the Wenner array, the Schlumberger array, and the dipole-dipole array. The latter is the most commonly used array in field testing (Griffiths et al., 1993).

Array electrode spacing controls the image resolution, whereas the total array length controls the maximum probing depth. Typically, the smaller the electrode spacing is, the higher the image resolution, but very closely situated electrodes would degrade the measurements: typical electrode spacing is 1 m to 3 m. Similarly, the probing depth increases with the array length, with the maximum reliable probing depth limited to, approximately, 15% to 20% of the array length. It should be noted though that the array length cannot be allowed to increase uncontrollably in the hope that a greater probing depth can be achieved: the probing depth is limited due to current intensity attenuation. Typical ERT surveys include 56 to 112 electrodes, resulting in array lengths of a maximum of 100 m, and a probing depth of about 20 m to 25 m.

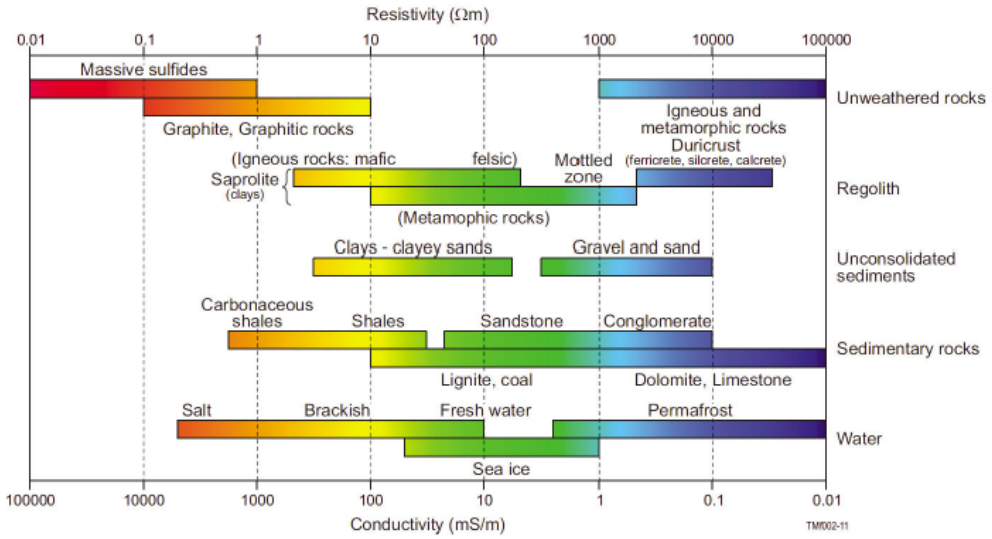

Figure 2.15: Typical ranges of electrical resistivity (Ohm-m) for earth materials (Gonzalez-Alvares et al. 2014)

Once an image of the subsurface resistivity emerges from the inversion process, to be able to identify any subsurface anomalies, it is necessary that resistivity values be mapped on to actual materials. Figure 2.15 shows one such map, where the range of electrical resistivity values for commonly encountered earth materials is shown.

We note that several factors affect the resistivity of earth material, including porosity, texture, degree of saturation, chemical makeup of the pore water, temperature, and clay content (Kaufman and Hoekstra 2001). As can be seen in Figure 2.15, the differences in resistivity values between a few soil types (e.g., clay vs. sand/gravel) and between a few rock types (e.g., shales and limestones) are strong enough to allow identification. We note though that the differences between, for example, clayey sands, shale, and even fresh water are small enough to make material identification very difficult, if not impossible, without prior information, or other corroborating observations.

We also note that to detect a patch of limestone saturated with air-filled pockets appears possible, due to the resistivity contrast between the patch and its surroundings. However, to delineate the air-field pockets within the limestone, i.e., to precisely identify voids in limestone would be challenging due to the orders of magnitude of difference between the limestone's resistivity (~10,000 – 100,000 Ohm-m) and the air's resistivity (1-3 x 10^{16} Ohm-m): such large differences in the sought properties place onerous computational demands on the inversion process, which may prove to be insurmountable with commercially-available ERT inversion software.

In general, when the subsurface anomaly is detectable based on the contrast between the anomaly's resistivity and that of its surroundings, the anomaly size must also be greater than approximately half the electrode spacing to be seen in subsurface resistivity images. Since the typical electrode spacing ranges between 1 m and 3 m, and, in some cases, as high as 10 m, the maximum detectable anomaly size ranges between 0.5 m and 5 m.

ERT has been used in void and cave detection studies for over 20 years (e.g., Cardarelli et al. 2006, Panek at al. 2010, Brown et al. 2011, Bharti et al. 2016, Deiana et al. 2018). For example, an ERT study conducted in Williamson County, Texas by AGI (AGI ERT applications) was successful at detecting one known and one previously unknown cave located in limestone approximately 6 m below the surface and overlain by approximately 4 m of clay (Figure 2.16). Furthermore, ERT was

used extensively in the vicinity of the Loop 1604 and SH 151 interchange in San Antonio as a means to detect voids in the Austin Chalk Formation (Green et al. 2013). As part of this study, 32 3D surveys were conducted and 31 potential anomalies were identified. However, of these potential anomalies, only 5 were ranked as medium-high to high likelihood of being a void/cave. This study illustrates the challenges associated with being able to confidently interpret the results of ERT-based void detection measurements. Even when ERT is able to successfully detect voids/anomalies, the locations of the anomalies may vary depending on how the data are processed. Specifically, when inverting for the resistivity/conductivity distributions, the resistivity boundaries are per force smoothed such that the exact sizes/shapes of voids may not be detected; sometimes the voids are shifted from their actual position. For example, Deiana et al. (2018) found that ERT results were able to identify the approximate locations of several known tombs, however, the precise locations could not be identified (Figure 2.17).

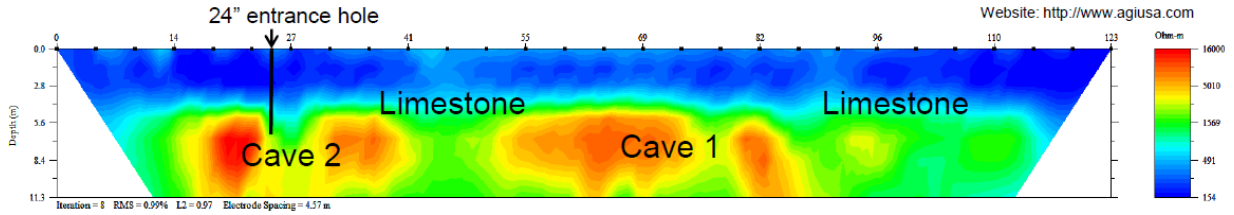

Figure 2.16: Example of a 2D ERT survey in Williamson County, Texas that was successful in locating one known cave (Cave 1) and one unknown cave (Cave 2).

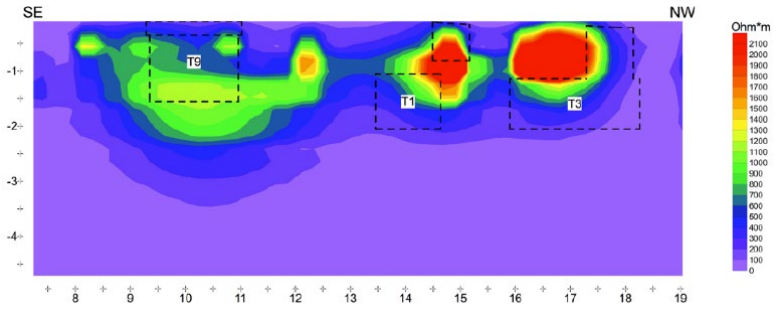

Figure 2.17: Example of a test conducted to evaluate the accuracy of anomalies detected using 2D ERT surveys. Known tomb locations are indicated by dashed lines and the locations of anomalies identified by ERT are indicated by warm colors (Deiana et al. 2018)

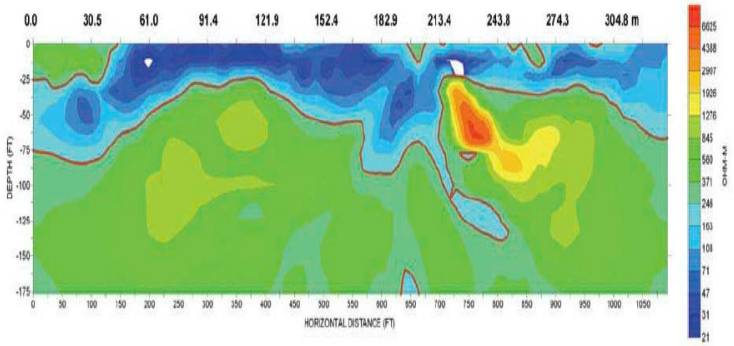

Figure 2.18: Resistivity images in a karstic formation; finger-shaped regions filled with low resistivity material help localize the sinkholes (Dobecki et al., 2006

ERT has also been used for sinkhole and cavity detection (Dobecki et al., 2006), and more commonly for the identification of the ravel zone. A ravel zone is, effectively, a previously air-filled cavity, which is subsequently occupied by loosely packed soil, transported from the overlain layers to the cavity by water. Figure 2.18 shows the sinkhole distribution in a karstic region revealed by an ERT survey.

Another notable application of the ERT technique was in the Kleśnica Valley in Poland (Kasprzak et al., 2017). A total of 8 ERT line surveys were conducted, with five of them perpendicular to the main axis of the Kleśnica Valley, and the rest aligned with the valley axis (Figure 2.19). Wenner-Schlumberger electrode arrays were used with electrode spacing of 5 m. While surface vegetation and steep slopes presented difficulties, the authors report successful void detection at three levels above the valley floor (Figure 2.19).

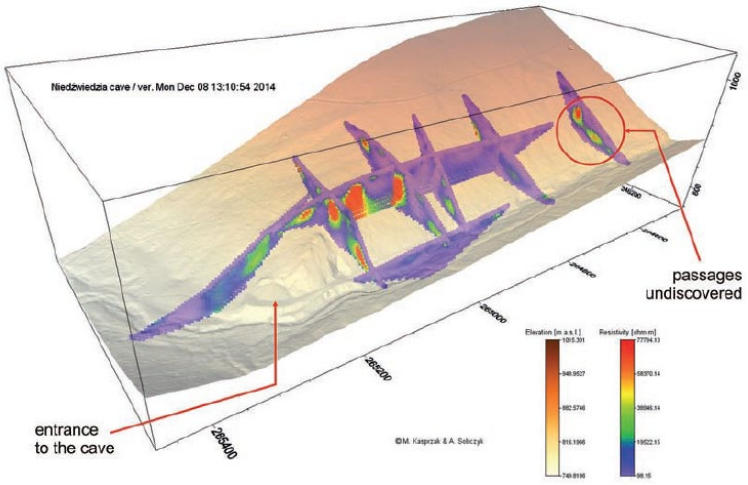

Figure 2.19: ERT-based 3D image showing detected voids within the karstic formation in the Kleśnica Valley (Kasprzak et al., 2017)

Another ERT survey was reported in a previously mined formation, which contained both known and unknown air-filled voids (Martínez-Pagán et al., 2013). Four ERT surveys were performed as part of the investigation; Figure 2.20(a) depicts the inverted resistivity distribution, whereas Figure 2.20(b) shows the delineation of all known voids/cavities. As it can be seen, in the best of cases the ERT has only approximately recovered the shape and location of the voids. For example, the depth of void C has been underestimated by about 5 m; the location of voids B and D is approximately correct, but the shape is not, while only a small portion of void A has been detected.

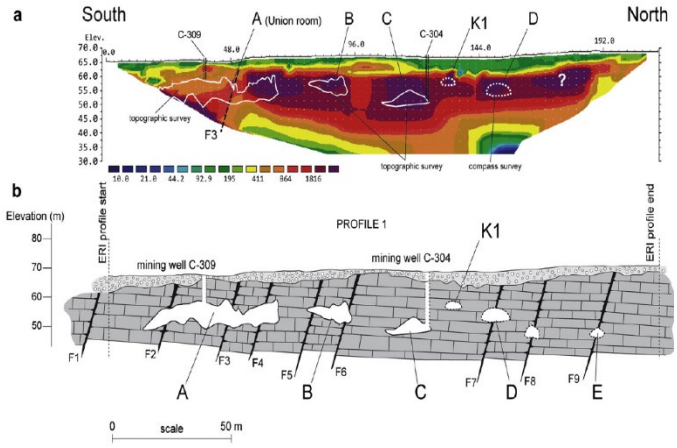

Figure 2.20: (a) ERT inversion-based subsurface resistivity image; (b) sketch of the subsurface known cavity shape and locations (P Martínez-Pagán et al., 2013)

Similar difficulties were encountered in another ERT investigation at a construction site located in a densely populated urban environment (Ungureanu et al., 2017). The goal was to detect old basements and buried pipes. A total of four ERT were conducted using 41 electrodes spaced 1 m apart. A mix of a Wenner and Schlumberger was used, in order to improve both the horizontal and vertical resistivity resolution. As shown in Figure 2.21, the ERT surveys were only partially successful in localizing a large targeted cavity (shown with dashed lines); the difficulty was attributed to the presence of moisture in the top layer, which is known to affect the measurements.

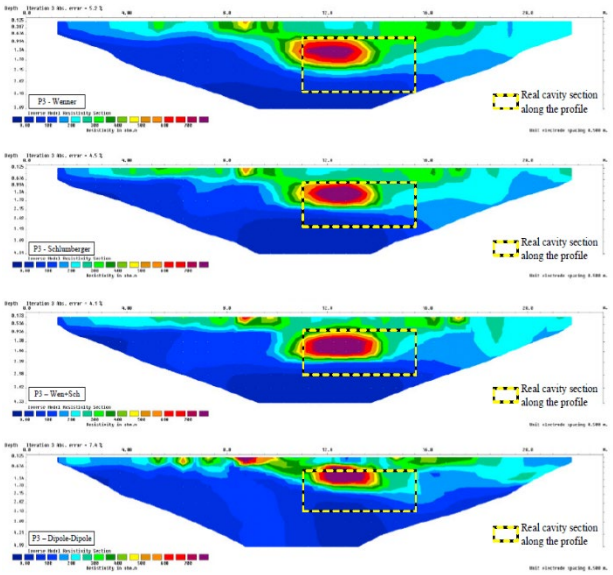

Figure 2.21: Comparison between ERT inverted resistivity image and target cavity location (Ungureanu et al., 2017)

By contrast to the above, a recently conducted 3D ERT survey in an archeological site in central Mexico was able to identify the existence of a large cavity under the Moon Pyramid (Argote et al., 2020). A total of 113 electrodes were used for the ERT survey; 27 of them were placed on the west side with a spacing 6 m; 31 electrodes were placed on the north side with a spacing of 5.5 m; 27 electrodes were placed on the east side with a spacing of 5.5 m; and 22 electrodes were placed on the south side with a spacing 5 m. The 3D ERT-inverted resistivity image (Figure 2.22) indicates the existence of a cavity that is roughly 20 m-wide and 15 m-deep from the surface, while a possible tunnel also exists on the southeastern side of the Moon Pyramid.

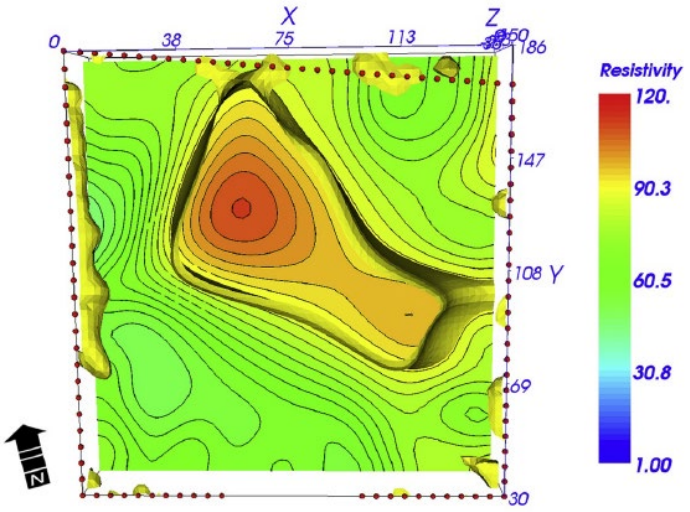

Figure 2.22: 3D ERT image of subsurface of the Moon Pyramid (Argote et al., 2020)

We note that ERT is a "static" method (i.e., the user does not have the ability to change the source to advantage) in the same way that dynamic methods (e.g., GPR, MASW, and FWI) allow by providing the user with control over the frequency content of the source/excitation. This fact alone limits the volume of the collected data, or said differently, the probing of the formation is more limited when DC currents are injected versus the probing afforded by waves. To improve on the data deficiency, which is inherent in all inversion-based approaches, so-called, *multi-physics-based* approaches have also emerged. The "*multi-physics*" term is used to imply that two methods, each based on different underlying physics, are deployed to probe the same formation. Since each method is effectively aiming at reproducing the subsurface distribution of a material property (or properties) that are different than the property (or properties) reproduced by the other method, there is need to correlate the properties to be able to map the images to real materials. For example,

when ERT and MASW are combined in a field investigation, the resistivities should be correlated with shear wave velocities to improve material identification (Carderelli et al. 2010, Martinez-Moreno et al. 2013, Deiana et al. 2018).

The combined use of different geophysical methods is the exception rather than the norm, since multi-physics-based inversion is presently at the cutting edge of inversion-based imaging developments. Examples, where the ERT is one of the two methods, are mentioned below.

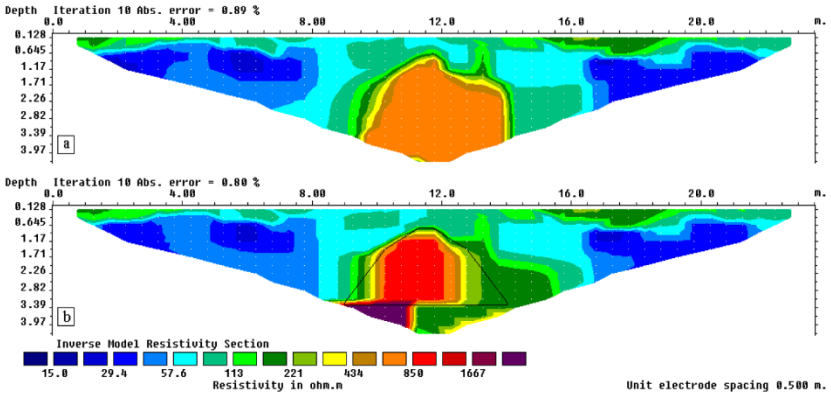

Figure 2.23: (a) ERT initial resistivity distribution guess informed by the GPR survey; (b) ERT final resistivity subsurface image showing sharp definition of the cavity and its boundary (Boubaki et al., 2011).

A cavity detection study was conducted using combined GPR and ERT surveys in a garden of the Abbaye de l'Ouye in France (Boubaki et al., 2011). A 250 MHz emitting antenna was used for the GPR survey and a total of 48 electrodes with spacing of 1 m and 0.5 m were used for the ERT survey. The GPR results indicate that it was difficult to localize the cavity due to strong reflections from its roof. However, the GPR trace-based imaging was used as a priori information for the ERT-based inversion. Figure 2.23(b) shows the resistivity subsurface image produced after the ERT initial guess was informed by the GPR imaging: the cavity's location and extend is more closely delineated by the combined use of both methods.

Another combined ERT survey with seismic refraction tomography (SRT) was conducted in a suburb of Rome aiming at the detection of a subsurface cavity: the targeted cavity was partially accessible, which offered the opportunity to validate the imaging results (Cardarelli et al., 2010). The SRT survey involved 48 geophones spaced 2 m apart, a hammer source, which was used at

17 locations, with a short spacing of 6 m. The ERT survey used 48 electrodes, spaced 2 m apart in a dipole-dipole array. Figure 2.24(a) depicts the SRT imaging, indicating a probable cavity location. Then the initial guess of the resistivity distribution was biased based on the SRT imaging, by providing a high value for the resistivity in the presumed cavity location. Figure 2.24(b) shows the ERT-based subsurface resistivity image, which has not only accurately recovered the cavity (as verified due to physical accessibility), but it also revealed two previously unknown nearby cavities.

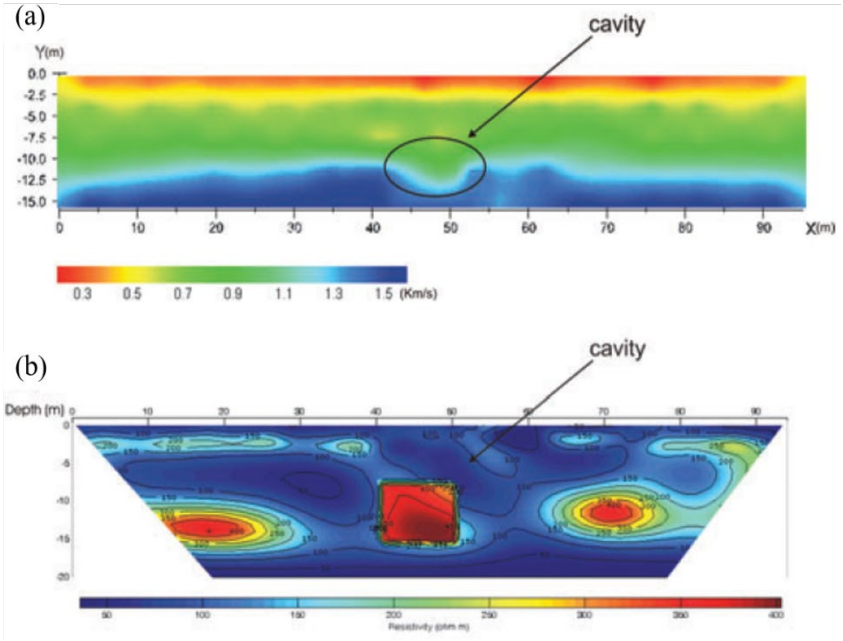

Figure 2.24: (a) P-wave velocity distribution based on SRT; (b) ERT-based inverted resistivity image, informed by the SRT inversion (Cardarelli et al., 2010).

In summary, ERT has both depth and resolution limitations, as already discussed. Moreover, the detectable anomaly size depends on the electrode spacing, and is, thus, similarly limited. ERT is probably well-suited to detect well-sized (>0.5 m) subsurface anomalies within the top 15 to 20 m, under ideal field conditions. The difficulty in uniquely identifying materials that are characterized by similar resistivity values can only be alleviated with prior information; however, such non-uniqueness does not appear to be onerous for cavity or void detection. Since ERT requires inverting for the spatially distributed resistivity, the computational demands are

significant: imaging results, depending on the complexity and dimensionality of the survey will likely be obtained in a matter of hours (not minutes) with present-day high-end workstations.

ERT is likely well-suited to address subsurface imaging in combination with other geophysical methods, since such combinations and property correlations augment the data space and improve imaging resolution, even when combined in the simplest possible manner –by using the imaging results of one method to inform the other

2.3. Multi-Channel Analysis of Surface Waves (MASW)

Multi-Channel Analysis of Surface Waves uses elastic waves to probe the subsurface.

2.3.1. MASW Introduction

In recent years, non-invasive surface wave methods have become a popular alternative to standard invasive site characterization tests, as they are relatively quick and inexpensive to perform. One such non-invasive technique, the multichannel analysis of surface waves (MASW) method (Park et al., 1999), is commonly used to provide one-dimensional (1D) and pseudo two-dimensional (2D) representations of subsurface soil layering and shear stiffness, although the accuracy of this method requires further study, particularly when subsurface irregularities (i.e., anomalies or voids) are present. To provide a comprehensive review of the ability of the MASW method to detect and resolve subsurface voids, an overview of the MASW testing procedure is provided herein, followed by a summary of various results presented in the literature.

The MASW method, as with all surface wave testing methods, generally involves three distinct steps (Figure 2.25): (1) data acquisition, which involves recording in-situ seismic wavefields with significant surface wave content; (2) data processing, which involves transforming the recorded wavefields into experimental dispersion data; and (3) inversion, which involves inverting the experimental dispersion data, from which the subsurface model (i.e., layering and elastic moduli) may be inferred. While these steps are elaborated on throughout this document, the reader may also refer to the more detailed discussions presented in Foti et al. (2018) and Vantassel and Cox (2021) regarding data acquisition/processing and inversion, respectively.

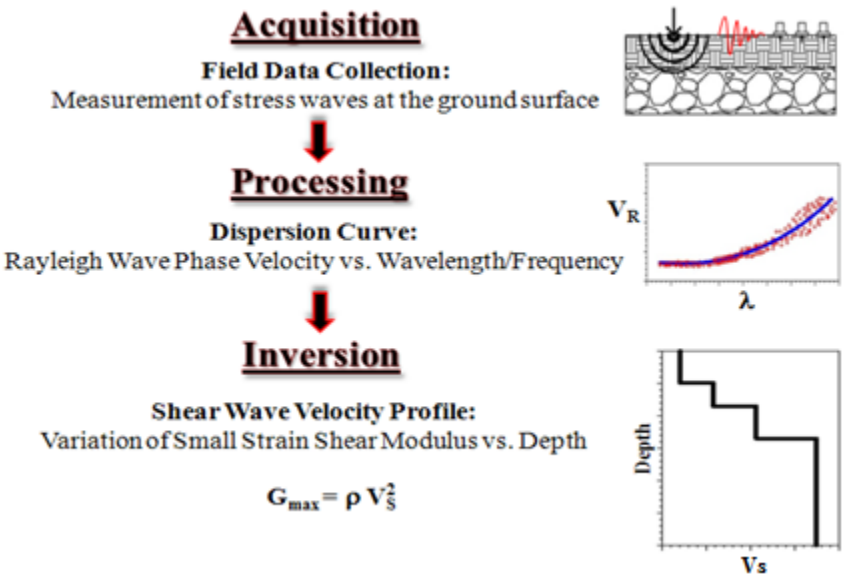

Figure 2.25: The three steps of general surface wave testing procedures (adapted from Foti et al. 2011).

2.3.2. MASW Testing Procedure

2.3.2.1. Overview of the MASW method

The MASW method (Park et al., 1999) is an active-source surface wave method that uses a linear array of geophones to record the propagation of surface waves (Rayleigh- or Love-type)[3]. MASW, as with all surface wave methods, relies on the dispersive nature of surface waves to obtain information regarding the subsurface. This dispersion, wherein a surface wave's phase velocity (V) varies as a function of its frequency (f), occurs because high frequency waves have short wavelengths (λ) that travel through shallow subsurface layers, whereas low frequency waves correspond to longer wavelengths that travel through both shallow and deeper layers. By measuring this dispersive relationship, it is then theoretically possible to use it in an inverse problem to resolve the subsurface properties (i.e., soil stiffness and layering) that cause the site-

[3] In effect, a surface wave source will generate both surface and bulk waves. The geophones record the motion that is due to all propagating waves. Thus, while the contribution due to the surface waves is dominant (e.g., 80% - 85% of the vertical surface displacement component is attributable to Rayleigh waves), it is not the only wave present in the recordings. That MASW attributes the entirety of the recorded motion to surface waves is one of the fundamental shortcomings of the method.

specific dispersion, ultimately resulting in 1D subsurface profiles representative of the material properties beneath the center of the linear array.

2.3.2.2. Data acquisition

Data acquisition for MASW involves using a seismic source (e.g., sledgehammer, accelerated weight drop, vibroseis truck, etc.) near a linear array of receivers to record actively generated Rayleigh- or Love-type waves. The array of receivers may consist of vertically oriented velocity transducers (e.g., geophones), which are used to record Rayleigh waves, or horizontal geophones oriented perpendicular to the array line, which may be used to measure Love waves. Generally, MASW arrays contain between 12 and 96 receivers, typically spaced at equal distances between 0.5 m and 5 m. However, the total length of the array and the receiver spacing may be altered depending on the goals of testing, as these parameters influence the maximum depth of investigation and the resolution of thin, near-surface layers, respectively.

As previously mentioned, the MASW method relies on the dispersive nature of surface waves to obtain information regarding the subsurface due to the relationship between a wave's phase velocity, frequency, and measured wavelength (i.e., $\lambda = V/f$). Therefore, the frequency content of a seismic source must be carefully considered given its influence on the minimum and maximum wavelengths that are measured. The minimum wavelength (λ_{min}), which occurs at the highest frequency, controls the near-surface resolution, such that the thinnest near-surface layer that may be resolved is typically assumed to be approximately $\lambda_{min}/2$. Similarly, the maximum wavelength (λ_{max}), which occurs at the lowest frequency, controls the maximum depth (d_{max}) that can be profiled, such that d_{max} is typically assumed to be approximately $\lambda_{max}/2$ or $\lambda_{max}/3$ (Foti et al. 2018). Although surface waves may be generated by a variety of sources, sledgehammers (typically weighing 5 kg to 8.5 kg) are commonly used, as they generate surface waves over a fairly wide range of frequencies (10 – 50 Hz is common). A sledgehammer can be used to generate Rayleigh-type surface waves by vertically striking a metallic strike plate, whereas Love-type surface waves are generated by horizontally striking a shear plank coupled to the ground surface with a normal force.

A final consideration for the data acquisition stage is the source location relative to the first geophone in the array line. The locations of the source must be chosen such that near- and far-field

effects may be mitigated. Near-field effects occur when waves are recorded too close to the source before they have a chance to fully develop. As a rule of thumb, one generally does not want to record surface waves that have not propagated horizontally at least half of their wavelength. When waves are recorded that have not propagated far enough relative to their wavelength, the phase velocity is underestimated, thereby corrupting the dispersion data. As such, one should not place the source too close to the receiver array. Conversely, far-field effects refer to waves that have traveled too far before being recorded. In the case of far-field effects, short wavelength/high frequency waves simply disappear from the recorded ground vibrations if the source is placed too far from the receiver array. Hence, one needs to balance near-field and far-field effects when choosing source locations for MASW testing. In general, many investigators use only one source location that is often placed too near the receiver array (perhaps 1 m to 5 m away from the first geophone), risking near-field contamination. Therefore, multiple source locations (e.g., 5, 10, 20, 30, and/or 40 m away from the first geophone in the array) are preferred as a means to identify near-field effects when performing MASW, and when possible, these locations are "reversed" by using the source at the same distances away from the opposite end of the array. At each source location, three to ten impacts, or "shots", are measured and averaged in the time domain to allow for improved signal-to-noise ratios (SNRs). Additionally, by using multiple source locations, the dispersion curves computed for each location may be averaged, allowing for the consideration of experimental dispersion uncertainty (Cox and Wood, 2011).

To illustrate this step, a typical MASW field acquisition setup used to measure Rayleigh waves is shown in Figure 2.26.

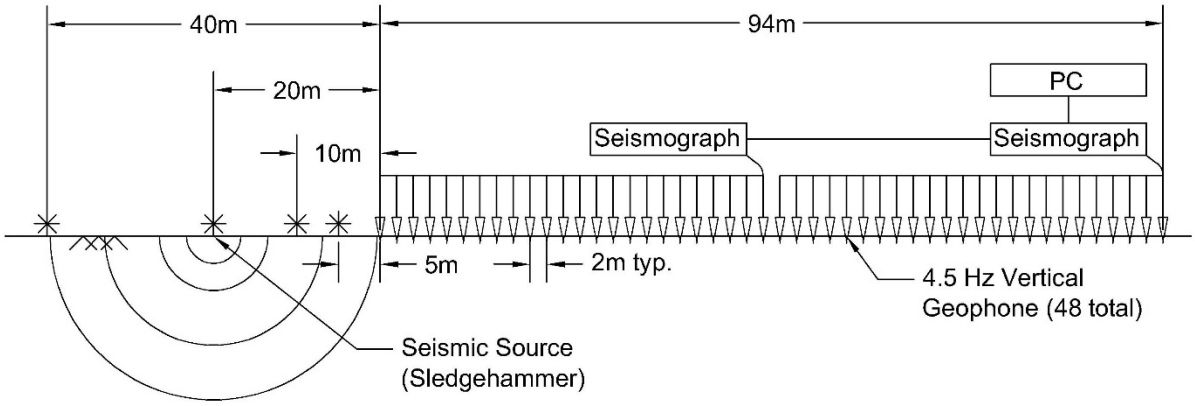

Figure 2.26: A typical MASW field data acquisition setup used to measure Rayleigh waves.

In Figure 2.26, vertical geophones are shown to denote that Rayleigh waves are being measured. In this example, 48 receivers spaced at 2 m were used for a total array length of 94 m. Note that four source locations are shown relative to the first geophone in the array line.

2.3.2.3. Data processing

After obtaining the seismic wavefields recorded by the geophones, a two-dimensional wavefield transformation is used to estimate the site's dispersion. Although multiple transformations exist (Aki, 1957; McMechan and Yedlin, 1981; Zywicki, 1999), a relatively simple two-dimensional Fourier transform, which translates the seismic wavefield from the time-offset (t-x) domain to the frequency-wavenumber (f-k) domain (Nolet and Panza, 1976), is commonly used. After applying the transformation, the dispersion data may be analyzed to identify clear trends in the data, particularly when multiple source offsets are used. By doing so, data that may have been contaminated by near-field effects or are clear outliers from the general dispersion trend may be identified and removed before attempting to develop a mean experimental dispersion curve with uncertainty bounds (Cox and Wood, 2011). It should be noted that spatial aliasing criteria should be followed, which allows for the elimination of wavelengths that are too small (i.e., frequencies that are too high) to be resolved by the array. For example, it is common to avoid using wavelengths less than two-times the receiver spacing. Further, parameters such as the total length of the array, geophone natural frequencies, and overall SNRs should be considered to eliminate low frequency/long wavelength data that cannot be accurately resolved by the array. For example, Park (2005) has suggested that d_{max} may be approximately equal to 0.5- to 3.0-times the length of the array. Historically, many have assumed that d_{max} be limited to 1.0-times the length of the array, and thus wavelengths greater than about two-times the array length should not be used (given $d_{max} \sim \lambda_{max}/2$). However, Yoon and Rix (2009) have suggested that the maximum wavelengths that may be measured depend on the array-center distance (i.e., the distance from the source to the midpoint of the array). To minimize phase velocity uncertainty (i.e., less than a 5% error on the measured phase velocity), they suggest that wavelengths greater than two-times the array-center distance should be eliminated. In either case, it is acknowledged that wavelengths greater than about two-times the array length or two-times the array-center distance may be contaminated by near-field effects and should not be used during the inversion phase. After developing the active-source

dispersion data, they may need to be resampled prior to inversion based on the quality and frequency range of the experimental dispersion data (Vantassel and Cox, 2021).

2.3.2.4. Inversion

The final step of surface wave testing is inversion, which involves finding the velocity model whose theoretical dispersion curve best matches the experimental dispersion data from the processing step. This is accomplished by first assuming a 1D candidate layered-earth model comprising a number of trial layers, each defined by a thickness (H), compression wave velocity (V_p), mass density (ρ), and shear wave velocity (V_s). This procedure is further illustrated in Figure 2.27. The model's theoretical dispersion curve is then calculated, most often using the transfer matrix forward problem (Thomson, 1950; Haskell, 1953), and compared to the theoretical dispersion data by means of a quantitative misfit value. To perform these inversions, either local or large-scale global search algorithms may be used. For local inversion algorithms, like those employed in most commercial software, a linearized least-squares inversion is performed using an initial model that is assumed to approximate the true subsurface model. The sensitivity between each model parameter and the model's misfit value is then evaluated, such that a new model can be generated with a lower dispersion misfit. In this case, the mean experimental dispersion data is targeted (without consideration of data uncertainty) and the model with the lowest misfit is retained as the single, most likely subsurface model. In contrast, global search algorithms do not require an initial starting model; instead, upper and lower limits are applied to each model parameter (forming a parameterization space), thereby allowing for a wider range of models to be investigated. For global inversion algorithms, the mean dispersion data with its associated uncertainties are targeted and all models with acceptable misfit values are retained as a means to quantify uncertainty in the inversion process. In general, global inversions use an L2 norm of residuals for a misfit value, which may or may not be normalized.

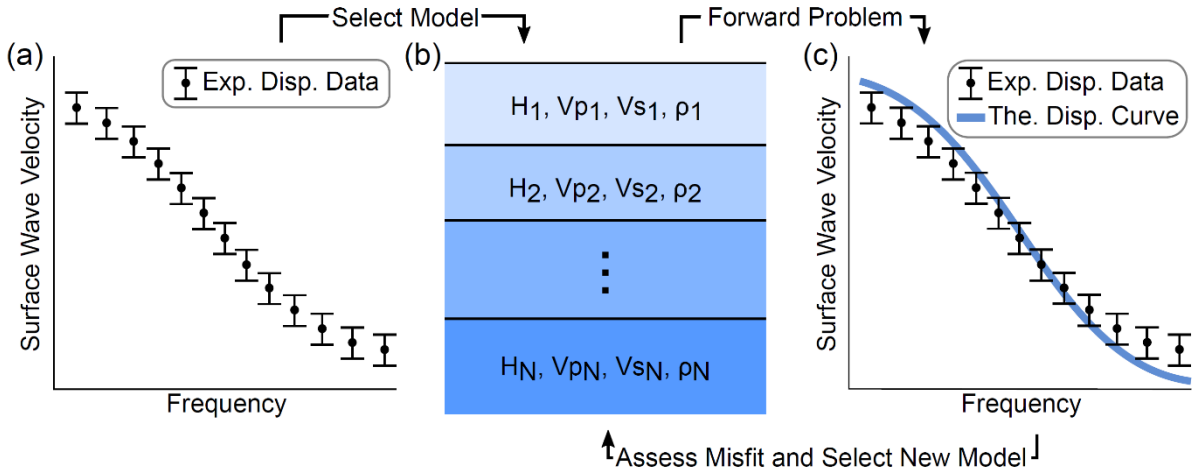

Figure 2.27: The typical inversion process, beginning with: (a) the development of the experimental dispersion data from the processing stage. (b) shows a candidate layer-earth model with each layer defined by various parameters. (c) shows the comparison of the candidate model's theoretical dispersion curve to the experimental dispersion data shown in (a). Note that the misfit calculated between the curve and data in (c) is then used to judge if a new candidate model must be selected, resulting in iteration (adapted from Vantassel and Cox, 2021).

In Figure 2.27, the inversion process is shown, beginning with the experimental dispersion data obtained during the prior data processing stage (Figure 2.27(a)). Figure 2.27(b) then shows the development and selection of a candidate layered-earth model, in which each layer is defined by H, V_p, V_s, and ρ. The theoretical dispersion curve shown in Figure 2.27(c) is then calculated using a forward problem and compared to the experimental dispersion data shown in Figure 2.27(a) using a misfit function. The misfit value is then assessed, and if the misfit is deemed too high, then the candidate layered-earth model is refined, and the process is repeated. The goal of this iterative process is to find the model(s) that best represent the experimental dispersion data, such that the best 1D V_s profile located at the center of the array line may be determined.

It is important to note that the inversion stage of surface wave testing may be rather time-consuming given the non-linear and non-unique nature of the inverse problem. Specifically, the inverse problem's non-linearity refers to the non-linear relationship between experimental dispersion data and the parameters of a subsurface velocity model. To address this issue, multiple inversions should be performed using local or large-scale global search algorithms, such that many candidate subsurface models can be tested and compared to experimental dispersion data to find

the best fit. However, the inverse problem's non-uniqueness refers to the possibility that many different subsurface models may match the experimental dispersion data equally well, resulting in multiple solutions of seemingly equal quality. To address this non-uniqueness, it is typically recommended to use global search algorithms, as they allow for a wider range of potential models to be explored, and when paired with the consideration of multiple parameterizations of the candidate model, can allow for a more complete exploration of the inverse problem's non-uniqueness. Given the complexity of inversion, only a brief introduction to this step was provided herein. For a more detailed discussion, the reader is again referred to Vantassel and Cox (2021).

2.3.3. 2D MASW

Although the three-step process described previously is inherently one-dimensional (i.e., each inversion results in the "best" 1D V_s profile located at the center of the array), this process may be extended to develop pseudo-2D (Park, 2005; Ivanov et al., 2006) and -3D images (Miller et al., 2003). Similar to standard MASW testing, the first step in 2D MASW involves data acquisition. However, in this case, many records must be obtained across a site, resulting in multiple independent 1D V_s profiles that may then be combined into a 2D V_s profile using spatial interpolation. One method of obtaining data to perform 2D MASW, the roll-along technique, is illustrated in Figure 2.28.

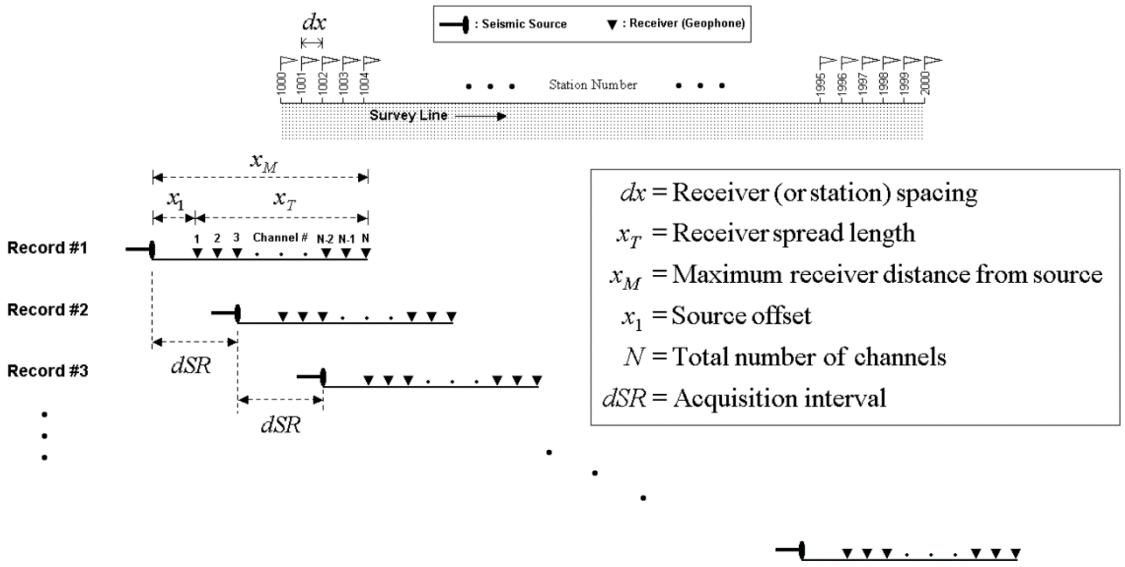

Figure 2.28: An illustration of the roll-along technique for 2D MASW data acquisition (adapted from Park, 2005).

The roll-along technique, or acquisition method, begins with a standard linear array used for MASW composed of a certain number of receivers (typically 24) each spaced at a constant distance (typically 1 m-2 m). At the first location, the source is activated, the records are transformed to dispersion data, and an inversion is performed to generate a 1D V_s profile located at the center of the array. The array is then shifted along a linear survey line by a distance *dSR*, which may also be called an acquisition interval. The same source-receiver configuration is then used with this new array location, resulting in a second set of records, which may again be used to generate another 1D V_s profile. This process is repeated until multiple sets of records are obtained across the site. Finally, the 1D profiles may be assembled based on the location of the midpoint of each corresponding array, such that the final 2D subsurface map may be generated using a spatial interpolation scheme. In a similar sense, a 3D subsurface image may also be generated using this method, although at least two non-coincident survey lines must be used. While this type of testing strategy can be used to produce pseudo-2D or -3D subsurface images, it must be stressed that it is not a true 2D or 3D approach to subsurface imaging. It should always be remembered that each 1D Vs profile contributing to the 2D/3D image represents a spatial average of the material properties beneath the extent of the array, which typically ranges from 23 m to 46 m for an array

composed of 24 geophones at 1 m or 2 m spacing, respectively. As such, the spatial averaging effect across the length of the array will tend to smear/distort relatively small features beneath the array, making it difficult to resolve true subsurface variability, even if a roll-along technique is used to profile in 2D/3D.

2.3.3.1. Use in void detection

Given the relatively quick and inexpensive nature of 2D MASW testing, it has become a popular method for use in anomaly and void detection studies. In particular, MASW has been used in a wide variety of case studies, ranging from the detection of underground structures to the detection of voids left behind by prior excavations. When using 2D MASW for detecting anomalies and voids, it is important to consider the effects that array length, receiver spacing, and source frequency content have on the resolution of the subsurface. As previously stated, typical MASW arrays may contain between 12 and 96 receivers with receiver spacings between 0.5 m and 5 m, which vary depending on the goals of testing. In general, long arrays allow for deeper profiling, whereas shorter arrays have a limited profiling depth. However, long arrays result in more horizontal averaging across the lateral extent of the array, whereas shorter arrays result in less horizontal averaging, and thus less "smearing" of the subsurface. Additionally, smaller receiver spacings allow shorter wavelengths to be resolved, leading to greater near-surface resolution, whereas larger receiver spacings increase the depth of investigation (Park, 2005; Foti et al., 2018).

When reviewing case studies on anomaly or void detection, it seems that 24 receivers spaced at approximately 1 m are commonly used for the array (Xia et al., 2004; Ivanov et al., 2009; Mohamed et al., 2013; Suto and Kristinof, 2014; Mahvelati and Coe, 2017). However, some studies reported using 24 receivers with larger receiver spacings than 1 m, while others reported using a constant 1 m receiver spacing with more than 24 receivers, depending on the specific array length needed to obtain a greater depth of investigation (Debeglia et al., 2006; Ivanov et al., 2006; Groves et al., 2011; Nolan et al., 2011; Rahimi et al., 2018). In general, it seems that 24 receivers and a receiver spacing of 1 m are preferred and typically provide reasonable data, although information about the site may result in refining these choices.

Regarding source types, relatively large sledgehammers (i.e., 5 to 8.5 kg) are typically used with a metal strike plate, although with varying degrees of success (Xia et al., 2004; Debeglia et al.,

2006; Mohamed et al., 2013; Suto and Kristinof, 2014; Mahvelati and Coe, 2017; Rahimi et al., 2018). When deeper profiling is desired, accelerated weight drops are often used (Ivanov et al., 2003; Ivanov et al., 2006; Ivanov et al., 2009; Ivanov et al., 2016; Nolan et al., 2011; Sloan et al., 2015). While most studies utilized either sledgehammers or accelerated weight drops, the reported source offset locations varied significantly in the literature. Typically, the nominal source offset (i.e., the nearest source's location relative to the first receiver) was chosen based on the desired investigation depth. Most studies opted to use a single source offset placed at a distance ranging from approximately 5 to 20 m (Xia et al., 2004; Ivanov et al., 2006; Mohamed et al., 2013; Sloan et al., 2013; Suto and Kristinof, 2014; Sloan et al., 2015; Ivanov et al., 2016; Mahvelati and Coe, 2017), although in some cases, multiple source locations were used to mitigate near-field effects that may have occurred if the nearest source offset was poorly chosen. In these cases, either two offsets were chosen to represent a near-offset and far-offset (Ivanov et al., 2009; Ismail et al., 2014), or more than two offsets spaced at various distances were selected (Groves et al., 2011; Rahimi et al., 2018).

Although detailed descriptions regarding the data acquisition step are frequently reported in literature, details regarding the data processing or inversion stages are rarely provided. In general, commercial software, such SurfSeis or WinSeis, are cited for use in data analysis (Ivanov et al., 2003; Xia et al., 2004; Ivanov et al., 2006; Nolan et al., 2011; Mohamed et al., 2013; Ismail et al., 2014; Suto and Kristinof, 2014; Sloan et al., 2015; Ivanov et al., 2016) and are further used to perform inversions and to provide subsurface images. Given the level of reported detail of many of these subsurface images, it is likely that the inversions were performed using trial models with a significant number of relatively thin layers. This is often accomplished by using fixed-thickness layers (FTL), each with a thickness of 1 to 2 m, or layers that gradually increase in thickness as depth increases. The presumption is that when relatively thin layers are used during inversion, this should allow for the resolution of smaller subsurface features/anomalies. However, as discussed below, it is likely that this procedure actually results in relatively poor resolution of the subsurface due to the highly non-unique nature of inversions performed with many thin layers. It should also be noted that the inversions performed for each distinct array location must use the same number of layers in order to allow for spatial interpolation.

2.3.4. Examples in Literature

Despite the popularity of 2D MASW, the application of MASW to the detection of voids and subsurface anomalies has not been rigorously evaluated, as a variety of successful and unsuccessful results have been presented in literature. For example, Xia et al. (2004) attempted to use MASW to profile a site in which a collapse occurred under a drainage feature in Maryland. The drainage feature, which was a man-made subsurface drain system, consisted of a pipe installed in mostly horizontally stratified sandy and clayey silts. After the collapse occurred, a backfill of coarse sand and gravel was used to fill the resulting void, although it was unknown if more voids were present in the surrounding area. Because the depth to the drainage tunnel was approximately 13.5 m, the desired maximum profiling depth was chosen to be 15 m, and five survey lines were placed around the collapse based on accessibility. From these five survey lines, one line in particular (Figure 2.29) was placed across the collapse, thereby allowing for the identification of the general void area shown at a depth of 12 m between Stations 46 and 52. Despite noting that their data contained relatively large amounts of noise, they suggest that the identification of the relatively large void (approximately 18 m long and 6 m wide) was possible through the use of multiple survey lines, and thus 2D MASW may be successfully used when attempting to identify subsurface voids or anomalies. A critical review of the 2D image shown below raises the question, if the location of the void had not been known a priori, would the image truly have been interpreted to identify a void/collapse feature between stations 46 and 52? Or, does the anomaly at a depth of 10 m near station 25 represent a void? This example illustrates that many researchers have claimed to be successful at identifying known voids, but the evidence is often not strong and leaves one to wonder if they would have been successful without prior knowledge of the void location?

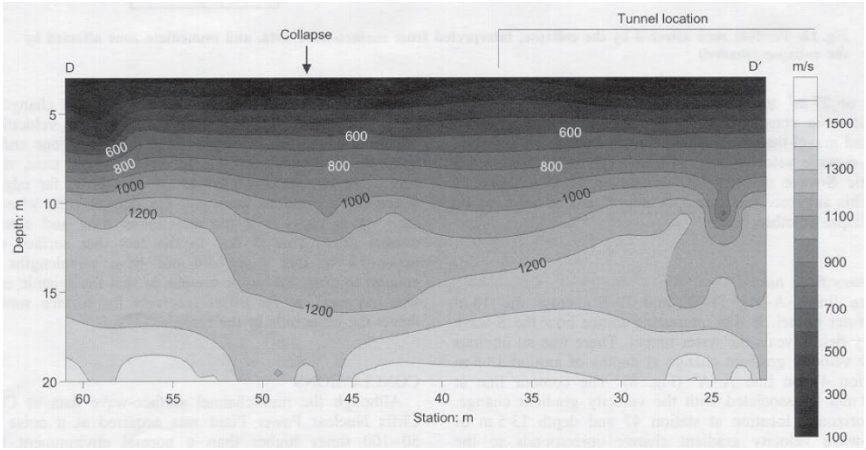

Figure 2.29: A 2D shear-wave velocity map/image of the subsurface described by Xia et al. (2004). Note that between Stations 46 and 52 and at a depth of approximately 12 m, a relatively low velocity zone may be identified, which corresponds to the known location of the collapse.

Similarly, Sloan et al. (2015) used MASW with the roll-along approach to investigate potential voids or structurally weak zones around a pipeline in west Texas. In this case, they attempted to use MASW to identify subsurface voids that may not have yet fully reached the ground surface (i.e., sinkholes), and to additionally estimate the size of voids that were visible at the surface. Four 1.1 km-long survey lines were used in parallel with horizontal offsets of 10 m between arrays to obtain subsurface images across the site. In these images, low-velocity zones of variable size were identified at the near-surface (i.e., top depths around 4 m). For example, one MASW section (Figure 2.30) shows a low-velocity zone between Station 17000 and 17020 at a depth between 4 and 8 m. Directly above this area, another zone is seen to have lower V_s overall than the surrounding areas, indicating a sinkhole may be present. Because of these results, probing was conducted at this site and a void located approximately 30 cm below the surface was found, which revealed a sinkhole was present, albeit much closer to the near-surface than the velocity profile suggests. Therefore, despite noting that their data were relatively noisy due to nearby fracking, they concluded that it was still possible to identify locations of low-velocity zones (i.e., voids) across the site, but suggested that these images be used to identify potential zones that require further investigation through the use of invasive probing methods. The image shown in Figure 2.30 further supports this assertion, as although it was used to describe a successful detection of a void, the image suggests a much deeper void than actually present.

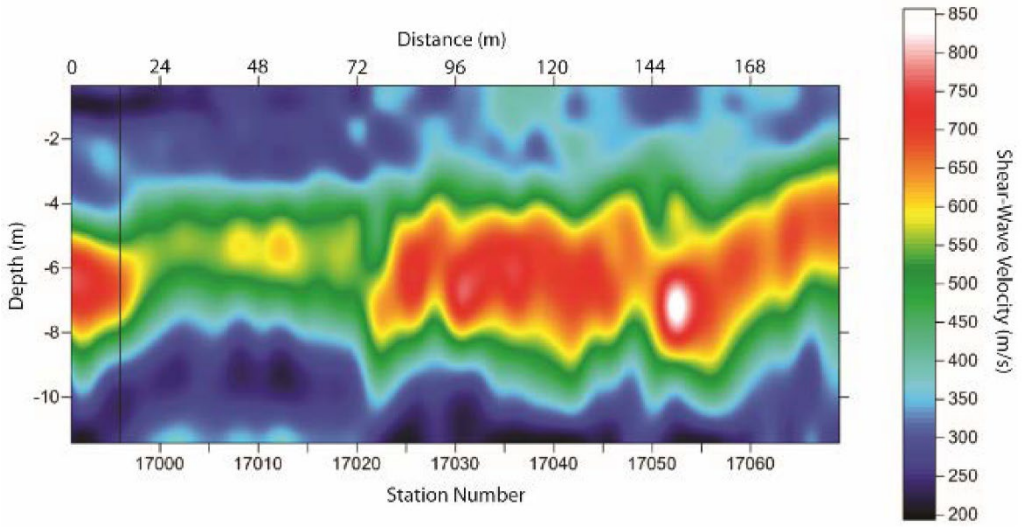

Figure 2.30: A 2D velocity profile of the site investigated by Sloan et al. (2015). Note that a low-velocity zone is present between Stations 17000 and 17020 with a sharp decrease relative to the surrounding material between 4 and 8 m depth. At this location, a sinkhole located 30 cm below the ground surface was found while probing.

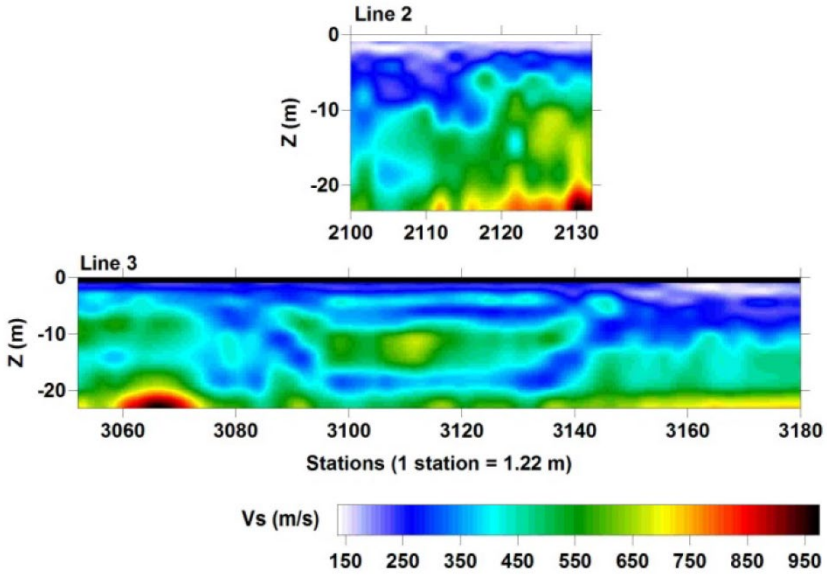

Figure 2.31: A set of 2D velocity profiles for the Galena, Kansas site study conducted by Ivanov et al. (2016). In the top image (Line 2), the authors note a dipping boundary at Station 2115 at a depth of roughly 10 m that was later associated with a low-velocity anomaly between Stations 2102 and 2115 at a depth of 7.5 to 10.5 m. In the bottom image (Line 3), the authors note the location of an old mine tunnel is indicated by a low-velocity anomaly present between Stations 3095 and 3140 at a depth of approximately 17 to 20 m.

The findings of Ivanov et al. (2016) also revealed that using MASW with the roll-along approach allowed for the detection and delineation of voids at a mining site in Galena, Kansas. In this case, both MASW and the backscatter analysis of surface waves (BASW) method were used to obtain subsurface images up to a depth of approximately 25 m. However, they noted that the MASW method alone did not allow for the resolution of potential voids; rather, information from both methods was required to develop a comprehensive subsurface profile, thus suggesting that MASW should be used with other methods to accurately identify and resolve voids. The 2D V_s profiles provided in their report are shown in Figure 2.31. In the case of Line 2, a low-velocity zone identified by a strong contrast with the surrounding material was noted at a depth of approximately 10 m near Station 2115. Although this contrast may seem just as likely to be the result of natural subsurface heterogeneity, a large anomaly was later identified between Stations 2102 and 2115 at a depth of 7.5 to 10 m using the BASW method. When viewing Line 3, a low-velocity zone is shown between Stations 3095 and 3140 at a depth of 17 to 20 m. In this case, the anomalous zone was found to correspond to the location of a mine tunnel, which was determined using mining schematics. However, the authors did not support this assertion using BASW, but instead mention the possible use of drilling to further confirm these results. There are obviously other locations in the Line 2 and Line 3 that could have also been interpreted as likely voids. For example, consider the low velocity circular anomaly located at approximately 20 m deep near station 2105. While not identified as a void by Ivanov et al. (2016), one might reasonably infer that from the 2D Vs

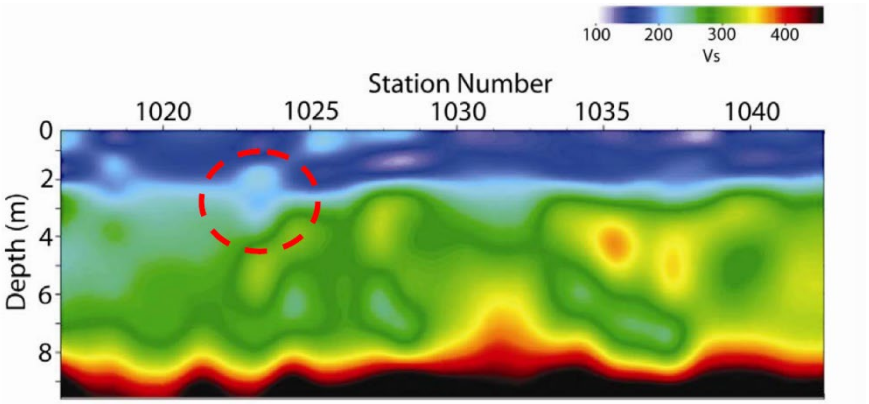

Figure 2.32: A 2D velocity profile of the site investigated by Sloan et al. (2013). Note that the red circle indicates the location of a 1.25 m by 1.25 m tunnel located 3 m below the surface that was created for the study, which can be identified by the low velocity zone surrounded by a high velocity "halo".

image. However, it is also possible that it is not an actual soft zone/void and only an artifact of the inversion.

To test the accuracy of the MASW method in detecting voids, Sloan et al. (2013) created a 1.25 m by 1.25 m tunnel at a shallow depth (i.e., a top depth of 3 m) and used both refraction and MASW testing to image the subsurface. While they were able to identify the tunnel as a low-velocity zone surrounded by a high-velocity "halo" (Figure 2.32, station 1023), the authors note that confidence in this interpretation may be attributed to having prior knowledge of the tunnel's location and size, as the subtle changes in velocity seen in the resultant subsurface profile could be easily misattributed to standard subsurface heterogeneity. Furthermore, the top depth and size of the anomaly shown in Figure 2.32 are not very accurate regarding the true, known size of the tunnel, and given that the actual tunnel was filled with air, a much lower V_s is expected for the anomaly than what was actually resolved (i.e., $V_s \sim 200$ m/s). Additionally, a similar low-velocity zone, though not quite as distinct, is noted around Station 1032 at a depth of about 2 m, but this was not indicated as a tunnel or void. While the authors indicate that the buried tunnel was located successfully using 2D MASW, one could also argue that the tunnel was not accurately resolved in terms of its depth, size, or velocity/stiffness.

Guidelines for the good practice of MASW, and surface wave analysis methods can be found in Foti, et al 2018. Given MASW's underlying assumptions, the detection, localization, and material determination of an anomaly or void of limited extend appears to contradict the fundamentals of MASW, as well as "good practice" recommendations, making detectability possible only under very particular circumstances of relatively large and relatively shallow anomalies. Thus, care must be taken when attempting to use MASW to detect and resolve anomalies.

2.4. Full-Waveform Inversion (FWI)

Full-Waveform Inversion (FWI) uses elastic waves to probe the subsurface.

2.4.1. FWI Overview

The aim of the FWI is to image the subsurface in terms of its elastic properties. In effect, the soil is assumed to behave as a lossless (no material damping) linear elastic isotropic and heterogeneous solid, characterized by spatially varying mass density $\rho(x, y, z)$, shear wave velocity $V_S(x, y, z)$

and compressional wave velocity $V_P(x, y, z)$. In fact, the last two material properties can be equivalently replaced by any number of elastic property pairs: for example, one can use Young's modulus and Poisson ratio, or the pair of the Lamé parameters $\lambda(x, y, z)$ and $\mu(x, y, z)$, or the pair of the bulk modulus and shear moduli, etc.

In principle, for a complete characterization of the subsurface, all three quantities (mass density and the pair of elastic parameters) must be obtained. However, inverting for three spatially distributed parameters is a challenge that remains unsolved to present day. In fact, inverting even for two spatially distributed parameters in three dimensions is a daunting task that demands the deployment of state-of-the-art algorithms and computational resources. To place the task in perspective, consider that in the methods reviewed thus far, ERT is the only one that comes close: a 3D ERT requires inverting for the electric conductivity of the subsurface (i.e., of only one spatially varying material parameter, compared to a minimum of two elastic parameters in the FWI case).

To understand why FWI, and related inversion processes, are computationally and algorithmically challenging, consider that to be able to image the subsurface below a ground surface area of 100 m x 100 m, at a depth of about 30 m, there is need to invert for the elastic properties at approximately 10 million points, resulting in twice as many inversion variables (20 million elastic properties). This is not equivalent to having to solve 20 million equations, which could be easily handled with today's algorithms and computational hardware: rather, for each inversion iteration, and there will be hundreds or thousands of iterations, two time-dependent forward problems involving anywhere between 500 million to one billion equations would need to be solved. This is computationally challenging.

2.4.2. FWI methodology

The FWI geophysical method comprises stages similar to the MASW: a field testing procedure to collect data, an intermediate stage to primarily denoise the data in preparation for inversion, and the inversion stage that would eventually lead to the subsurface image.

Field testing requires sources and sensors: again, similarly to MASW, a variety of sources could be used to impart a dynamic excitation on the ground surface, whereas an array of geophones deployed on the ground surface is used to record the time traces of the soil's response to the

excitation (Figure 2.33). The geophone array is usually deployed on a grid, with the spacing determined primarily by equipment availability and the intended area/volume coverage: in general, the denser the array, the better the image resolution. Either single-component, or three-component geophones can be used: preference is always given to geophones that could lead to recordings of all three components, but the method can accommodate single-component recordings as well.

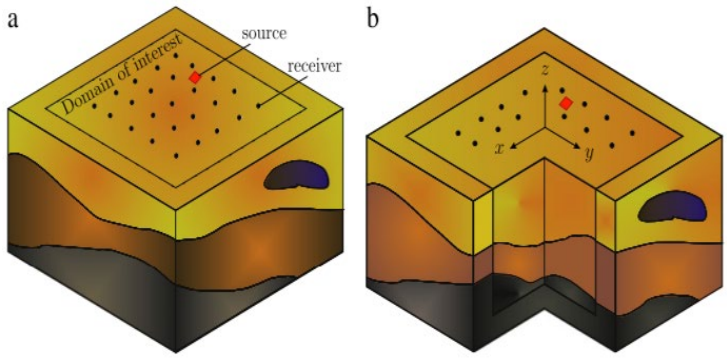

Figure 2.33: (a) and (b): schematic of array and source deployment on the surface of a probed geologic formation for FWI purposes

We note that the imparted load must also be recorded, and its point of application should ideally be within the area defined by the geophone array. A flat terrain is preferred, but the method is not constrained by topographic surface anomalies.

Following the application of the load, both surface and bulk waves are generated: the geophones record the resulting motion, which consists of contributions from direct arrivals (surface waves, P waves, S waves, the head wave) and of contributions from waves reflected by the heterogeneity of the subsurface (layer interfaces, subsurface anomalies, etc.). In other words, the geophones record the complete waveform sensed at the geophone location: it is the full waveform that is exploited for inversion purposes –thence the name of the methodology.

Following standard signal denoising and averaging procedures, the time traces of the geophone records and of the load are subsequently used for inversion. The process follows concepts already discussed in the context of the ERT: a misfit functional is defined as the difference, in the least-squares sense, between the recorded (measured) time traces at the geophone locations, and the

computed response at the same locations based on trial property distributions, subject to the equations describing the underlying elastic wave propagation physics. Stated succinctly:

$$\min_{\lambda,\mu} \mathcal{J}(\lambda,\mu) = \frac{1}{2}\sum_{j=1}^{N_r} \int_0^T \int_{\Gamma_m} (\mathbf{u}-\mathbf{u}_m)\cdot(\mathbf{u}-\mathbf{u}_m)\delta(\mathbf{x}-\mathbf{x}_j)\mathrm{d}\Gamma dt + \mathcal{R}(\lambda,\mu)$$

where $\mathcal{J}$ is the objective function, N_r is the total number of geophones, T is total observation time, Γ_m is the ground surface, $\mathbf{u}$ is the time trace of computed displacement vectors at the geophone locations based on trial property distributions, $\mathbf{u}_m$ is the time trace of the recorded displacement vector, $\delta(\mathbf{x}-\mathbf{x}_j)$ is Dirac delta function, and $\mathcal{R}(\lambda,\mu)$ is a regulation term aiming at filtering out unphysical property distributions. Further details can be found in related publications from our group.

2.4.3. FWI synthetic and field studies

FWI has been successfully used to image the near-surface deposits under conditions of arbitrary heterogeneity. In fact, the world's first FWI-based imaging was reported by a University of Texas at Austin team led by Professor Kallivokas in 2013. Specifically, we used FWI to image a site at Hornsby Bend in Austin, Texas: Figure 2.34 show the P-wave and S-wave velocities distributions at a 2D cross-section of the site, extending 200 m horizontally and 48 m in depth (Kallivokas et al., 2013).

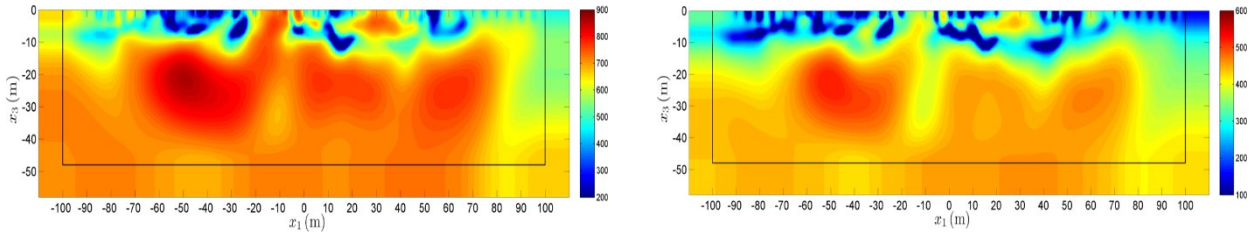

Figure 2.34: FWI imaging at the Horsby Bend site in Austin, Texas. P-wave velocity (left), S-wave velocity (right). Notice the weak zones depicted in both the P- and S-wave plots near the surface (shown in blue in the top 10 m). Notice also the finger-like softer zone developing in the middle of the cross-section extending to a depth of 35 m.

Subsequently, in 2015, our team successfully imaged another site at the Garner Valley in California, where FWI was used to obtain the P- and S-wave velocities of a 66 m x 68 m x 40 m formation, as depicted in Figure 2.35 (Fathi et al., 2016).

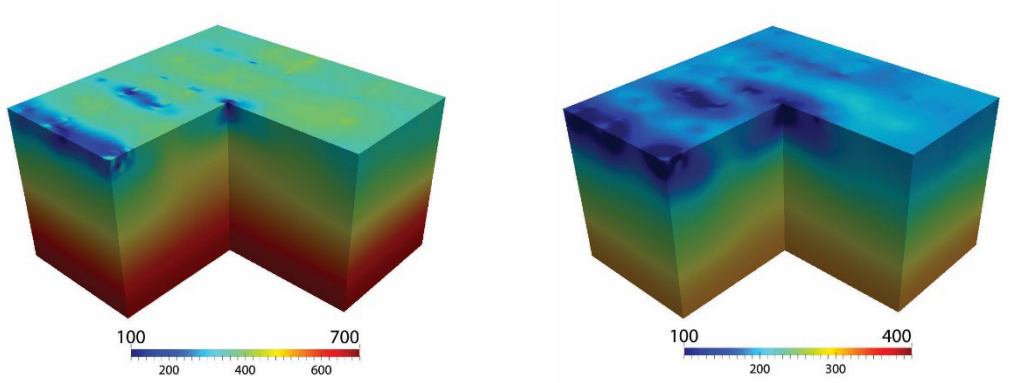

Figure 2.35: FWI-based subsurface imaging of P- and S-wave velocities of a geologic formation in Garner Valley, California. The imaged volume is 66m x 68m x 40m deep; 49 single-component geophones were deployed, 44 were used for inversion, and 5 were used as control geophones; 380,000 material parameters were inverted for (the P and S wave velocities were simultaneously inverted for)

Examples of other highly heterogeneous FWI imaging include the imaging of the Marmousi2 oil-industry benchmark test, depicted in Figure 2.36 (Kucukcoban et al., 2019). The benchmark includes strong heterogeneous karstic features, and it was successfully imaged by Kallivokas and his group using FWI.

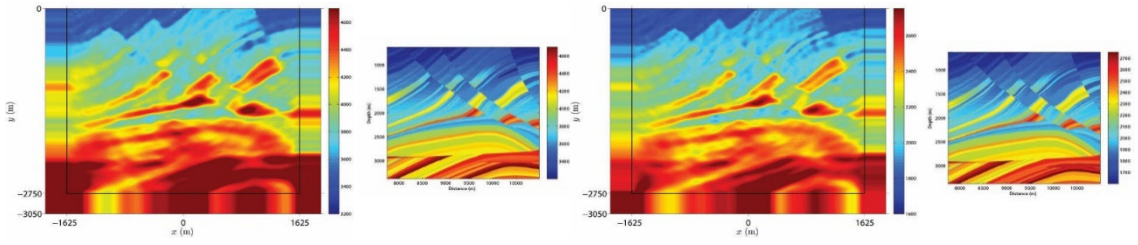

Figure 2.36: P- and S-wave velocities imaging of a cross-section of the Marmousi2 benchmark problem; the two leftmost figures are the P-wave velocities (imaged and target), and the two rightmost figures are the S-wave velocities (imaged and target).

When presented with strong contrasting zones, as is the case when seeking to detect voids, FWI performs well: shown below (Figure 2.37) is a FWI imaging experiment based on synthetics in the presence of a single inclusion embedded within a 3D layered medium (Fathi et al., 2015).

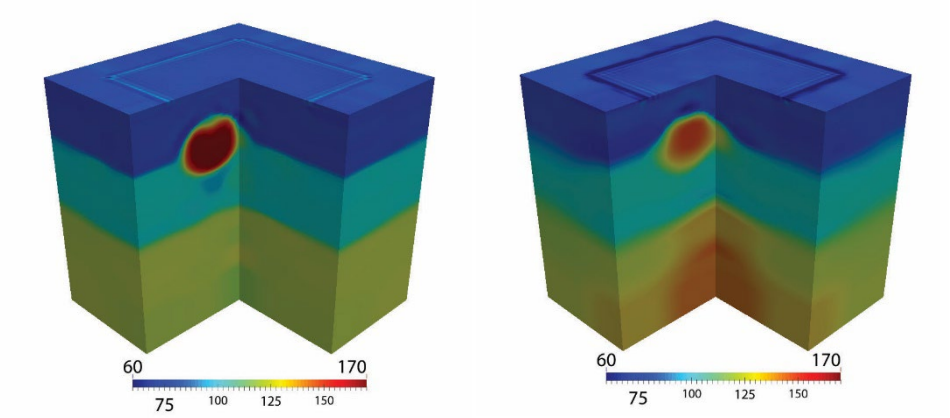

Figure 2.37: Elastic properties imaging using FWI of an inclusion embedded in a layered medium.

More recently, 3D FWI results were obtained from a void detection study conducted for the Florida Department of Transportation (FDOT) (Figure 2.38). The test site, in Newberry, Florida, consists of medium dense, fine sand and silt underlain by highly variable limestone, the depth of which varies from approximately 2 m to 10 m across the site. The FWI surveys used 48, 4.5-Hz vertical component geophones located in a 4 × 12 grid at 3 m spacing on the ground surface The seismic energy was created by the NHERI@UTexas Thumper shaker truck at the locations indicated in the figure. The final inverted 3D structure is show in Figure 2.38. The shear wave profile consists of soft soil layers at shallow depths, underlain by a stiffer weathered limestone layer. The compressional wave profile is consistent with the shear wave profile. Several potential voids were identified in the subsurface. For displaying the void, Figure 2.38 shows a 2D Vs and Vp profile slice taken at the middle of the domain, together with SPT N-values collected from a borehole drilled to verify the void. The void was confirmed to exist from about 4 to 7 m depth (Tran et al., 2019a,b).

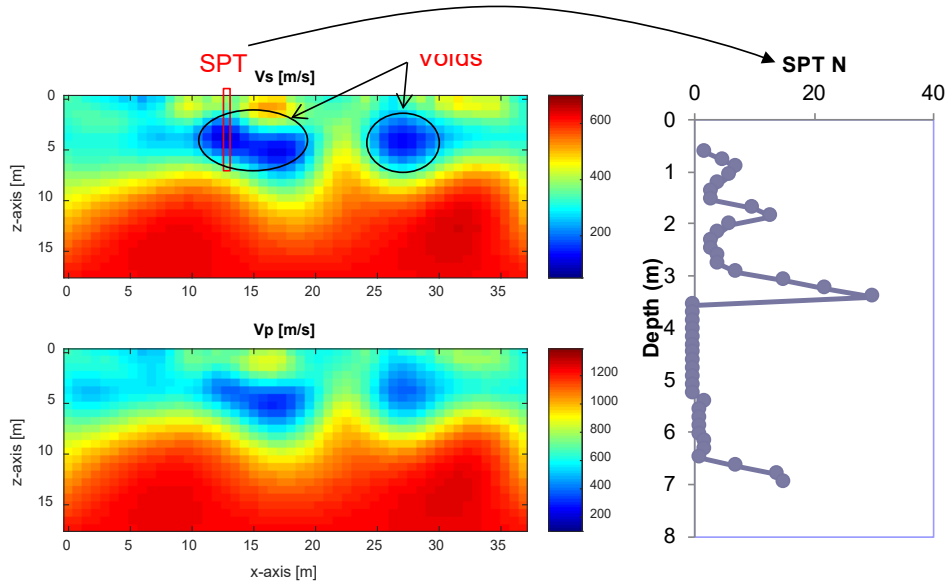

Figure 2.38: Active-source 3D FWI results in terms of S and P-wave velocities; x-section view of 3D results indicating two voids, one of which was verified by drilling and SPT measurements.

In summary, FWI appears quite promising in imaging the subsurface at high resolution, including any subsurface anomalies. The chief disadvantage of the method is the high computational cost in processing the acquired field data. Field challenges include the need to record the load (similar to seismic surveys for exploration), and the need for multiple shot locations, while the geophone array remains stationary. If at a site, the water table intrudes into the formation to be imaged, then a separate investigation should precede FWI (e.g., P wave refraction) to accurately determine the water table.

2.5. Summary Remarks

Summary remarks for each of the reviewed methods can be found at the end of the preceding sections 2.1-2.4. Based on the literature reviewed thus far, the following broad conclusions can also be drawn:

- No single method appears to be best positioned for detecting subsurface anomalies, whether soil-filled, water-filled, or air-filled (voids).

- For all methods, their ability to detect an anomaly of a given size depends on the method's parameters during field deployment (sensor spacing, source and sensor characteristics, etc.), as well as on the local site conditions (presence of water in the deposits; orientation, shape, and dimensions of the anomaly, etc.). Since during a blind field investigation, it is not possible to sweep over the entire parameter space (i.e., operate GPR antennas at multiple frequencies spanning a broad spectrum, or conduct ERT surveys using different array lengths, and multiple electrode spacings, etc.), it is quite possible that a few subsurface anomalies will be detected while others might be missed. If available, site-specific, a priori, information, can assist in partially alleviating such difficulties.

- The trace-based GPR method appears to be the easiest to operate with the least amount of data post-processing, but accuracy and consistency remain open questions, while interpretation of the trace-based imaging is subjective.

- The ERT method, especially in the context of 3D surveys, is promising, but not without potential pitfalls, as outlined in section 3. Together with FWI, it is one of the two true 3D methods under consideration herein.

- The MASW method appears to have limited ability to accurately resolve either the location or the size of subsurface anomalies, or both, unless they are located close to the surface and are of considerable size. The difficulty is rooted in MASW's theoretical underpinnings which do not allow consideration of arbitrary heterogeneity – a necessity when interested in the detection of subsurface anomalies.

- The FWI method is the most expensive both from a field investigation and a data post-processing point of view.

Chapter 3. Synthetic Studies

In this Chapter, we review a representative subset of the computational studies we conducted using synthetically-generated sensor data.

Synthetic data refer to the computationally-generated response at sensor locations, using software that models the *forward* problem for given probing sources.

The forward problem depends on the geophysical method: for ERT, the forward problem is governed by a Poisson-type equation for the electric potential, whereas for MASW and FWI, the forward problem is governed by Navier equations of elastodynamics written in terms of the displacement vectors. To address the forward simulations and the generation of synthetic data, we used a mix of in-house developed software, open-source software, as well as commercially-available software. Specifically, software we used included:

- 2D electric potential *forward* code based on finite elements for use with ERT (in-house);
- 2D *forward* elastodynamics code based on finite elements for use with FWI (in-house); and
- 2D *forward* open-source elastodynamics code (DENISE) for use with MASW.

In addition, to generate the electric potential synthetics for 3D ERT we used Ansys (a commercial general-purpose finite element software), as well as the forward capabilities of AGI's EarthImager3D and EarthImager2D[4].

For the associated inverse problems, we used the following:

- 2D FWI *inversion* code based on finite elements (in-house);
- 2D dispersion-curve *inversion* codes *swinvert* and *swbatch* for use with MASW (in-house); and
- 2D and 3D ERT *inversion* codes (AGI's EarthImager2D and EarthImager3D).

[4] AGI's EarthImager software is distributed as part of their ERT surveying apparatus. The EarthImager suite includes 2D and 3D, forward and inverse, modeling capabilities.

As previously noted, MASW is a 1D method, sometimes used in pseudo-2D mode, and, therefore, has no 3D counterpart. While we maintain in-house both a forward 3D elastodynamics state-of-the-art code, as well as a 3D FWI inversion code, which have been developed under the auspices of previously funded National Science Foundation research projects, due to time limitations, we were unable to adapt them to the needs of this project, and, therefore 3D FWI studies were not conducted. However, we note that the findings based on the 2D studies hold true for 3D as well.

3.1. Electric Resistivity Tomography – Synthetic Studies

3.1.1. The ERT Forward Problem

When DC current is injected in the ground, the soil acts as a circuit of resistors that impedes the free flow of current. The degree of current flow difficulty is expressed in terms of the soil's *resistivity*, which varies in space as a function of the soil type. In a typical setting of an ERT survey, DC current is injected through two injector electrodes on the ground surface (C1 and C2 in Figure 3.1): due to the current flow through the ground, electric potential differences can be measured between any two electrodes situated in the vicinity of the injector electrodes (P1 and P2 in Figure 3.1, which shows a typical ERT dipole-dipole array topology).

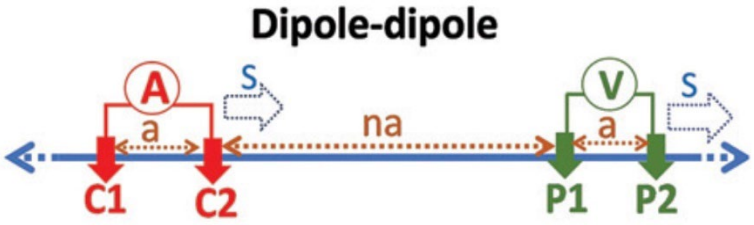

Figure 3.1: A typical dipole-dipole ERT array: C1 and C2 are the injector electrodes; P1 and P2 are receiver electrodes where the potential difference is measured

The electric potential $\phi(\boldsymbol{x})$ (not the potential difference) at any given point $\boldsymbol{x}$ on the ground surface and within the subsurface is governed by the following boundary-value problem (BVP):

$$
\begin{aligned}
&\nabla[\sigma(\boldsymbol{x}) \cdot \nabla\phi(\boldsymbol{x})] = -\tfrac{1}{2} I[\delta(\boldsymbol{x}-\boldsymbol{x}_s^+) - \delta(\boldsymbol{x}-\boldsymbol{x}_s^-)] && \text{in } \Omega, \\
&\tfrac{\partial\phi(\boldsymbol{x})}{\partial \mathbf{n}} = 0 && \text{on } \Gamma_s, \\
&\tfrac{\partial\phi(\boldsymbol{x})}{\partial \mathbf{n}} + \alpha\,\phi(\boldsymbol{x}) = 0 && \text{on } \Gamma_\infty.
\end{aligned}
\tag{3.1}
$$

where Ω denotes the domain occupied by the soil (subsurface), Γ_s is the ground surface, Γ_∞ denotes the far-field boundary, $\mathbf{n}$ is the outward normal to a domain-bounding surface such as Γ_s or Γ_∞, $\boldsymbol{x}$ denotes position vector ($\boldsymbol{x} = (x, y, z)$), I is the intensity of the injected current, δ denotes the Dirac- δ function, $\boldsymbol{x}_s^+$ and $\boldsymbol{x}_s^-$ denote the location of the two injector electrodes, and, importantly, $\sigma(\boldsymbol{x})$ is the conductivity of the subsurface[5].

Equation (3.1)a is the governing partial differential equation for the electric potential $\phi(\boldsymbol{x})$, accounting for the spatially-varying conductivity $\sigma(\boldsymbol{x})$ (and resistivity). Equation (3.1)b is a Neumann condition accounting for vanishing electric field on the ground surface, and equation (3.1)c is a Robin radiation condition, valid at infinity.

The BVP (3.1) holds true in 3D. To model the forward problem in 2D, additional assumptions need to be made, which impart important modifications to (3.1). Since the injected current in ERT surveys is always a 3D point source, first the governing equations need to be Fourier-transformed in space along the direction perpendicular to the electrode array line (e.g., along y), and the conductivity must be assumed to remain constant along the y direction: that is, every slice/vertical plane of the subsurface along the array line is assumed to have the same distribution of conductivity, i.e., $\sigma(x, y, z) \equiv \sigma(x, z)$. Accordingly, the BVP (3.1) reduces to:

$$
\begin{aligned}
&\nabla\left(\sigma(x,z) \cdot \nabla\tilde{\phi}(x,z)\right) - k_y^2\,\sigma(x,z)\,\tilde{\phi}(x,z) = -\tfrac{1}{2} I \cdot [\delta(\boldsymbol{x}-\boldsymbol{x}_s^+) - \delta(\boldsymbol{x}-\boldsymbol{x}_s^-)] && \text{in } \Omega, \\
&\tfrac{\partial\tilde{\phi}}{\partial \mathbf{n}} = 0 && \text{on } \Gamma_s, \\
&\tfrac{\partial\tilde{\phi}}{\partial \mathbf{n}} + \alpha\tilde{\phi} = 0 && \text{on } \Gamma_\infty,
\end{aligned}
\tag{3.2}
$$

[5] Conductivity is the reciprocal of the resistivity.

where k_y denotes the Fourier-transform variable (spatial wavenumber), and $\tilde{\phi}(x,z)$ is the Fourier-transformed electric potential. The BVP (3.2) forms the basis for the 2D forward ERT problem[6]. We note that: a) BVPs (3.1) and (3.2) exhibit a singularity under the injector electrodes, which needs to be treated appropriately; b) BVP (3.2) needs to be solved for a range of the spatial wavenumbers k_y, sum up the responses for all wavenumbers, before Fourier-inverting the sum to obtain the 3D response.

We implemented the 2D BVP (3.2), with appropriate treatment of the singularity, using finite elements to obtain the response (electric potential) at the ERT array electrodes. Our numerical results were compared against EarthImager2D's forward modeling and found to be in excellent agreement.

Similarly, we used Ansys to model the 3D forward problem defined by BVP (3.1). Because Ansys is a general-purpose finite element package, it cannot account for the special treatment that the singularity under the injector electrodes requires. Consequently, the Ansys forward modeling results exhibited differences when compared against EarthImager3D's forward modeling in the near-field, i.e., at distances close to the injector electrodes. Nevertheless, we used both Ansys and EarthImager3D to generate the forward problem synthetics.

3.1.2. The ERT Inverse Problem

The ERT inverse problem that leads to the imaging of the subsurface in terms of the soil's resistivity is typically cast as a minimization problem where the misfit between measured potential differences and computed potential differences is minimized:

$$J = \sum_{m=1}^{N} \left(u_{\text{computed}}^{(m)} - u_{\text{measured}}^{(m)}\right) \cdot \left(u_{\text{computed}}^{(m)} - u_{\text{measured}}^{(m)}\right) \tag{3.4}$$

In (3.4), J is the misfit functional, N is the number of electrode pairs, and $u_{\text{computed}}^{(m)}$ and $u_{\text{measured}}^{(m)}$ are the computed and measured potential differences, respectively. The computed solutions

[6] The lateral (along y) conductivity/resistivity homogeneity is a common assumption in both our in-house software and EarthImager2D.

correspond to trial conductivity distributions. The minimization of J is typically constrained by the underlying physics, which, in this case, are described by the BVPs (3.1) and (3.2). In addition, it is common that a regularization scheme is implemented to combat the inherent solution multiplicity associated with inverse problems. The process is iterative, and, upon convergence, if attained, the misfit J is minimized (up to a prescribed tolerance), and the subsurface conductivity distribution that corresponded to the last value of the misfit is pronounced to be the true distribution.

We used EarthImager2D and EarthImager3D to invert for the subsurface's conductivity/resistivity.

3.1.3. 2D and 3D ERT Synthetics

Consider first the case of a subsurface object in the form of a parallelepiped of dimensions 4 m by 1 m by 2 m (along x, y, and z, respectively), as depicted in Figure 3.2. The object is assigned a resistivity of 500 Ohm-m and is embedded in a homogeneous host with 50 Ohm-m resistivity. The outer domain measures 20 m long by 10 m wide by 6.7 m deep. The top surface of the object is at a depth of 1.25 m from the ground surface, the latter set at $z = 0$ m.

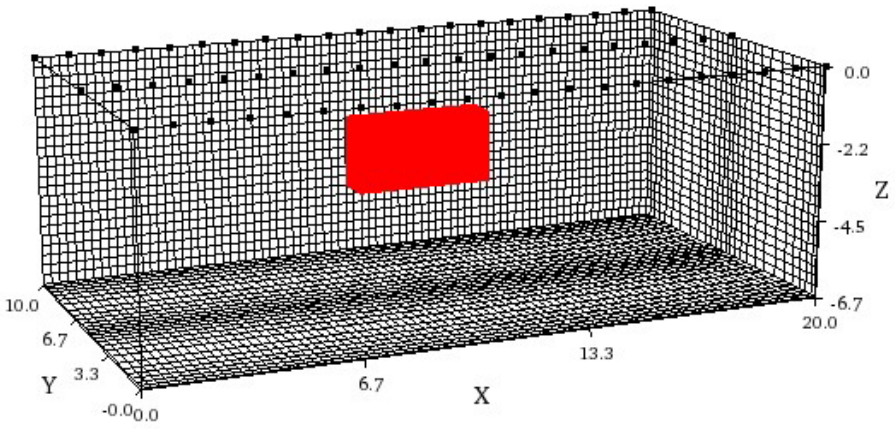

Figure 3.2: A parallelepipedal anomaly of 500 Ohm-m resistivity, embedded in a homogeneous host of 50 Ohm-m resistivity.

A dipole-dipole electrode array was deployed along x, consisting of 63 electrodes spaced 1 m apart, and organized in 3 parallel lines of 21 electrodes each (shown as black dots in Figure 3.2).

The spacing between the 3 electrode lines was 5 m. Both slide-along and roll-along experiments were conducted and hundreds of datasets were assembled for multiple injector electrode positions, effectively mimicking a detailed field experiment.

We used EarthImager3D to generate the potential differences at the electrode array, and then fed the datasets into EarthImager3D's inverse engine, seeking to reconstruct the target. The inversion results are depicted in Figure 3.3-Figure 3.5.

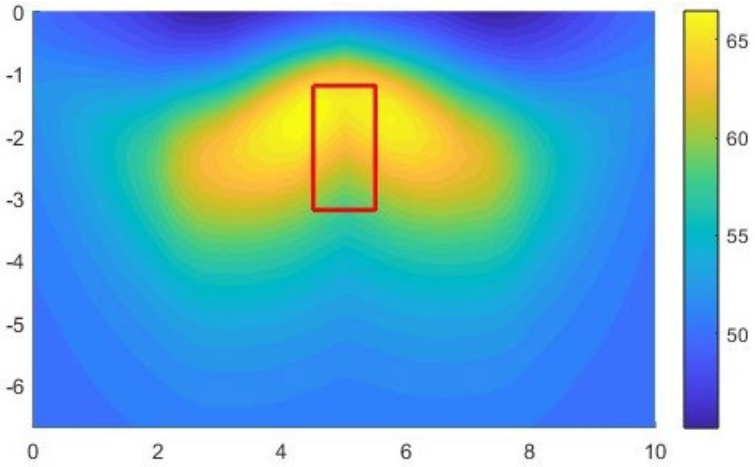

Figure 3.3: A planar cross-section of subsurface resistivity sliced at $\boldsymbol{x} = 10$ m; the red line delineates the parallelepipedal inclusion.

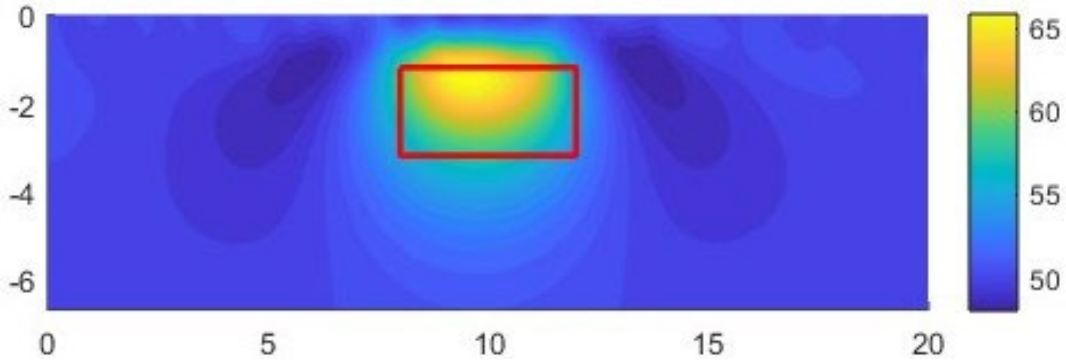

Figure 3.4: A planar cross-section of subsurface resistivity sliced at $\boldsymbol{y} = 5$ m; the red line delineates the parallelepipedal inclusion.

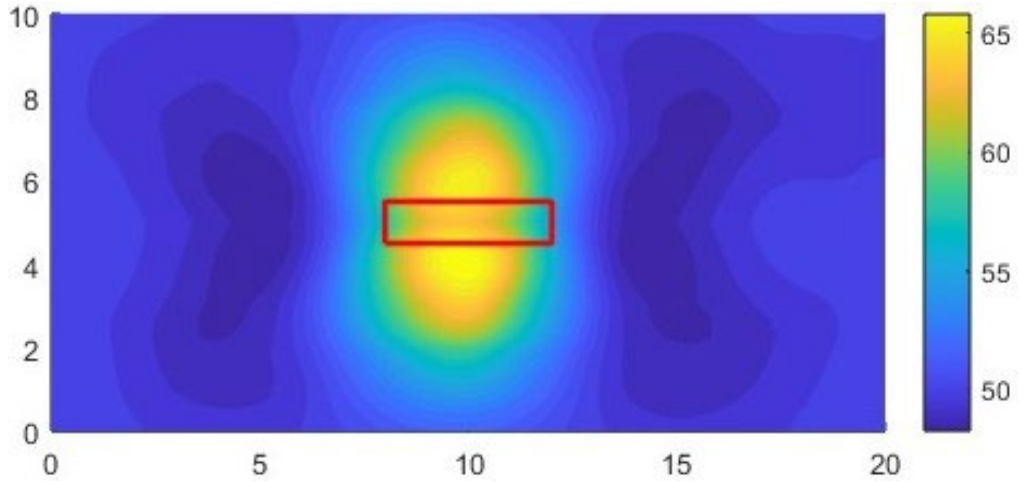

Figure 3.5: A planar cross-section of subsurface resistivity sliced at $\boldsymbol{z} = 2.25$m; the red line delineates the parallelepipedal inclusion.

Figure 3.3, Figure 3.4, and Figure 3.5, depict planar slices of the subsurface resistivity distributions. The red rectangles delineate cross-sections of the embedded parallelepiped. There are two difficulties revealed by the plots of subsurface resistivities: a. the inverted resistivity has missed the object, despite showing resistivity intensity at that location, and b. while the reconstructed resistivity values for the background are close to the target (~50 Ohm-m), the object's resistivity is off by a factor of ~8 (65 Ohm-m versus 500 Ohm-m). We note that in generating the data, we avoided committing a, so-called, "inverse crime", usually associated with using the same mesh for generating the forward solution as the mesh used for the inversion.

We also used Ansys to generate the forward synthetics for the following numerical experiment: an ellipsoid with semi-axes 2 m by 0.5 m by 1 m, also embedded in the same homogeneous host as in the previous example, at a depth of 1.25m from the ground surface (Figure 3.6). The ellipsoid had a resistivity of 500 Ohm-m. The electrode array had the same number of electrodes and geometric arrangement as in the previous example. Figure 3.7, Figure 3.8, and Figure 3.9 depict planar slices of the subsurface resistivity, including the trace of the ellipsoid (red line): here too, it is clear that EarthImager3D did not succeed in reconstructing the target ellipsoid.

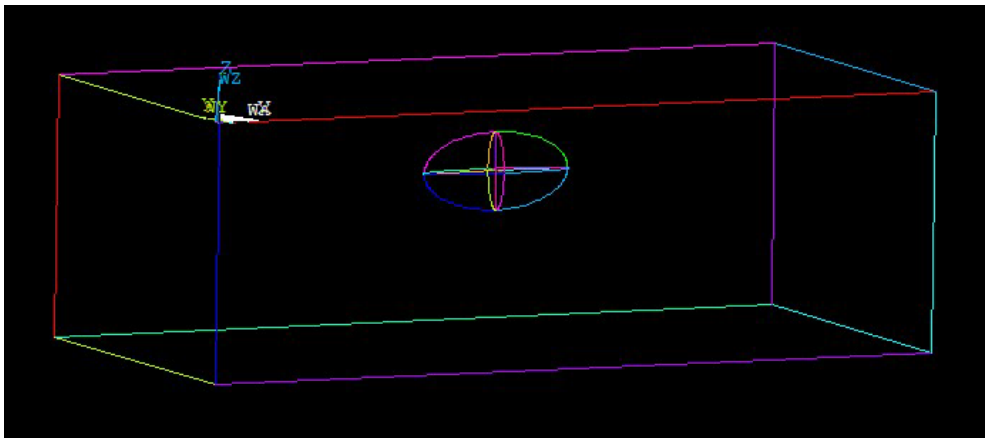

Figure 3.6: An ellipsoidal anomaly of 500 Ohm-m resistivity, embedded in a homogeneous host of 50 Ohm-m resistivity

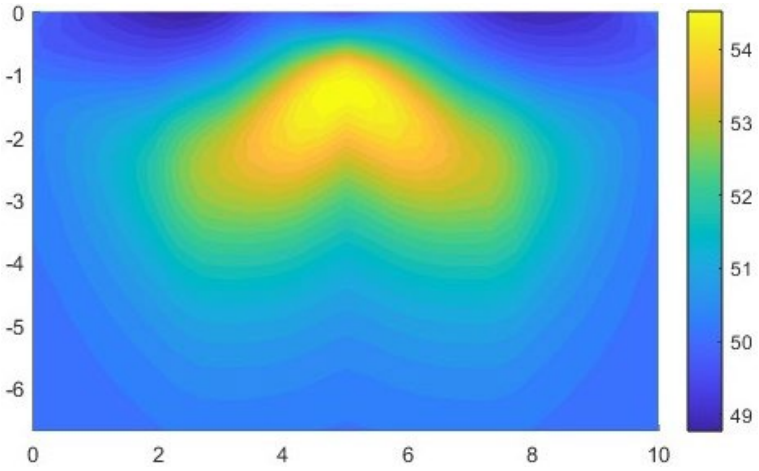

Figure 3.7: A planar cross-section of subsurface resistivity sliced at $\boldsymbol{x} = 10$ m; the red line delineates the ellipsoidal inclusion.

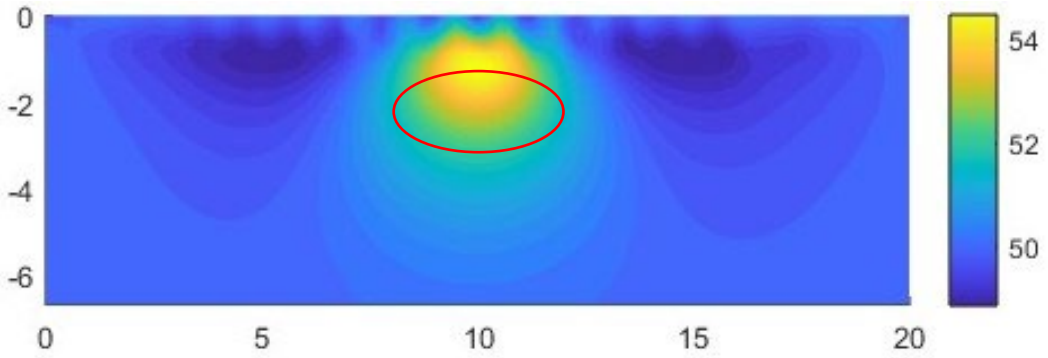

Figure 3.8: A planar cross-section of subsurface resistivity sliced at $\boldsymbol{y} = 5$ m; the red line delineates the ellipsoidal inclusion.

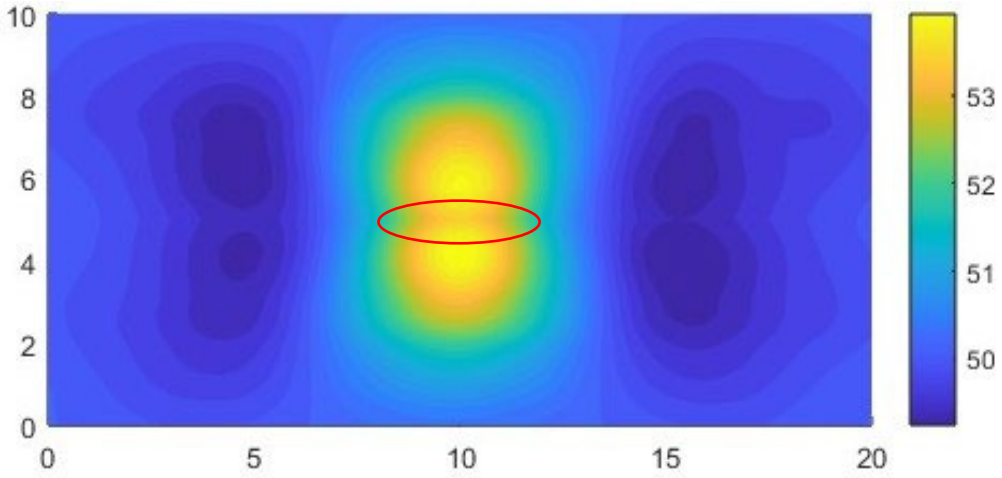

Figure 3.9: A planar cross-section of subsurface resistivity sliced at $\boldsymbol{z} = 2.25$ m; the red line delineates the ellipsoidal inclusion.

Next, we turn to 2D forward synthetics and associated inversion. To this end, consider a 4 m by 2m rectangle of 500 Ohm-m resistivity, embedded in a homogeneous host of 50 Ohm-m, 1.25 m below the ground surface: the model, together with the finite element mesh is depicted in Figure 3.11. The background host is similarly modeled with a rectangle, 20 m long by 6.7 m deep. We deploy a dipole-dipole array comprising 21 electrodes, spaced 1 m apart.

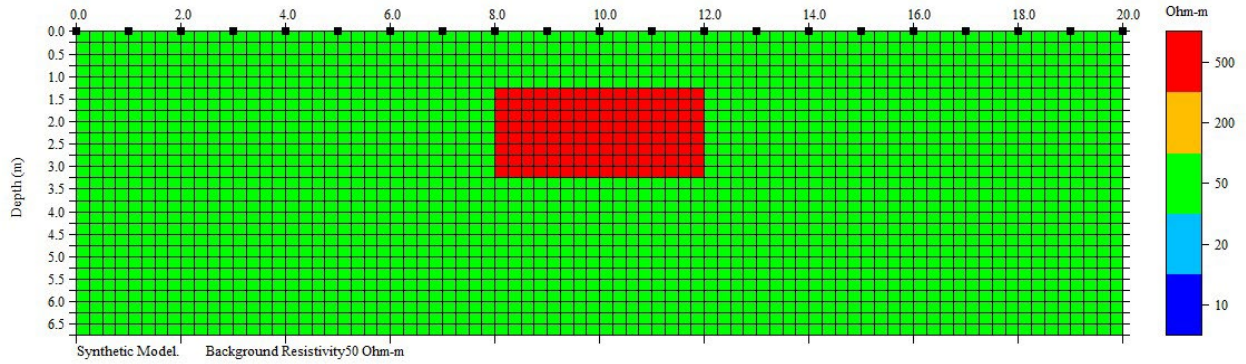

Figure 3.10: A 2D prototype ERT model; a rectangular anomaly of 500 Ohm-m resistivity, embedded in a homogeneous host of 50 Ohm-m resistivity

We generated the electric potential synthetics using our in-house code and/or EarthImager2D, and fed the datasets to EarthImager2D's inverse engine; the resulting subsurface resistivity is depicted in Figure 3.11. The red lines delineate the target, and it is clear that the inversion has satisfactorily recovered the resistivity of the target object (the maximum value was 449 Ohm-m versus 500

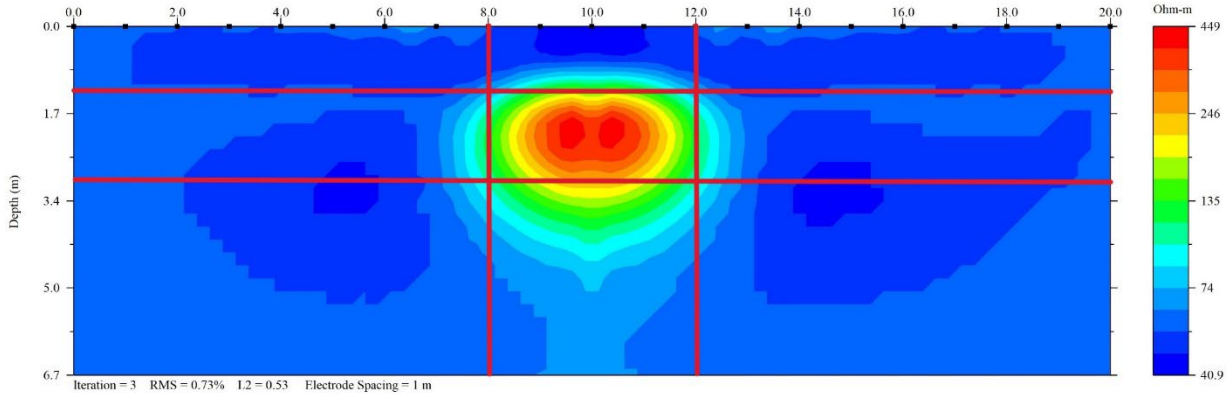

Figure 3.11: Subsurface resistivity map following 2D inversion; the red rectangle in the middle of the plot delineates the target rectangle.

Ohm-m of the target), while the background varies between 40 Ohm-m and 70 Ohm-m. The near-surface resistivity is better recovered than the forward-scatter region of the target, where the resistivity exceeded the target values (light cyan region).

To further test the capabilities, we use Ansys to generate the forward synthetics in 3D, using a prolonged parallelepiped in the direction perpendicular to the array line, thus mimicking 2D conditions, as depicted in Figure 3.12.

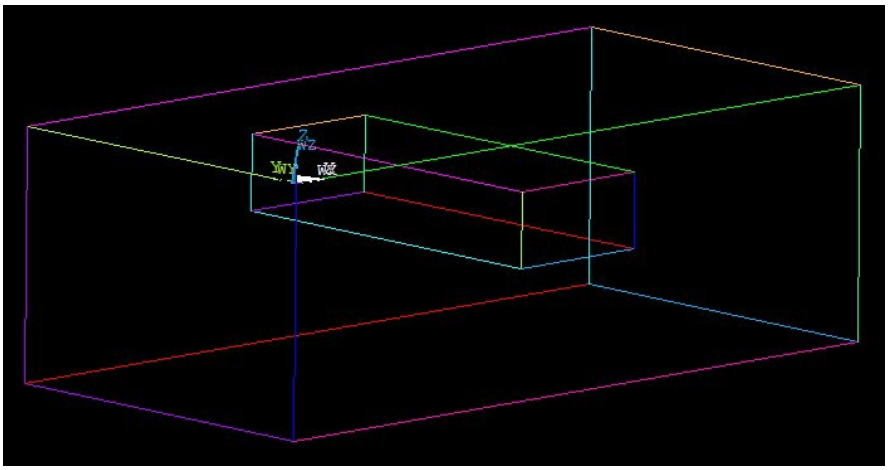

Figure 3.12: A long parallelepipedal anomaly of 500 Ohm-m resistivity, embedded in a homogeneous host of 50 Ohm-m resistivity, mimicking 2D conditions.

The resistivity properties of the background host and the target remain the same; the block surrounding the target object is 20 m long by 10 m wide by 6.7 m deep. EarthImager2D recovered the background resistivity and that of the target object satisfactorily, as it can be seen in Figure 3.13.

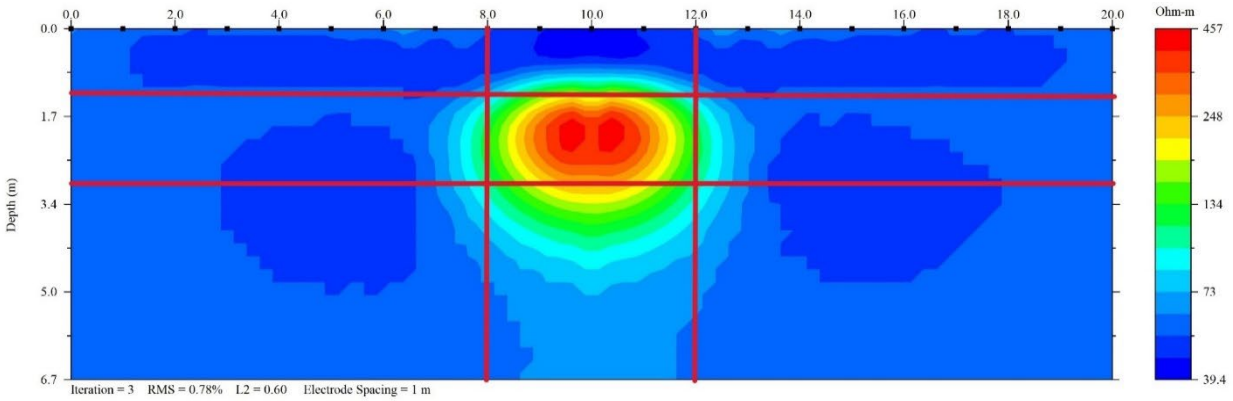

Figure 3.13: Subsurface resistivity map following 2.5D inversion; the red rectangle in the middle of the plot delineates the target rectangle.

Thus, in summary, the numerical experiments with the ERT synthetics suggest difficulties with the 3D version of EarthImager, while the 2D version appears to satisfactorily recover embedded objects under 2D or pseudo-2D assumptions. We note that the usual constraints associated with ERT apply: detection depth is limited to about 15%-20% of the array length, the smaller the target anomaly is, the more difficult the property determination becomes even when the anomaly is detected, the size of the detectable anomaly depends on the array spacing, etc.

3.2. Multi-Channel Analysis of Surface Waves – Synthetic Studies

To explore the detectability of anomalies/voids using MASW, the prototype model depicted in Figure 3.14 was adopted. Accordingly, a rectangular box, intended to resemble an anomaly, of length L and thickness T, was embedded at depth D from the ground surface, within a homogeneous half-space host of shear wave velocity V_{S-HS}. The anomaly was assumed to have a shear wave velocity V_S, and the contrast between the host and the anomaly was defined as $I = \frac{V_S}{V_{S-HS}}$. An array of 24 geophones, spaced 1 m apart, was deployed on the ground surface. Table 1 summarizes the sensor array and source parameters used for the forward MASW synthetics

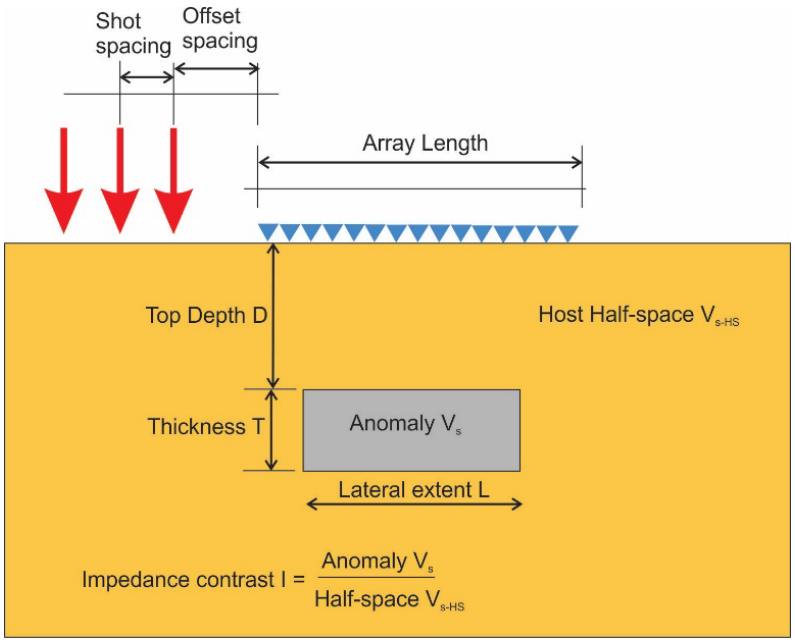

Figure 3.14: MASW prototype model schematic. The shear-wave velocity ($\boldsymbol{V_{s-HS}}$) of the half-space and of the anomaly ($\boldsymbol{V_s}$)were varied to create a range of impedance contrasts ($\boldsymbol{I}$), while the top depth ($\boldsymbol{D}$), thickness ($\boldsymbol{T}$), and lateral extent ($\boldsymbol{L}$) of each anomaly were varied to represent a set of possibilities that may be encountered during field testing. Roughly 300 models were created for each unique impedance contrast and half-space $\boldsymbol{V_{s-HS}}$ pairing, such that over 3,000 treatment models were created in total.

Number of receivers	**24**
Receiver spacing	**1 m**
Array length	**23 m**
Type of source	**Spike wavelet, 0-15 Hz**
Sampling frequency	**400 Hz**
Recording duration	**3 s**
Nominal offset	**10 m**
Source spacing	**5 m**

Table 1: Model parameters for MASW synthetics

We used the open-source software DENISE (Köhn et al., 2012) to obtain the synthetics for each model. DENISE is a 2D finite-difference code for modeling elastic wave propagation; we recall

that a fundamental and pervasive assumption in MASW is that the soil layering is horizontal, which implies that in the direction perpendicular to the vertical plane going through the array line there is homogeneity (it is an assumption identical to the one made in 2D ERT). This assumption justifies the use of the 2D plane-strain code DENISE.

DENISE implements a staggered-grid finite-difference discretization scheme (Virieux, 1986) to numerically propagate stress wave energy throughout any arbitrary model. The models used in this study were 256- m long and 64- m deep and discretized every 0.25 m in the horizontal and vertical directions (i.e., 1024 x 256 grid points). The top of the model followed the free surface boundary condition (Levander, 1988), whereas the bottom and sides of the model were truncated with perfectly matched layers (PMLs) (Komatitsch and Martin, 2007). For this study, an eighth-order finite-difference operator was used in space, and a second-order finite-difference operator was used in time. A separate simulation was performed for each source location for each model. The simulations were performed for a duration of 3 s with a time step of 0.02 ms, as required for numerical stability. The resultant waveforms were down-sampled to 400 Hz prior to dispersion processing.

The frequency domain beamformer (FDBF) with inverse-amplitude weighting and a plane-wave steering vector (Zywicki, 1999) was used to transform the simulated seismic data into estimates of the model's experimental dispersion data. To perform the inversions for this study, the surface wave inversion workflow *swinvert* developed by Vantassel and Cox (2021a) was adopted. This workflow employs multiple large-scale global search inversions that incorporate different user-defined trial parameterizations (e.g., different numbers of layers) to address the surface wave inversion problem's non-linearity and non-uniqueness. To perform the large number of surface wave inversions required for this study, *swbatch* (Vantassel et al., 2020), an open-source tool that allows for batch-style surface wave inversion, was used. It should be noted that *swbatch* is a user-friendly web-application, available on the DesignSafe-CyberInfrastructure (Rathje et al., 2017), that allows those without prior knowledge of high-performance computing (HPC) to use it in their inversion studies. *swbatch* employs the global search Neighborhood Algorithm (Sambridge, 1999) as implemented in the Dinver module (Wathelet et al., 2004) of the open-source software Geopsy (Wathelet et al., 2020) as its inversion engine. Table 2 summarizes the range of considered values for the various parameters of the prototype model: accordingly, the smallest anomaly was 1 m by

1 m, and the largest 36 m x 4 m. Two shear wave velocities were chosen for the background host (150 m/s and 300 m/s) corresponding to soft soils; given the range of impedance contrast considered, the softest inclusion had a shear wave velocity of 30 m/s and the stiffest ~450 m/s.

Variable	Notation	Values
Impedance contrast	I	0.67, 0.2, 0.5; 1.5, 2.0, 5.0
Half-space shear wave velocity (m/s)	V_{S-HS}	150, 300
Anomaly thickness (m)	T	1, 2, 4
Anomaly lateral extent (m)	L	1, 4, 6, 10, 14, 19, 25, 30, 36
Top depth (m)	D	2 – 20

Table 2: Summary of model variables with associated values

The numerical study was reported in Crocker et al. (2021): accordingly, over 3,000 MASW simulations were performed on models with and without anomalies (i.e., treatment and control models, respectively). These simulations were designed to replicate typical MASW testing procedures as found in the literature, and the anomalies were created to encompass a range of sizes (i.e., varying thickness and lateral extent), depths, and stiffnesses (defined by an impedance contrast, or the ratio of the anomaly's stiffness to the surrounding material's stiffness).

The possibility of detecting the anomalies was summarized in detection feasibility plots (Figure 3.15), which were developed using detectability misfit values (M_{detect}) that quantify the difference between a control model's dispersion and the dispersion of its corresponding treatment models (i.e., a model containing an anomaly). A detectability index (M_{detect}) threshold value of 1.0 was used to distinguish the detectability of an anomaly: M_{detect} values greater than 1.0 (indicated by colors other than blue) represent anomalies that are more likely to be detected, whereas values less than 1.0 (indicated by blue) represent anomalies that are less likely to be detected.

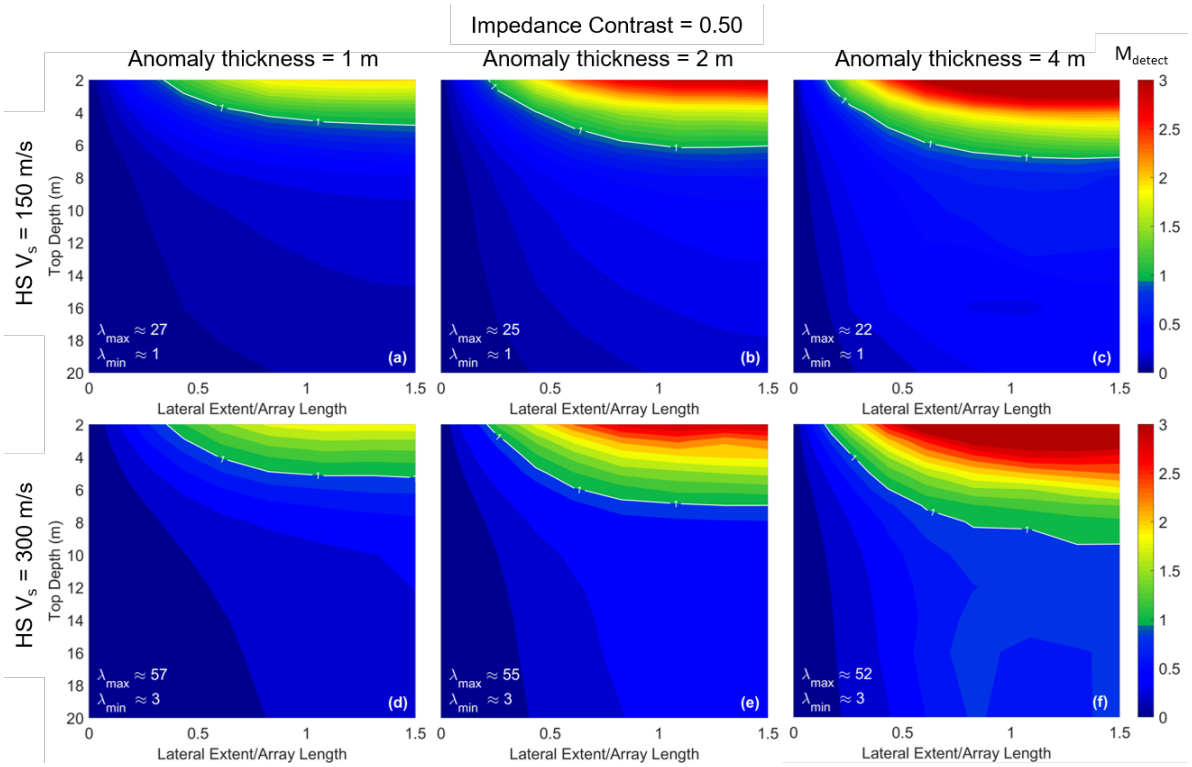

Figure 3.15: An example of detection feasibility plots as presented in Crocker et al. (2021). (a-c) represent models with a half-space $\boldsymbol{V_s}$ ($\boldsymbol{V_{s-HS}}$) of 150 m/s while (d-f) are for a $\boldsymbol{V_{s-HS}}$ of 300 m/s. Each row is listed in order of increasing anomaly thickness, such that (a-c) and (d-f) are for anomalies that are 1 m, 2 m, and 4 m thick, respectively. Note that the anomalies have an impedance contrast of 0.50, meaning that the anomalies presented in (a-c) have a $\boldsymbol{V_s}$ equal to 75 m/s, while those in (d-f) have a $\boldsymbol{V_s}$ equal to 150 m/s (from Crocker et al. 2021).

The results of the detection feasibility plots indicate that the possibility of detecting an anomaly increases as the anomaly's size increases, or as its depth decreases, which is expected. Moreover, when reviewing Figure 3.15(a), it seems that relatively thin anomalies (i.e., 1 m-thick) must be at least half the length of the array and no more than about 4 m-deep to have a chance of detection. Both of these observations are consistent with the theory behind MASW, which requires horizontal layering: thus, any departure, let alone a significant departure from the layering as those corresponding to anomalies of limited length, make detectability more difficult, if not impossible.

Furthermore, relatively large anomalies (i.e., 4 m-thick; refer to Figure 3.15(c)) must be at least a quarter of the array length and no more than about 6 m-deep to have a chance of detection. However, when comparing Figure 3.15(a)-(c) and Figure 3.15(d)-(f), these limits are shown to

increase when the overall velocity contrast between the anomaly and the surrounding material increases. This trend is more pronounced when comparing the maximum depths at which an anomaly can be detected, although subtle changes in the minimum detectable lateral extent are also visible. *Given these results, it seems that detecting an anomaly or void using MASW is difficult, requiring anomalies of fairly significant size and/or situated at relatively shallow depths*. It should be noted that Figure 3.15 represents only one of six sets of detection feasibility plots shown in Crocker et al. (2021); however, the conclusions presented herein are supported by the remaining detection feasibility plots.

It is of interest also to review the possibility of resolving an anomaly (i.e., determining its true size, location, and stiffness), once it has been detected (detection implies an approximate location, and blurry delineation). We performed a resolvability study by inverting for the soil layering of approximately 120 of the 3,000 models considered (see Crocker et al. (2021)). These models were selected based on trends in anomaly lateral extent and depth, and inversion parameterizations were developed based on known treatment model parameters (i.e., V_s, P-wave velocity V_p, and mass density ρ). Two layering parameterizations were used throughout the process: (1) the previously described FTL parameterization, in which relatively thin layers of fixed and equal thickness are used, and (2) the Layering by Number (LN) parameterization approach, which uses a predetermined number of layers with variable thickness to discretize the subsurface (for further details regarding these layering parameterizations, the reader is referred to Vantassel and Cox, 2021). Inversions performed using FTL included 10 2 m-thick layers and 20 1 m-thick layers, while 3, 4, and 5 layers of variable thickness were used with the LN parameterization. The inverted profiles were then compared to the true 1D subsurface profile at the center of the array both qualitatively (i.e., visually) and quantitatively (i.e., through the use of a velocity profile misfit, $M_{resolve}$). An example of a set of inversion results from Crocker et al. (2021) is shown in Figure 3.16.

Figure 3.16(a) shows the detection feasibility plot for models with a half-space V_s of 300 m/s containing anomalies with a thickness of 4 m and V_s of 150 m/s (i.e., the detection feasibility plot shown in Figure 3.15(f). The black hollow circles indicate five different treatment models with anomaly top depths ranging from 2 to 14 m. Figure 3.16(b)-(f) show the inversion results for an anomaly with a lateral extent of 14 m, which is roughly 0.6 times the array length, placed at top

depths of 2, 5, 7, 8, and 14 m, respectively. In this figure, only the results of the LN = 3, 4, and 5 inversion parameterizations are shown.

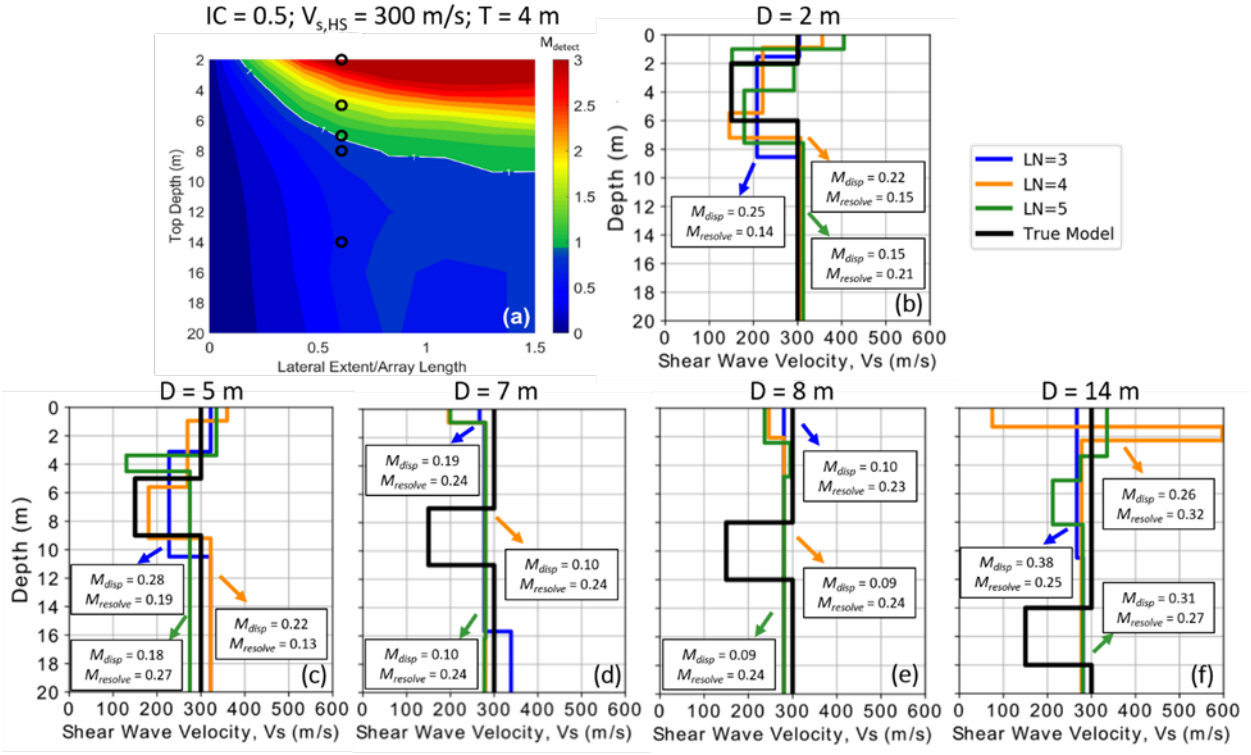

Figure 3.16: (a) Summary of detectability misfits (M_{detect}) for a model with a half-space V_s ($V_{s,HS}$) of 300 m/s containing an anomaly with a thickness of 4 m and V_s of 150 m/s (IC = 0.5). (b-f) show the inversion results for an anomaly with a lateral extent of 14 m (L/A = 0.61) placed at top depths of 2, 5, 7, 8, and 14 m, respectively (models I0.50-H300-T4-D(2,5,7,8,14)-L14, as indicated in (a) by black circles). The misfit values between theoretical and experimental dispersion data (M_{disp}) and between inverted and true V_s profiles ($M_{resolve}$) are shown for each LN parameterization in (b-f)

This is due to the FTL (fixed-thin-layer) inversion parameterizations resulting in very poor anomaly resolution. Specifically, in any case, the FTL parameterization resulted in thin layers of significantly high/low stiffness than the actual anomaly, leading to poor qualitative and quantitative results. In contrast, when reviewing Figure 3.16(b)-(f), the LN parameterizations are shown to result in relatively reasonable subsurface profiles. Further, the results show that intuitively, as an anomaly is placed closer to the ground surface, the ability to resolve it increases (compare Figure 3.16(b) to Figure 3.16(f)). For example, the shallowest anomaly (top depth = 2

m; Figure 3.16(b)) was resolved relatively accurately via inversion. However, many of the deeper anomalies (e.g., top depth > 5 m) could not be resolved accurately. Although only a subset of results is shown herein, it should be noted that this trend was also seen in other results reported by Crocker et al. (2021).

In summary, the MASW experiments with synthetic data confirmed the limitations of the method in detecting subsurface anomalies and/or voids.

3.3. Full-Waveform Inversion – Synthetic Studies

To explore FWI's ability to detect and quantify subsurface anomalies/voids using synthetics, we turned to the same prototype problem used in the MASW studies. However, instead of exploring all possible combinations of the parameter space suggested by the values of Table 2, we focus on select cases for which MASW has failed to detect the anomaly. For example, Figure 3.17 shows 6 red dots, each one corresponding to a parameterization of the prototype model, for which MASW failed to resolve the anomaly (the anomaly's impedance contrast is I =0.5). Specifically, the table in Figure 3.17 summarizes the 6 sets of parameters. Figure 3.18-Figure 3.23 depict the FWI results for the 6 cases MASW did not succeed (the anomaly thickness was T=1 m in all cases, and the anomaly is softer than the host).

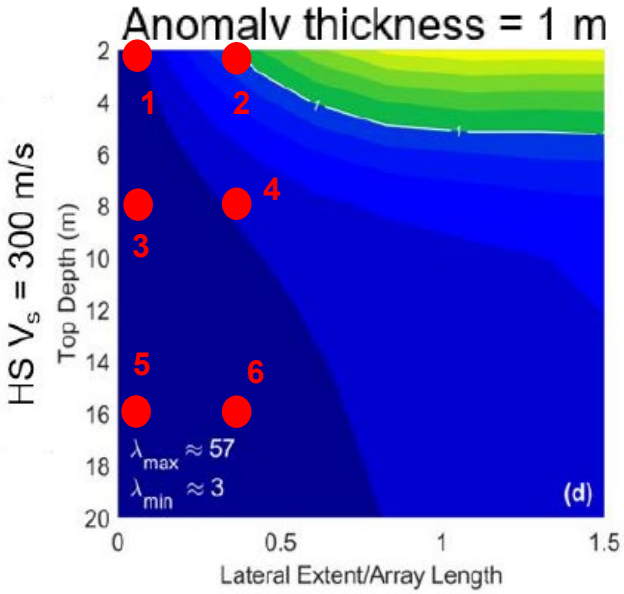

Case number (I = 0.5)	Anomaly Depth D	Anomaly Lateral Extent L
1	2 m	3 m
2	2 m	9 m
3	8 m	3 m
4	8 m	9 m
5	16 m	3 m
6	16 m	9 m

Figure 3.17: Red dots indicate MASW detectability failure cases; the table shows the subsurface anomaly parameters used in each one of the MASW failure cases (1-6).

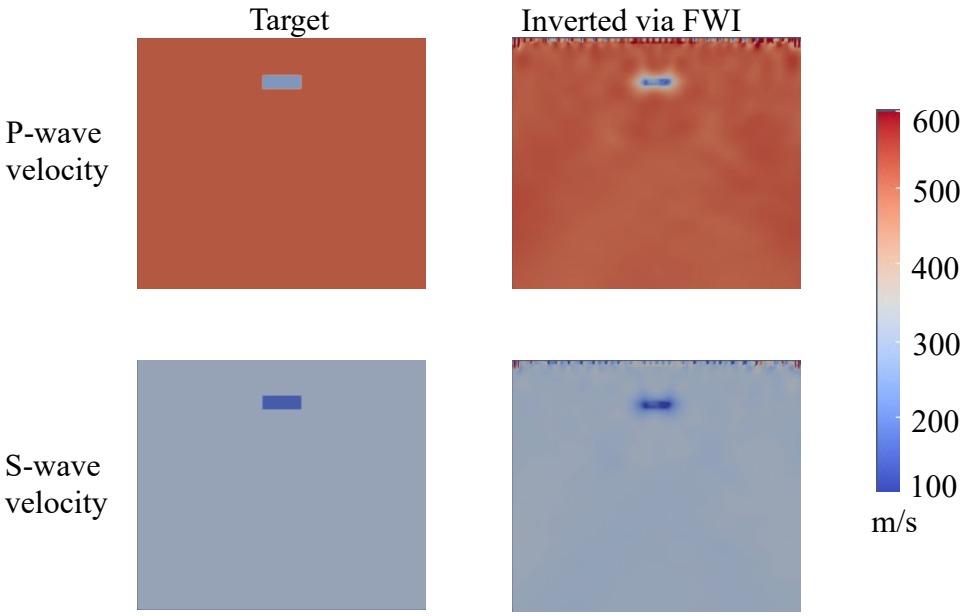

Figure 3.18: FWI imaging for Case 1: host shear wave velocity $\boldsymbol{V_{s-HS}}$ =300 m/s, anomaly shear wave velocity $\boldsymbol{V_s}$= 150 m/s, depth $\boldsymbol{D}$ = 2 m, length $\boldsymbol{L}$ = 3 m.

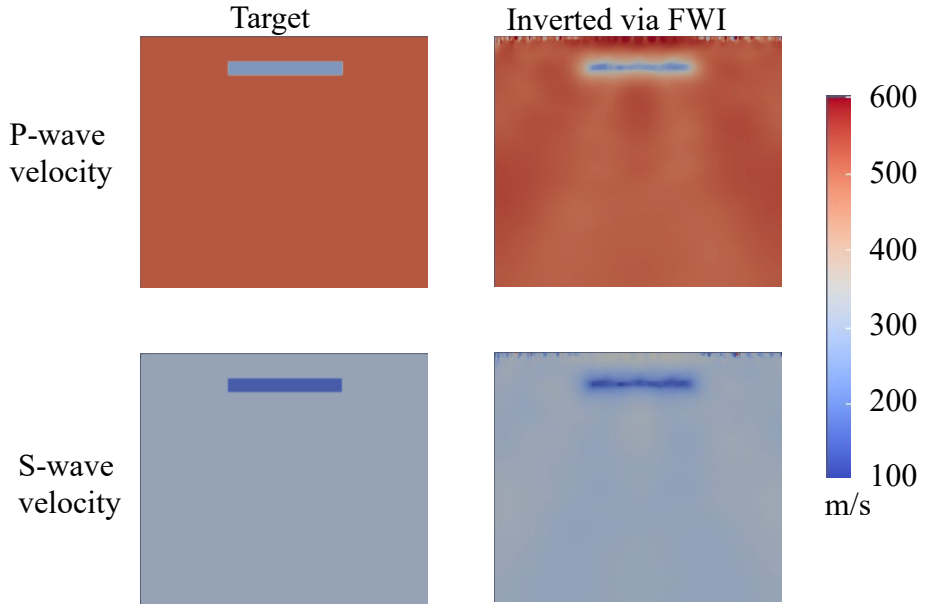

Figure 3.19: FWI imaging for Case 2: host shear wave velocity $\boldsymbol{V_{s-HS}}$ =300 m/s, anomaly shear wave velocity $\boldsymbol{V_s}$= 150 m/s, depth $\boldsymbol{D}$ = 2 m, length $\boldsymbol{L}$ = 9 m.

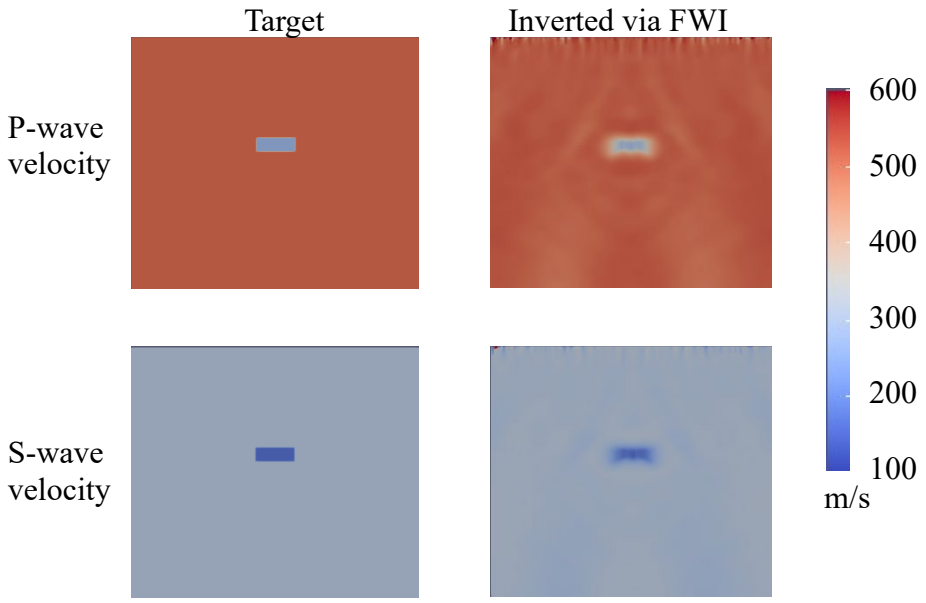

Figure 3.20: FWI imaging for Case 3: host shear wave velocity $\boldsymbol{V_{s-HS}}$ =300 m/s, anomaly shear wave velocity $\boldsymbol{V_s}$= 150 m/s, depth $\boldsymbol{D}$ = 8 m, length $\boldsymbol{L}$ = 3 m.

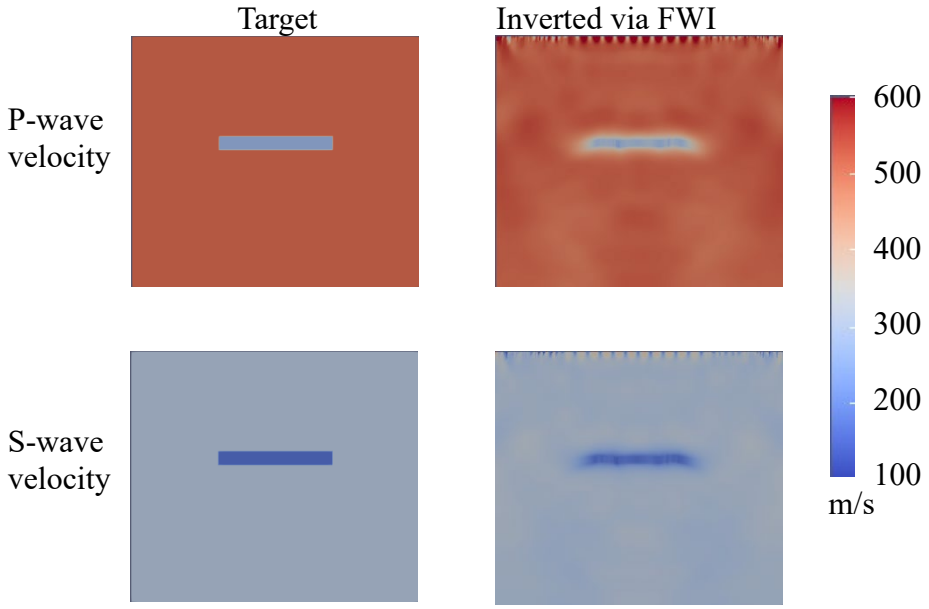

Figure 3.21: FWI imaging for Case 4: host shear wave velocity $\boldsymbol{V_{s-HS}}$ =300 m/s, anomaly shear wave velocity $\boldsymbol{V_s}$= 150 m/s, depth $\boldsymbol{D}$ = 8m, length $\boldsymbol{L}$ = 9 m.

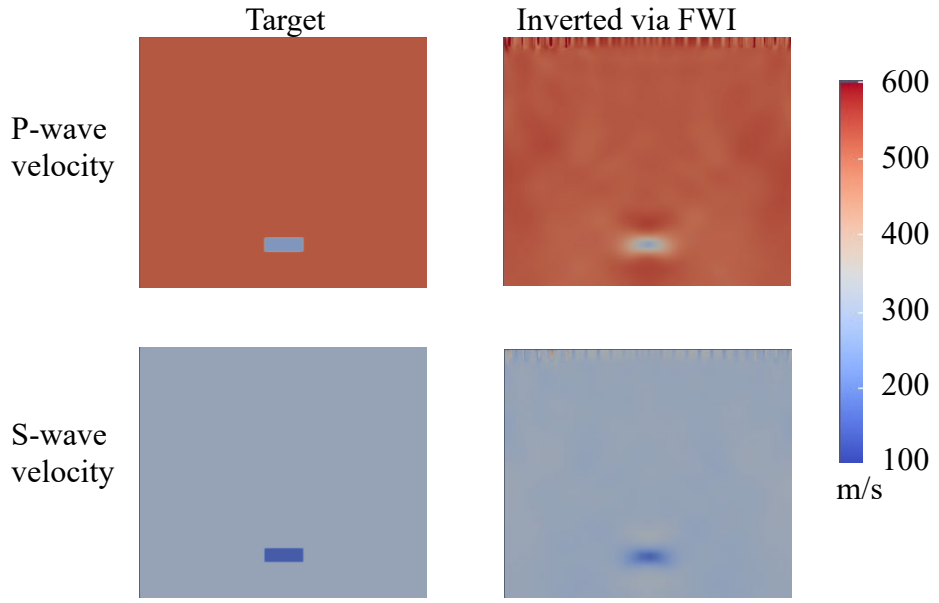

Figure 3.22: FWI imaging for Case 5: host shear wave velocity $\boldsymbol{V_{s-HS}}$ =300 m/s, anomaly shear wave velocity $\boldsymbol{V_s}$= 150 m/s, depth $\boldsymbol{D}$ = 16 m, length $\boldsymbol{L}$ = 3 m.

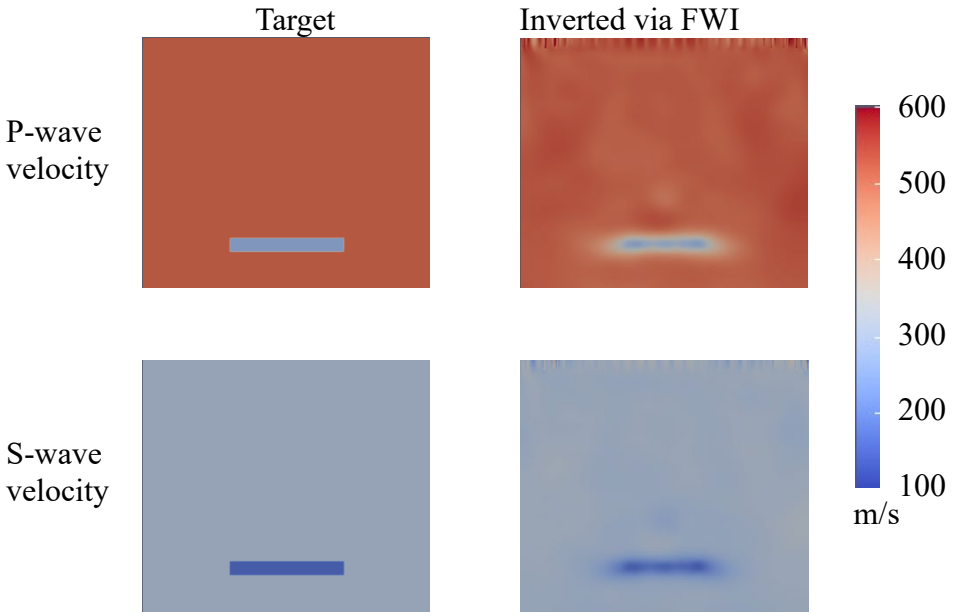

Figure 3.23: FWI imaging for Case 6: host shear wave velocity $\boldsymbol{V_{s-HS}}$ =300 m/s, anomaly shear wave velocity $\boldsymbol{V_s}$= 150 m/s, depth $\boldsymbol{D}$ = 16 m, length $\boldsymbol{L}$ = 9 m.

Figure 3.24 shows more severe cases of undetectability by MASW, corresponding to stiffer anomalies than the background host. Again, each of the 6 red dots correspond to a parameterization of the prototype model, for which MASW failed to resolve the anomaly (the anomaly's impedance contrast is I =1.5). Specifically, the inserted table in Figure 3.24 summarizes the 6 sets of parameters. Figure 3.25-Figure 3.30 depict the FWI results for the 6 cases MASW did not succeed (the inclusion thickness was T=1 m in all cases).

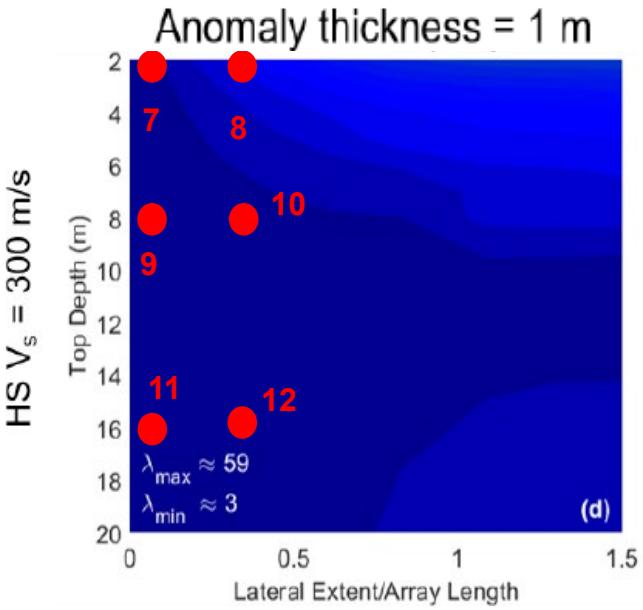

Case number (I = 1.5)	Anomaly Depth D	Anomaly Lateral Extent L
7	2 m	3 m
8	2 m	9 m
9	8 m	3 m
10	8 m	9 m
11	16 m	3 m
12	16 m	9 m

Figure 3.24: Red dots indicate MASW detectability failure cases; the table shows the subsurface anomaly parameters used in each one of the MASW failure cases (7-12).

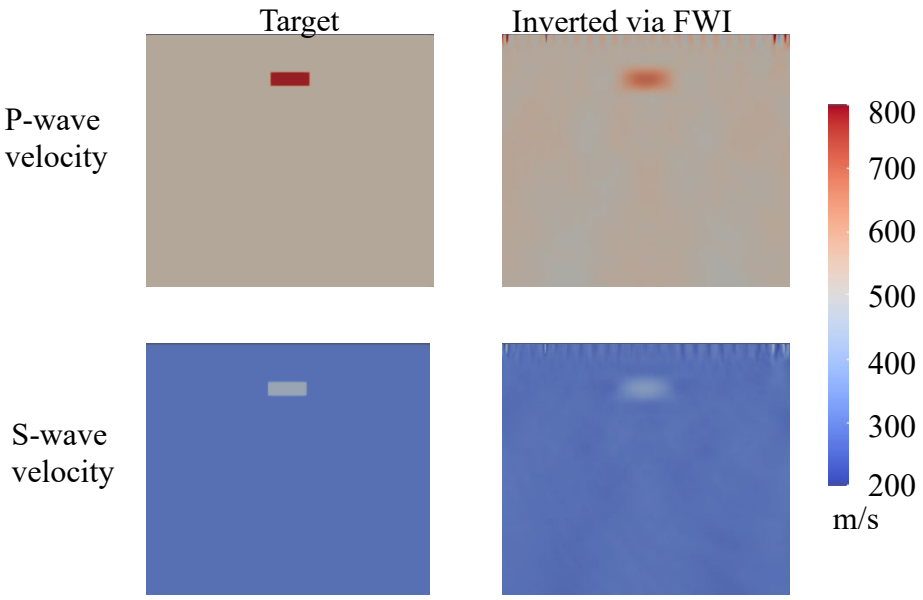

Figure 3.25: FWI imaging for Case 7: host shear wave velocity $\boldsymbol{V_{s-HS}}$ =300 m/s, anomaly shear wave velocity $\boldsymbol{V_s}$= 450 m/s, depth $\boldsymbol{D}$ = 2 m, length $\boldsymbol{L}$ = 3 m.

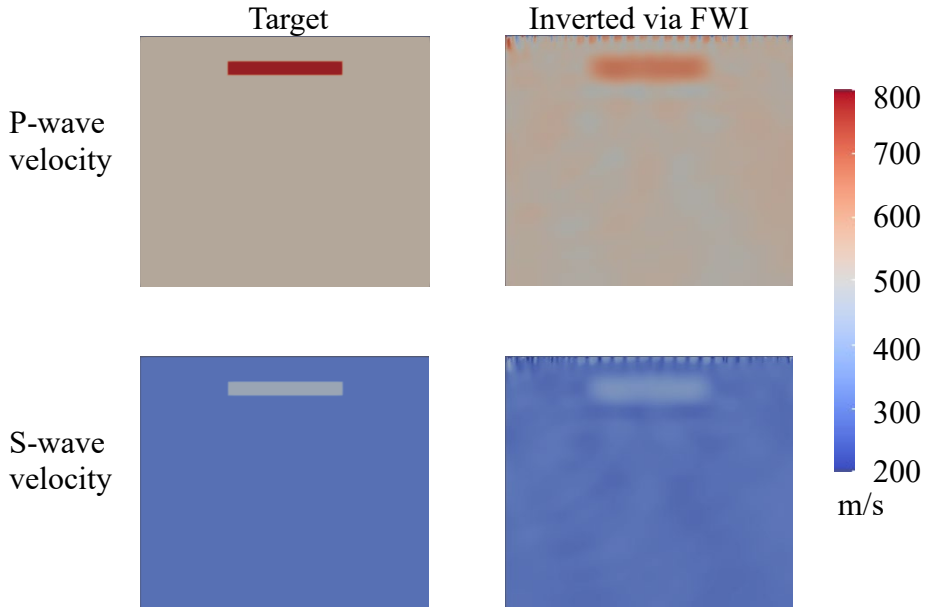

Figure 3.26: FWI imaging for Case 8: host shear wave velocity $\boldsymbol{V_{s-HS}}$ =300 m/s, anomaly shear wave velocity $\boldsymbol{V_s}$= 450 m/s, depth $\boldsymbol{D}$ = 2 m, length $\boldsymbol{L}$ = 9 m.

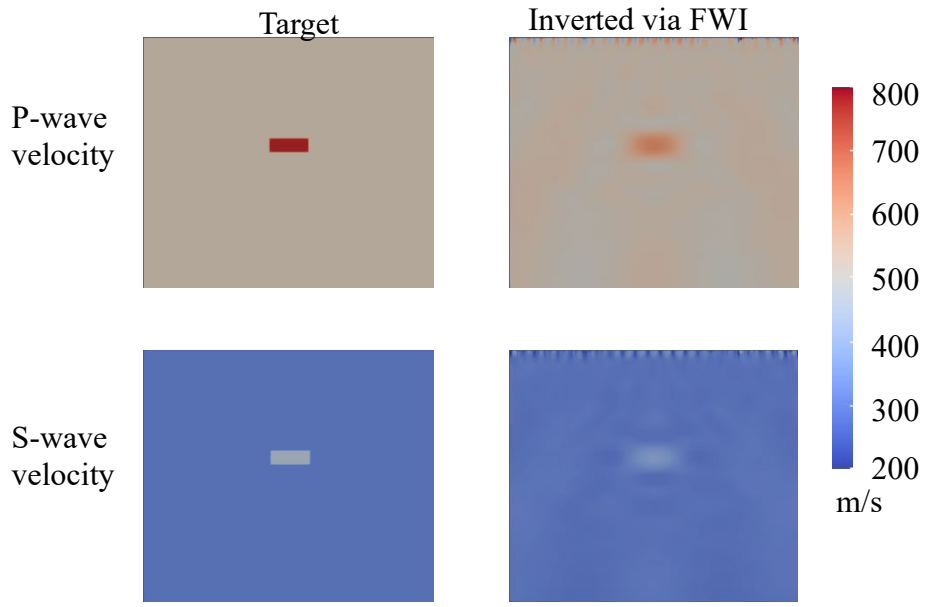

Figure 3.27: FWI imaging for Case 9: host shear wave velocity $\boldsymbol{V_{s-HS}}$ =300 m/s, anomaly shear wave velocity $\boldsymbol{V_s}$= 450 m/s, depth $\boldsymbol{D}$ = 8 m, length $\boldsymbol{L}$ = 3 m.

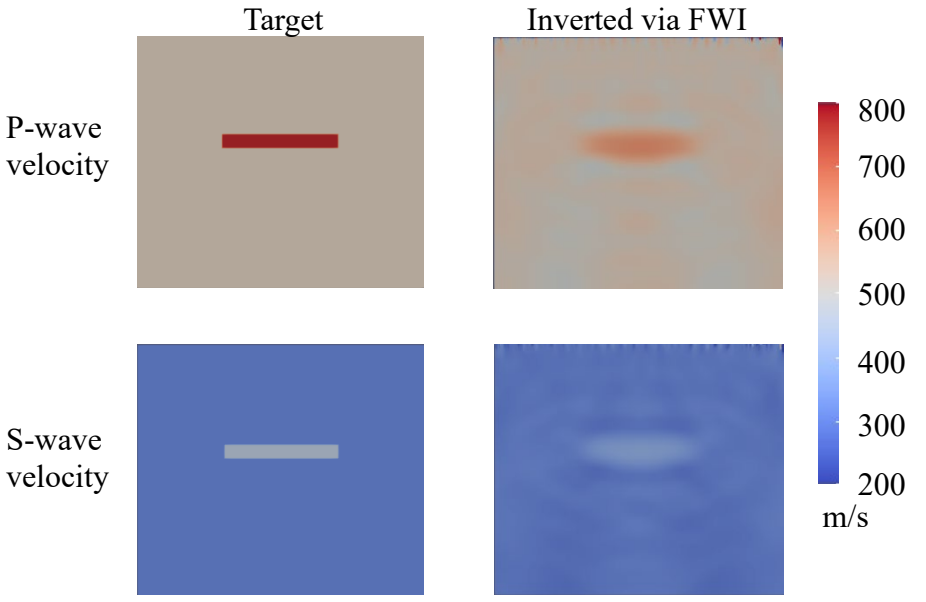

Figure 3.28: FWI imaging for Case 10: host shear wave velocity $\boldsymbol{V_{s-HS}}$ =300 m/s, anomaly shear wave velocity $\boldsymbol{V_s}$= 450 m/s, depth $\boldsymbol{D}$ = 8 m, length $\boldsymbol{L}$ = 9 m.

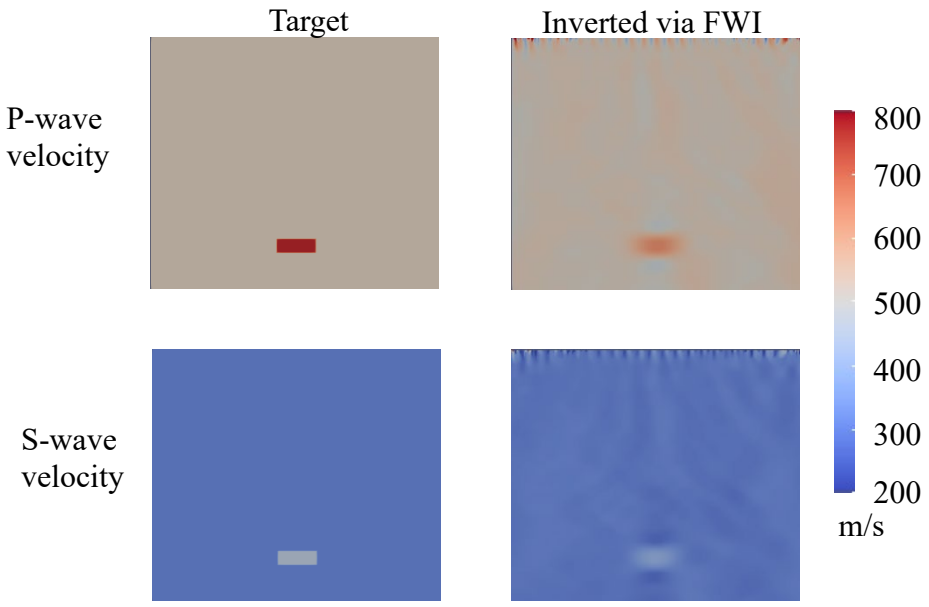

Figure 3.29: FWI imaging for Case 11: host shear wave velocity $\boldsymbol{V_{s-HS}}$ =300 m/s, anomaly shear wave velocity $\boldsymbol{V_s}$= 450 m/s, depth $\boldsymbol{D}$ = 8 m, length $\boldsymbol{L}$ = 3 m.

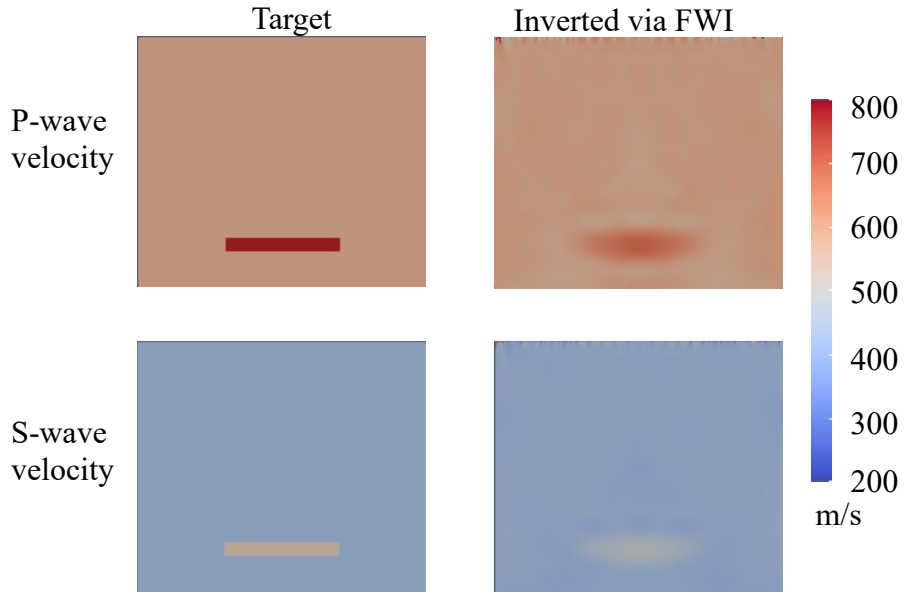

Figure 3.30: FWI imaging for Case 12: host shear wave velocity $\boldsymbol{V_{s-HS}}$ =300 m/s, anomaly shear wave velocity $\boldsymbol{V_s}$= 450 m/s, depth $\boldsymbol{D}$ = 16 m, length $\boldsymbol{L}$ = 9 m.

Figure 3.31 shows additional cases, corresponding to softer anomalies than the background host. In these cases, the anomaly's impedance contrast was I =0.5. Specifically, the table in Figure 3.31 summarizes the 4 sets of parameters. Figure 3.32-Figure 3.35 depict the FWI results for the 4 cases (the inclusion thickness was T=4 m in all cases).

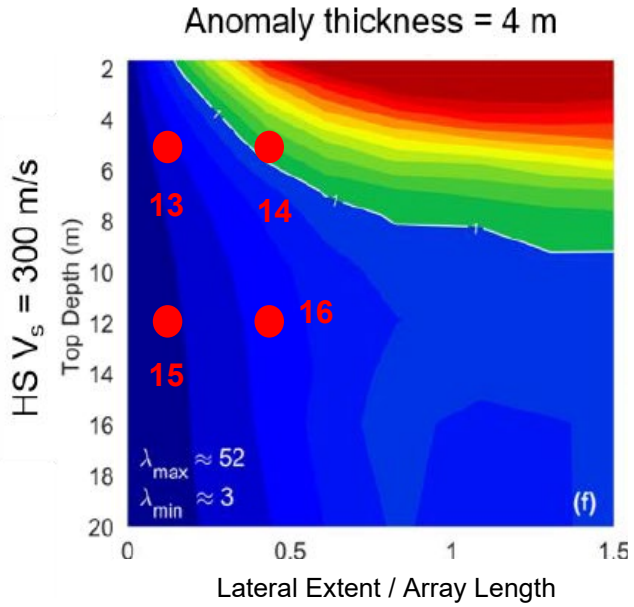

Case number (I = 0.5)	Anomaly Depth D	Anomaly Lateral Extent L
13	5 m	3 m
14	5 m	9 m
15	12 m	3 m
16	12 m	9 m

Figure 3.31: Red dots indicate MASW detectability failure cases; the table shows the subsurface anomaly parameters used in each one of the MASW failure cases (13-16).

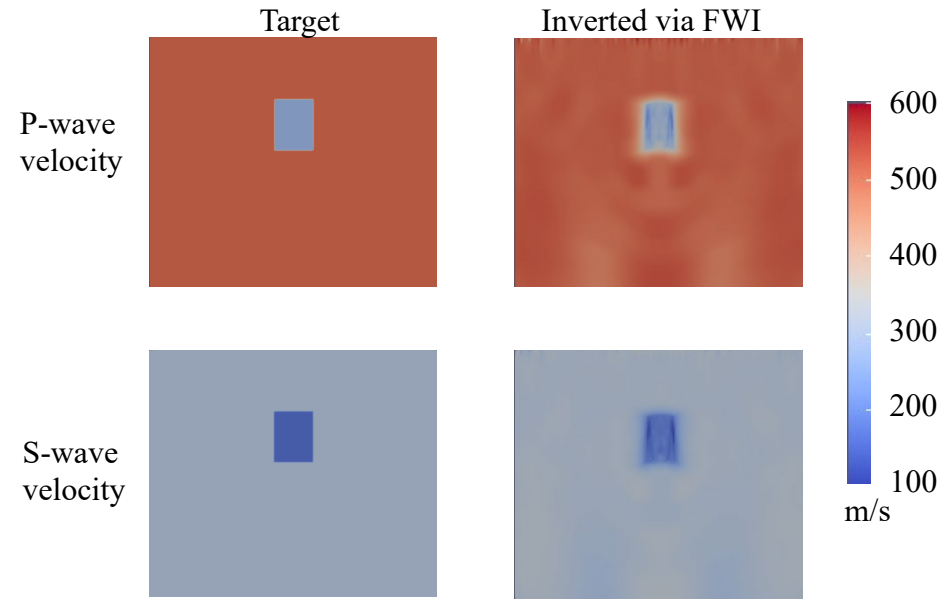

Figure 3.32: FWI imaging for Case 13: host shear wave velocity $\boldsymbol{V_{s-HS}}$ =300 m/s, anomaly shear wave velocity $\boldsymbol{V_s}$= 150 m/s, depth $\boldsymbol{D}$ = 5 m, length $\boldsymbol{L}$ = 3 m.

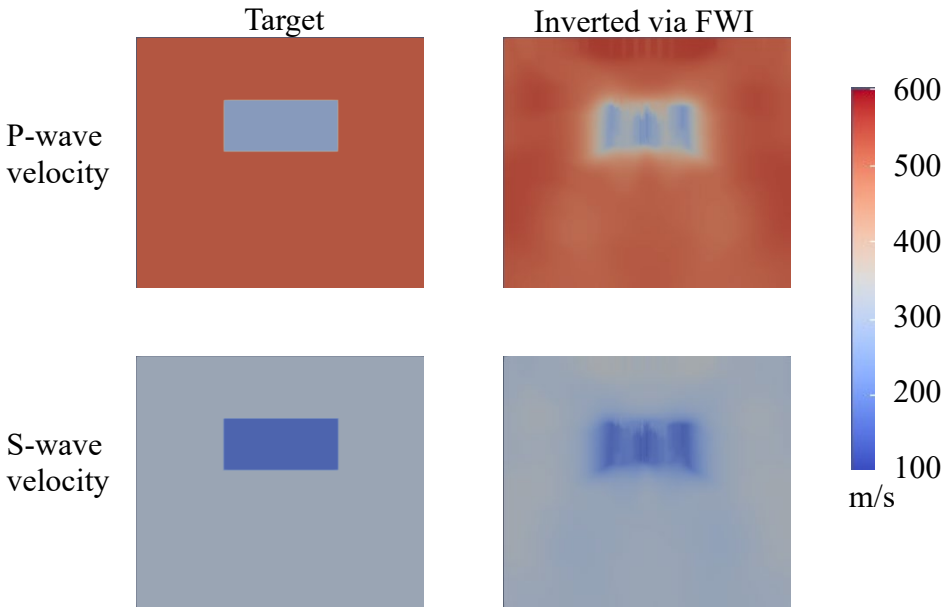

Figure 3.33: FWI imaging for Case 14: host shear wave velocity $\boldsymbol{V_{s-HS}}$ =300 m/s, anomaly shear wave velocity $\boldsymbol{V_s}$= 150 m/s, depth $\boldsymbol{D}$ = 5 m, length $\boldsymbol{L}$ = 9 m.

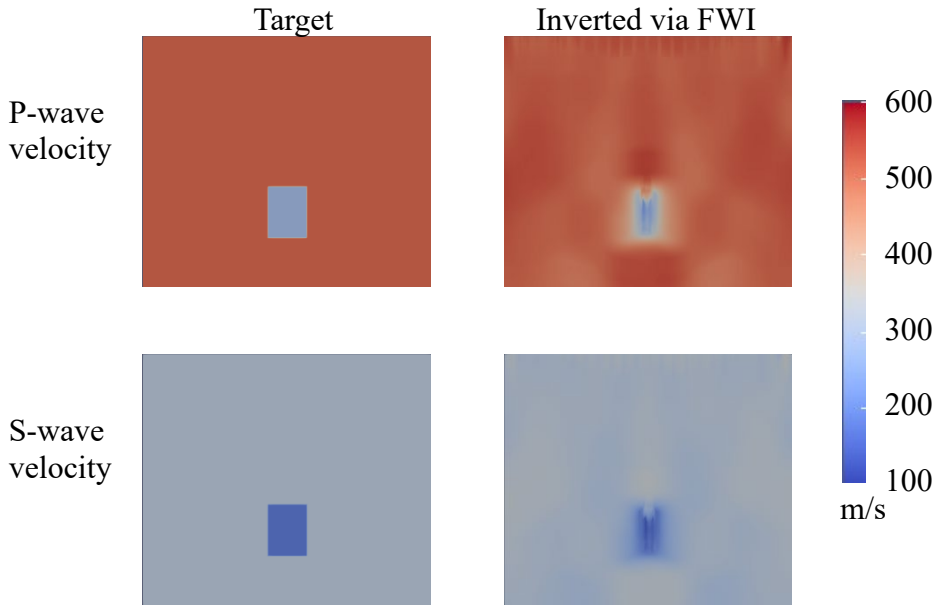

Figure 3.34: FWI imaging for Case 15: host shear wave velocity $\boldsymbol{V_{s-HS}}$ =300 m/s, anomaly shear wave velocity $\boldsymbol{V_s}$= 150 m/s, depth $\boldsymbol{D}$ = 16 m, length $\boldsymbol{L}$ = 3 m.

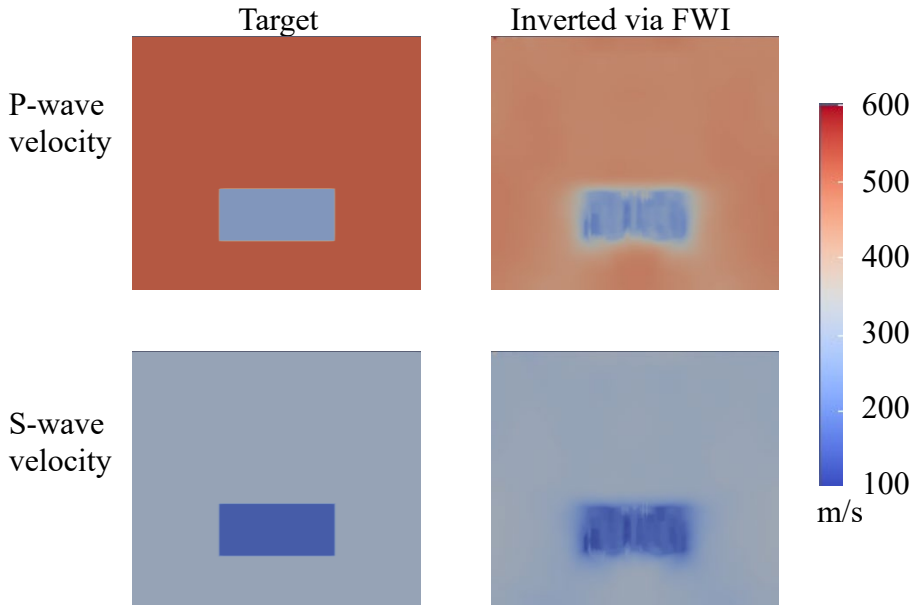

Figure 3.35: FWI imaging for Case 16: host shear wave velocity $\boldsymbol{V_{s-HS}}$ =300 m/s, anomaly shear wave velocity $\boldsymbol{V_s}$= 150 m/s, depth $\boldsymbol{D}$ = 16 m, length $\boldsymbol{L}$ = 9 m.

From the sample cases, it is evident that FWI was able to detect the anomaly and satisfactorily estimate the compressional and shear wave velocities of the anomaly and of the background host at thousands of (discrete) material points in the subsurface.

We note that while the presented cases pertained to cases where the anomaly's strong axis is parallel to the ground surface, FWI performs equally well in the more challenging cases of inclined or vertically-oriented anomalies as Figure 3.36 and Figure 3.37 show.

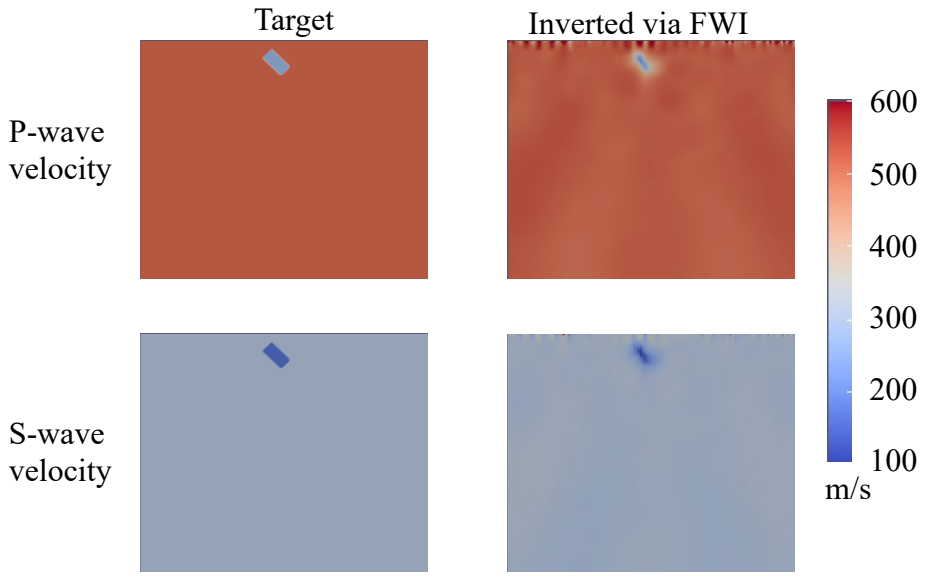

Figure 3.36: imaging for an inclined anomaly: host shear wave velocity $\boldsymbol{V_{s-HS}}$ =300 m/s, anomaly shear wave velocity $\boldsymbol{V_s}$= 150 m/s, thickness $\boldsymbol{T}$ = 1 m, length $\boldsymbol{L}$ = 3 m.

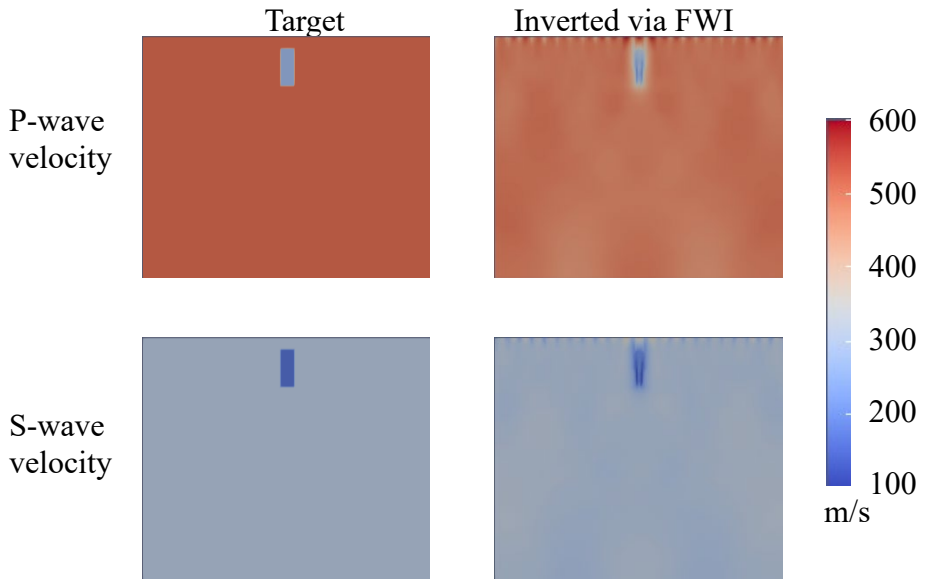

Figure 3.37: FWI imaging for a vertical anomaly: host shear wave velocity $\boldsymbol{V_{s-HS}}$ =300 m/s, anomaly shear wave velocity $\boldsymbol{V_s}$= 150 m/s, thickness $\boldsymbol{T}$ = 1 m, length $\boldsymbol{L}$ = 3 m.

The reconstruction of very soft inclusions (tantamount to voids) is also satisfactory, as the case shown in Figure 3.38 exemplifies for which the target inclusion has shear wave velocity of 30 m/s.

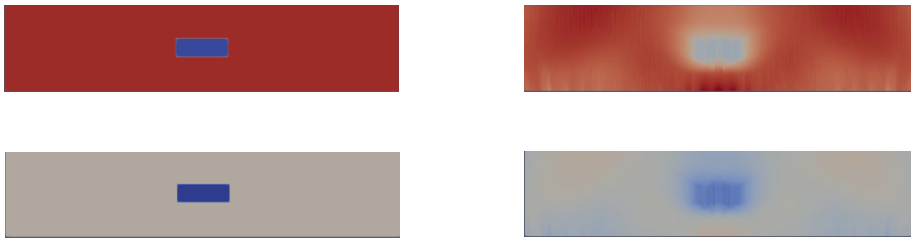

Figure 3.38: Ultra soft inclusion imaging using FWI.

In summary, the FWI numerical experiments with synthetic data confirmed the method's capabilities of resolving anomalies of various sizes, at various depths, both softer and harder than the host background. The usual interplay between detectable size and wavelength apply here as well: the ability of the method to resolve anomalies is limited only by the agility of the probing source in generating probing signals at wavelengths that are of the order of the targeted anomaly size. If the anomaly size is 2-5 times smaller than the smallest wavelength present in the probing

signals, detection becomes onerous (still not impossible, but it depends on the heterogeneity of the formation).

3.4. Summary of Findings – Synthetic Studies

We conducted numerical experiments using forward models encompassing subsurface anomalies to generate synthetics at sensor locations, which we then used to invert for the subsurface properties. We experimented with ERT in 2D and 3D, with MASW in 2D, and with FWI in 2D. In summary:

- ERT 2D, using EarthImager2D for the inversion, appears to reliably detect subsurface anomalies, for a wide range of sizes, at depths limited to 15%-20% of the array length. We note that, due to the smoothing EarthImager2D performs, the resistivity values in zones of strong property gradients will be, in general, inaccurate. In such cases, the imaging should be interpreted as providing an indication of an anomaly, but the very character of the anomaly (void versus inclusion) may not be readily decipherable; nor would the properties be accurate enough for a definitive mapping to a specific material.
- ERT 3D, using EarthImager3D for the inversion, proved to be challenging. While it is still possible to generate 3D images of the subsurface by combining 2D slices, direct 3D inversion proved to be problematic.
- MASW, due to the inherent theoretical constraints of the method, did not succeed in detecting subsurface anomalies for a wide range of cases, as expected.
- FWI 2D succeeded in imaging the subsurface, including anomalies, of various sizes and contrasting properties.

Chapter 4. Field Studies

In this Chapter, we review the results of field experiments conducted at two sites selected by the Texas Department of Transportation for the purposes of the project.

The first test site was in Georgetown, Texas (Figure 4.1), at approximately 30.631996ºN, -97.761407ºW (latitude, longitude). The test site was a small patch of mostly flat-surface land, sandwiched between Texas State Highway 29 (eastbound) and the Crescent Bluff Subdivision. The field tests for all four methods (ERT, MASW, FWI, and GPR) were conducted 6/29/2021 and 6/30/2021. Subsequently, in December 2022, a few boreholes were drilled at select locations to verify or refute the presence of suspected voids.

Figure 4.1: Aerial view of the Georgetown (GTWN) field experiment site; the yellow rectangle is the ground surface trace of the probed volume.

The second test site was at East Oak Hill, Texas Figure 4.2), at approximately 30.239211ºN, 97.829523ºW (latitude, longitude). The test site was sandwiched between Southwest Parkway and Texas State Highway 71. Similarly to the first test site, verification drilling took place also in December 2022.

Figure 4.2: Aerial view of the Southwest Parkway (SWPW) field experiment site; the yellow rectangle is the ground surface trace of the probed volume.

4.1. Field Experiments at Georgetown (GTWN)

At Georgetown we deployed ERT, MASW and FWI arrays. TxDOT conducted the GPR surveys, and an independent contractor at TxDOT's direction performed the verification drilling.

4.1.1. ERT – Field Studies (GTWN)

4.1.1.1. Testing Method and Locations

Geophysical testing to investigate potential voids along Texas State Highway 29 in Georgetown, TX was conducted using the Electrical Resistivity Tomography (ERT). Nine survey lines were conducted in the study (see Figure 4.3). Line X was conducted first and is approximately West-East (zero distance on the West end of the line) with a length of 110 meters (Figure 4.4). Lines A-H were conducted next and are also approximately West-East (zero distance on the West end of the line) with a length of 55 meters. Line A-H were conducted as parallel lines with a spacing between lines of approximately 2.0 meters (see Figure 4.3, Figure 4.5, Figure 4.6). However, Line G was located 2.2 meters from Line F and 1.8 meters from Line H in order to avoid a water line located parallel to the line. Ground photo of Line A is shown in Figure 4.6. The location of four water main valves on the site are shown in Figure 4.3. A surface opening (void opening) was

located at 36.5 meters along Line B and 43 meters along Line X. Overhead electrical service lines and other underground utilities were located throughout the project site. These tend to interfere with the measured resistivity values and may lead to anomalies in the subsurface and errors in the overall results.

The ERT data were collected using an Advanced Geosciences Inc. (AGI) SuperSting R8/IP Wifi resistivity meter (see Figure 4.7). For each survey, 56 surface electrodes were used with distances between electrodes of 2 meters for Line X and 1 meter for Line A-H. Passive electrode cables were connected to stainless steel stakes inserted 15-30 centimeters into the soil surface or through holes drilled in the shallow rock. The SuperSting resistivity meter controlled the injection of currents and the measurement of potentials using multiple channels. Contact resistance tests were performed before each survey and were generally less than 500 ohm-m with no values above 2000 ohm-m indicating excellent contact resistance at the site. Two-dimensional dipole–dipole and strong gradient survey configurations were used to collect data for each survey. The relative location of each electrode was surveyed using a Nikon Total Station with the true location of the end of each line surveyed using a Trimble Geo7x Centimeter GPS unit. More information regarding testing methods can be found in Rahimi et al. 2021 and 2018.

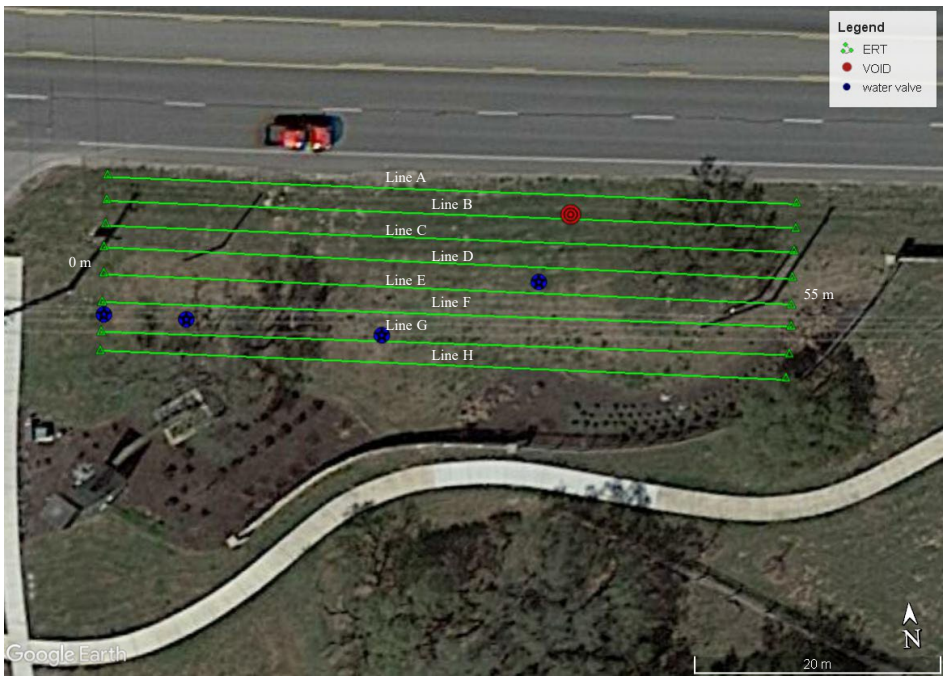

Figure 4.3: Georgetown site map showing ERT array lines (A-X).

Figure 4.4: Typical ERT line showing electrodes and their connectivity (line X).

Figure 4.5: Drone view of deployed ERT lines A-H.

Figure 4.6: Testing on ERT line A, while ERT lines B and C are in preparation.

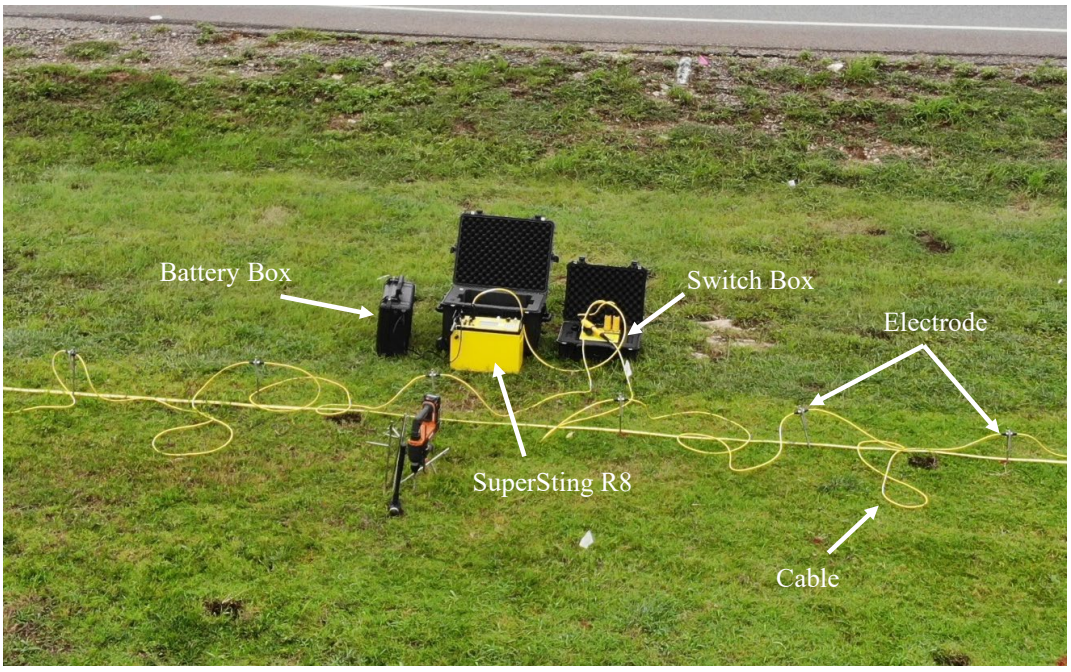

Figure 4.7: AGI data acquisition and injection equipment used for ERT testing.

4.1.1.2. Data Processing

2D Data Processing

The raw ERT data sets were inverted using AGI's EarthImager2D software. This program inverts measured resistivity data into a modeled distribution of true inverted resistivity values through iterative resistivity inversion algorithms. The resulting resistivity profile represents the resistivity distribution that best fits the measured data. However, resistivity inversion is indeterminate and non-unique, where many resistivity distributions could match the measured data equally well. Standard surface processing parameters suggested from AGI were used with a smooth inversion model used for all resistivity inversions, with a horizontal-to-vertical roughness factor of 0.5, a smoothness factor of 2, and a damping factor of 2. The minimum resistivity was set at 1 ohm-m and the maximum resistivity was set at 100,000 ohm-m. Electrode elevations from the total station were included in the inversions. After a preliminary inversion of each ERT profile, relative data misfit was used to remove individual points with >20-50% data misfit, based on the assumption that resistivity for adjacent measurements should not vary greatly. Up to 20% of measured data were removed following this criterion. The misfits between measured and modeled resistivity data for each profile, as measured by the root mean square error (RMSE), were minimized in the inversions. Inversions were considered complete after eight iterations or when an RMSE < 5-10% was reached, with the models converging in less than five iterations. The inversion procedure used a finite-element forward model with a Cholesky decomposition solver, six mesh divisions, and a thickness and depth factor of 1.1.

Pseudo 3D Data Processing

For the Pseudo 3D processing, the 2D raw resistivity for Lines A-H were combined in AGI's EarthImager3D software. This program was used to invert the combined resistivity data from the 2D lines. The resulting 3D resistivity model represents the resistivity distribution that best fits the measured data. However, as with 2D, 3D resistivity inversion is indeterminate and non-unique, where many resistivity distributions could match the measured data equally well. Standard surface processing parameters suggested from AGI were used with the parameters as used for the 2D data processing. Electrode elevations from the total station were included in the inversions. After a preliminary inversion, relative data misfit was used to remove individual points with >20-50%

data misfit, based on the assumption that resistivity for adjacent measurements should not vary greatly. Up to 20% of measured data were removed following this criterion. The misfits between measured and modeled resistivity data for each profile, as measured by the root mean square error (RMSE), were minimized in the inversions. Inversions were considered complete after eight iterations or when an RMSE < 5-10% was reached, with the models converging in less than five iterations. The inversion procedure used a finite-element forward model, two mesh divisions, and a thickness and depth factor of 1.1.

4.1.1.3. Interpretation and Results

The results of the ERT measurements for each survey line and the 3D model results are provided in this section. Please refer to Figure 4.3 for the location and orientation of each line. The elevation of each 2D cross section or model is based on the relative elevation of the site with zero elevation set as the highest measured elevation on the site.

Survey Line X

Shown in Figure 4.8 is the 2D resistivity cross section for Line X. For this cross section, a low near surface resistivity area (blue) is observed for the top ~1-2 meters of the subsurface, which is underlain by a more resistive area (green) for 0-70 meters along the line. The higher resistivity section likely indicates rock materials. Within the rock materials, a higher resistivity (orange) anomaly is observed at approximately 39 meters along the line and approximately 3-7 meters deep, which may be an air filled void. Another less significant high resistivity area is observed at 52 meters, which may be an air filled void or a forming void. Also of interest is the low resistivity anomaly (blue) at approximately 45 meters along the line. This area could be a previous void that has infilled with soil. Lower resistivity is also observed at distances greater than 70 meters along the line, which may indicate a fault where bedrock is deeper than observed for distances less than 70 meters. This area also corresponds with the start of a large wall at the site, which may interfere with the measurement causing errors in the survey.

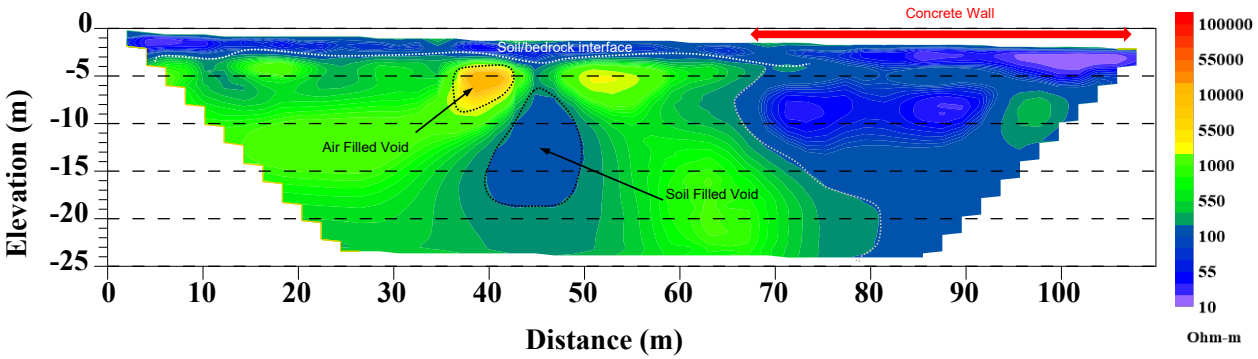

Figure 4.8: 2D cross-section of the subsurface resistivity below Line X.

Survey Line A

Shown in Figure 8 is the 2D resistivity cross section for Line A, which is the first in a series of parallel survey lines. For this cross section, a low near surface resistivity area (blue) is observed for the top ~1-2 meters of the subsurface, which is underlain by a more resistive area (green). A very high resistivity area is observed at 34 meters along the line with a depth from 2-5 meters below the surface. This area could be an air filled void. Other less significant high resistivity areas are observed at 15 meters, and 47 meters along the line, which may be forming voids or smaller air filled voids in the subsurface.

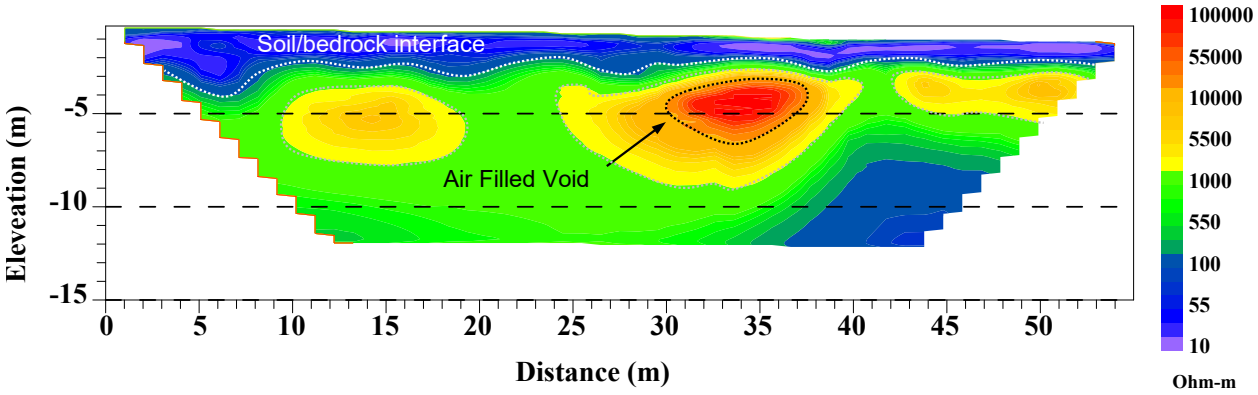

Figure 4.9: 2D cross-section of the subsurface resistivity below Line A.

Survey Line B

Shown in Figure 4.10 is the 2D resistivity cross section for Line B, which is 2 meters south and parallel to Line A. Similar to Line A, a low near surface resistivity area (blue) is observed for the top ~1 meter of the subsurface, which is underlain by a more resistive area (green). The same very high resistivity area is observed at 34 meters along the line at depth from 2-5 meters. Similar lesser high resistivity area are observed in this line as in Line A. A deeper low resistivity area is also observed in this line at 41 meters along the line. It extends from 3-7 meters below the surface and could be a previous void, which has filled with soil. This is also the line which is closest to the surface entrance observed on site.

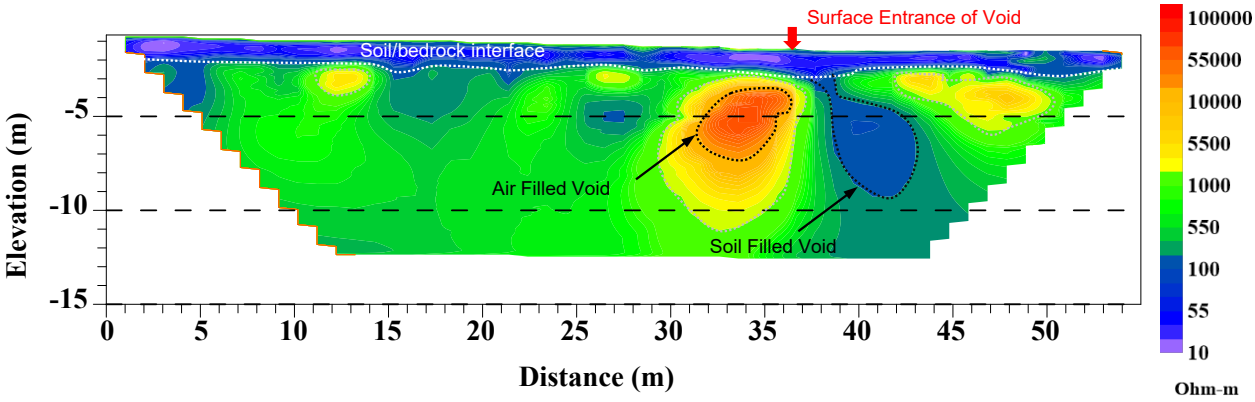

Figure 4.10: 2D cross-section of the subsurface resistivity below Line B.

Survey Line C

Shown in Figure 4.11 is the 2D resistivity cross section for Line C, which is 2 meters south and parallel to Line B. Similar to Line A and B, a low near surface resistivity area (blue) is observed for the top ~1 meter of the subsurface, which is underlain by a more resistive area (green). The same very high resistivity area is observed at 34 meters along the line at a deeper depth from 4-7 meters. This area has a lower resistivity than observed in lines A or B indicated the void is likely starting to disappear under this line. A low resistivity area is also observed in this line at 41 meters along the line, similar to line B. It extends from the surface to 8 meters below the surface and could be previous voids which have filled with soil.

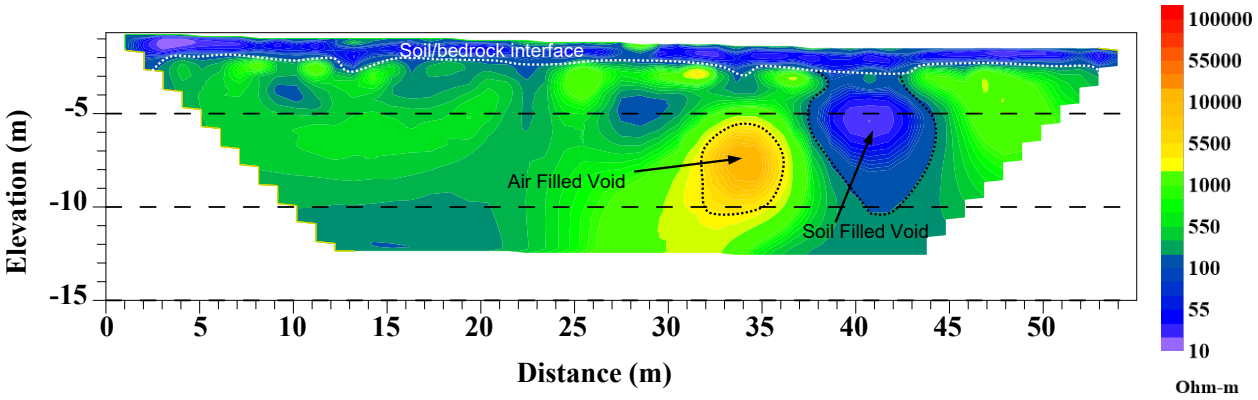

Figure 4.11: 2D cross-section of the subsurface resistivity below Line C.

Survey Line D

Shown in Figure 4.12 is the 2D resistivity cross section for Line D, which is 2 meters south and parallel to Line C. Similar to Line A-C, a low near surface resistivity area (blue) is observed for the top ~1 meter of the subsurface, which is underlain by a more resistive area (green). The same very high resistivity area observed in Lines A-C is disappearing in this line, indicating the void is likely not significant under this line. The low resistivity area observed in Lines B-C is more significant at 41 meters along this line. It extends from the surface to the maximum depth of the survey line and could be the center of a previous void, which has filled with soil. This is the line which is closest to the tree in the middle of the array.

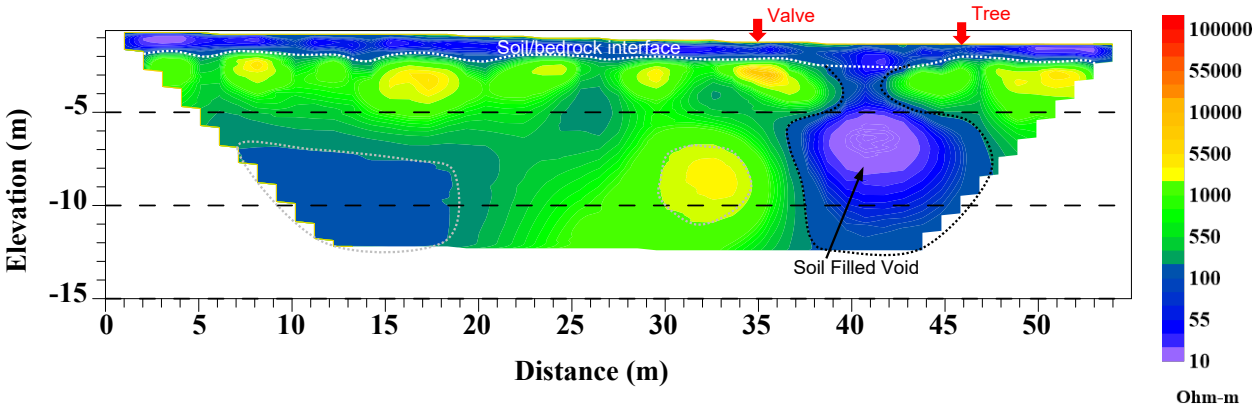

Figure 4.12: 2D cross-section of the subsurface resistivity below Line D.

Survey Line E

Shown in Figure 4.13 is the 2D resistivity cross section for Line E, which is 2 meters south and parallel to Line D. Similar to Line A-D, a low near surface resistivity area (blue) is observed for the top ~1 meter of the subsurface, which is underlain by a more resistive area (green). Some less significant higher resistivity areas (yellow) are observed along the line, which may indicate stiffer rock or potentially voids forming in the subsurface. The low resistivity area observed in Lines B-D is observed at 41 meters along this line. It extends from the surface to the maximum depth of the survey line. Another low resistivity area is observed at from 10-20 meters along with line at a deeper depth, which may be a soil filled void or interference from utilities in the area.

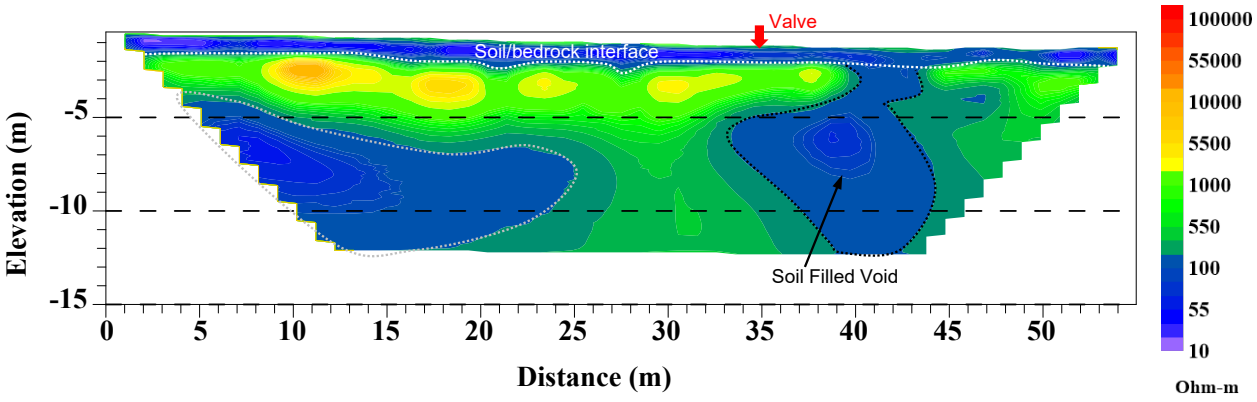

Figure 4.13: 2D cross-section of the subsurface resistivity below Line E.

Survey Line F

Shown in Figure 4.14 is the 2D resistivity cross section for Line F, which is 2 meters south and parallel to Line E. Similar to Line A-E, a low near surface resistivity area (blue) is observed for the top ~1 meter of the subsurface, which is underlain by a more resistive area (green). Some less significant higher resistivity areas (yellow) are observed along the line, which may indicate stiffer rock or potentially void forming in the subsurface. The low resistivity area observed in Lines B-E is observed at 41 meters along this line. It extends from 2-5 meters below the surface. Another low resistivity area is observed from 10-20 meters along the line at a deeper depth, which may be a soil filled void or interference from utilities in the area.

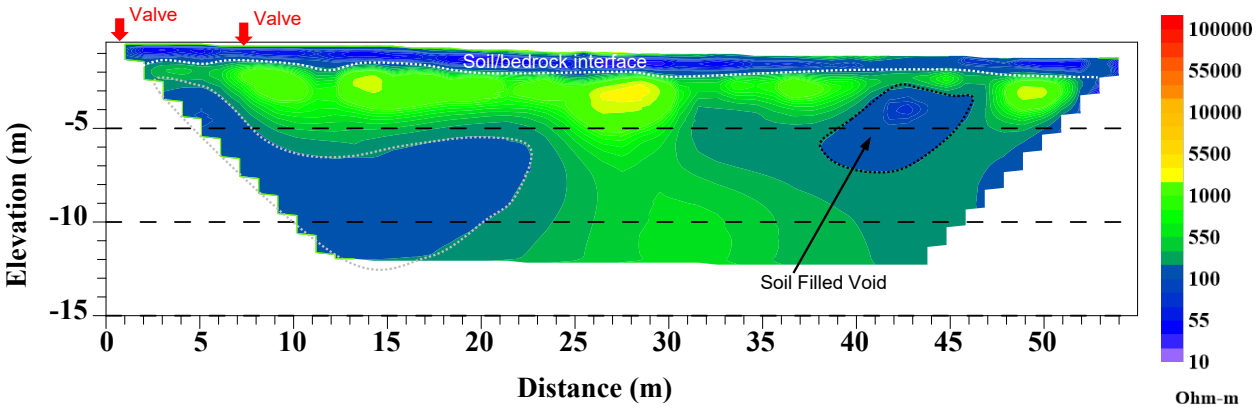

Figure 4.14: 2D cross-section of the subsurface resistivity below Line F.

Survey Line G

Shown in Figure 4.15 is the 2D resistivity cross section for Line G, which is 2.2 meters south and parallel to Line F. Similar to Line A-F, a low near surface resistivity area (blue) is observed for the top ~1 meter of the subsurface, which is underlain by a more resistive area (green). Deeper low resistivity areas are observed in the first section of the line and shallow low resistivity areas are observed at 25-35 meters along the line, which may be a soil filled void or interference from utilities in the area.

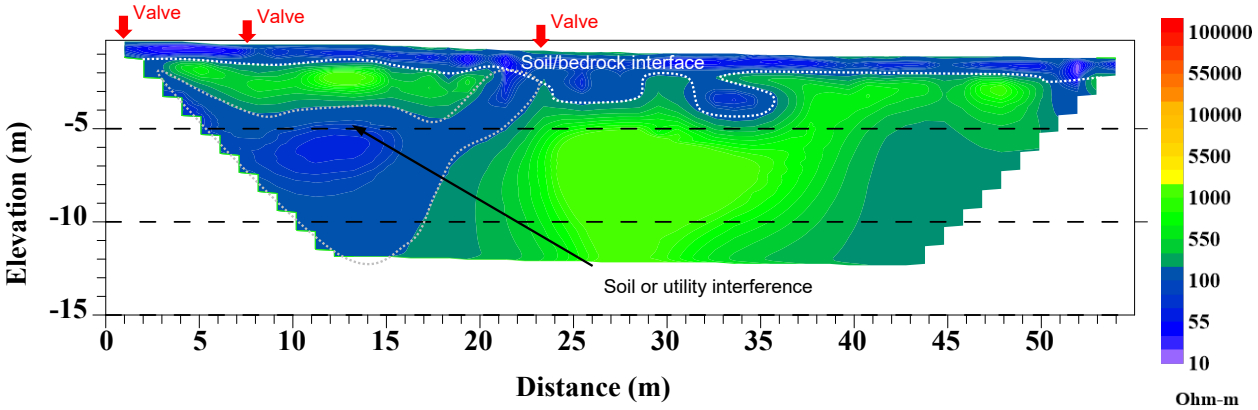

Figure 4.15: 2D cross-section of the subsurface resistivity below Line G.

Survey Line H

Shown in Figure 4.16 is the 2D resistivity cross section for Line H, which is 1.8 meters south and parallel to Line G. Similar to Line A-G, a low near surface resistivity area (blue) is observed for the top ~1 meter of the subsurface, which is underlain by a more resistive area (green). A higher resistivity area (yellow) is observed along the line at 33 meters which may indicate stiffer rock or potentially void forming in the subsurface. Deeper low resistivity areas are observed in the first section of the line, and shallow low resistivity areas are observed at 25-35 meters along the line, which may be a soil filled void or interference from utilities or trees in the area.

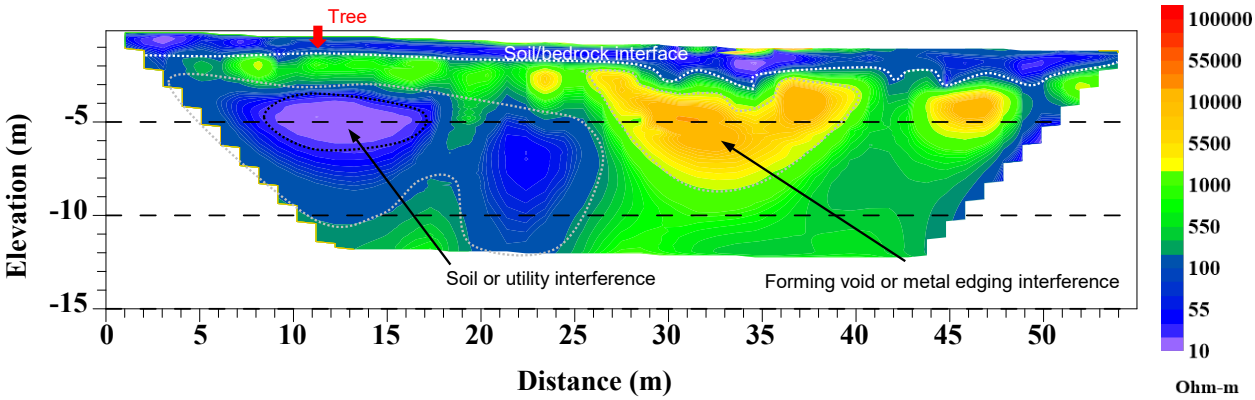

Figure 4.16: 2D cross-section of the subsurface resistivity below Line H

2D Combined Results

Shown in Figure 4.17 is an aerial view of the project site with the location and size of anomalies identified using the 2D resistivity analyses. These anomalies are either high resistivity, which are likely air filled voids or low resistivity, which are likely soil filled voids. The potential air filled voids are located under lines A-D (close to the road) with a depth between 2 and 7 meters depending on the anomaly. The potential soil filled void is located in the middle of the lines under lines B-F with a depth between 1 and 10 meters. An additional low resistivity anomaly is located on the south-west edge of the model. However, this resistivity anomaly is located near several water valves and trees, which may cause errors in the results.

Figure 4.17: Surface map of suspected void locations based on the 2D ERT analysis.

Pseudo 3D Results

Shown in Figure 4.18 is the pseudo 3D resistivity model for the site with high resistivity (>50,000 ohm-m) anomalies identified. There are three high resistivity anomalies in the subsurface are located under Lines A-D with distances of 17-22 meters, 27-35 meters, and 40-49 meters along the survey lines. The anomalies start at a depth of 2-3 meters and extend to 5-6 meters below the surface. The locations and sizes of the anomalies are similar to those identified using the 2D analyses.

Shown in Figure 4.19 is the pseudo 3D resistivity model for the site with low resistivity (< 125 ohm-m) anomalies identified. The primary anomaly is located under Lines B-E with a distance of 37-47 meters along the survey lines. The anomalies start at a depth of 1-2 meters and extend to 8-10 meters below the surface. The locations and sizes of the anomalies are similar to those identified

using the 2D analyses, with the exception that the large low resistivity anomalies under lines F-G near the start of the line were not resolved in this model.

Shown in Figure 4.20 is the pseudo 3D resistivity model for the site with high resistivity (>50,000 ohm-m) and low resistivity (< 125 ohm-m) anomalies identified. From this model, the 3rd high resistivity anomaly sits generally above the low resistivity anomaly.

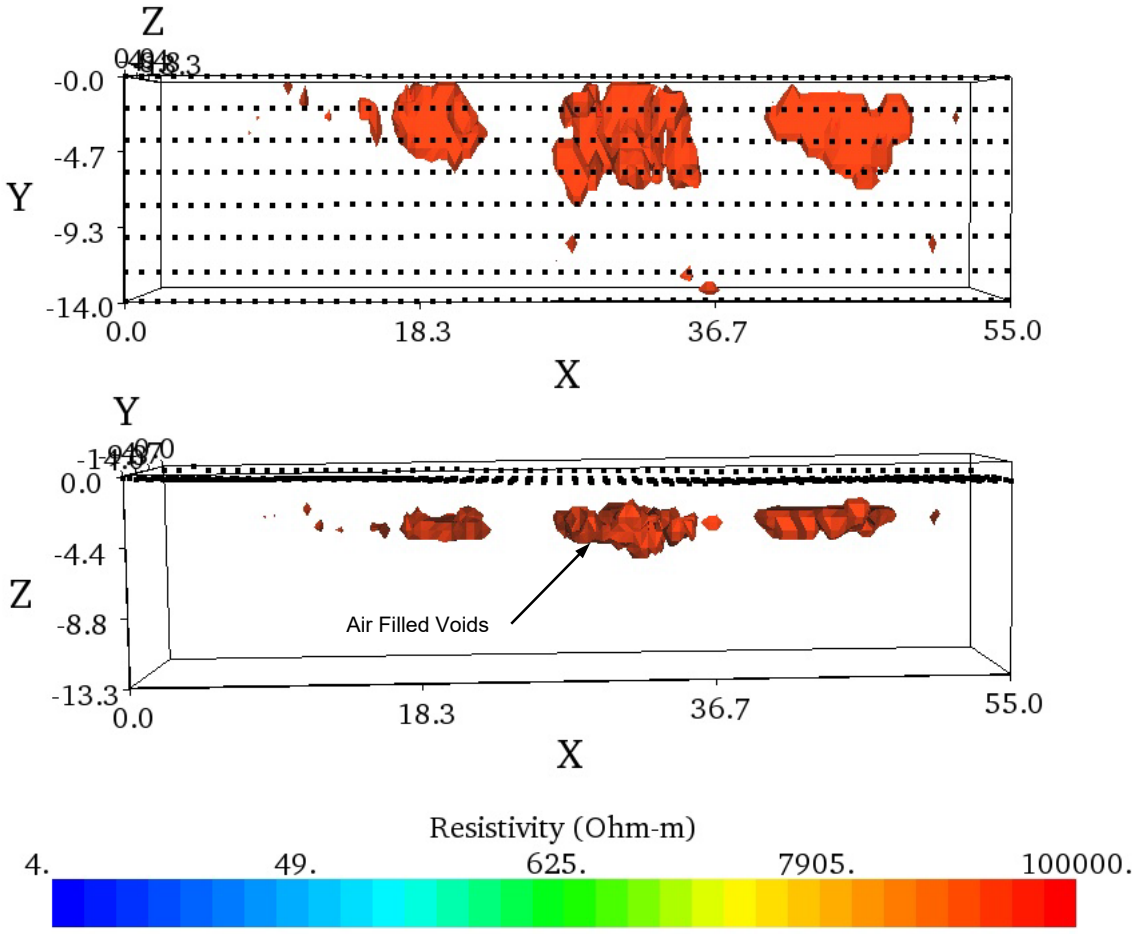

Figure 4.18: Pseudo 3D resistivity model with high resistivity (>50,000 ohm-m) areas of possible air-filled voids highlighted. Top figure is the top view and bottom figure is the profile view looking North.

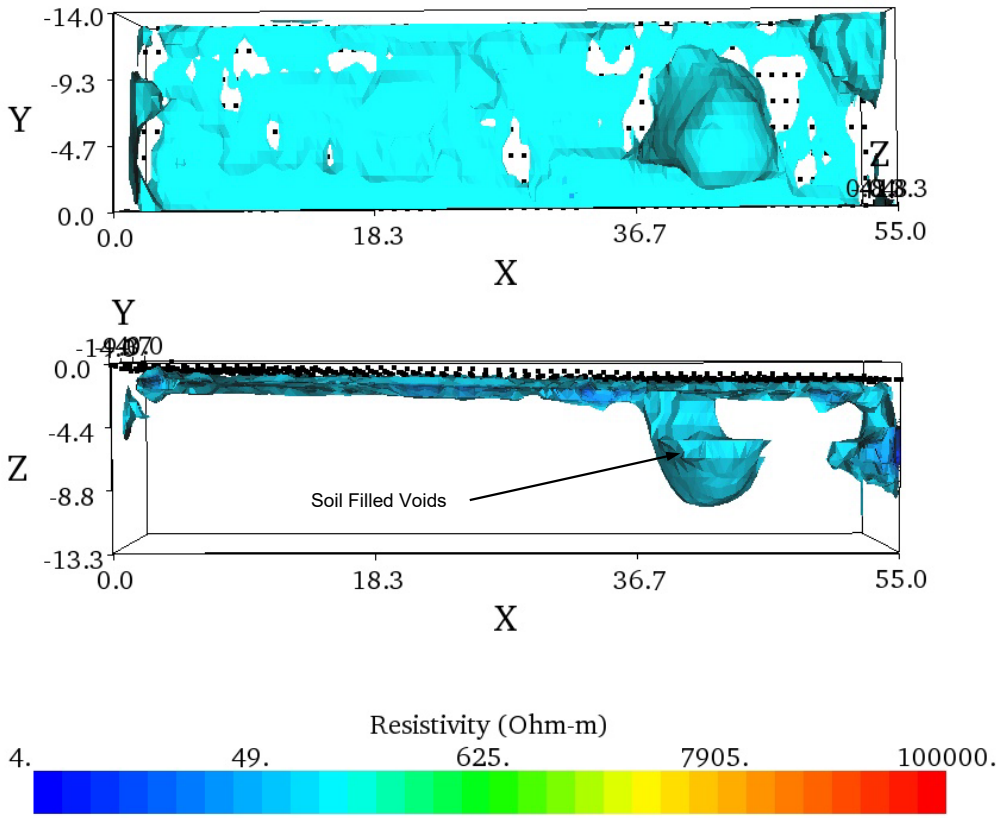

Figure 4.19: Pseudo 3D resistivity model with low resistivity (<125 ohm-m) areas of possible soil filled voids highlighted. Top figure is the bottom view and bottom figure is the profile view looking North.

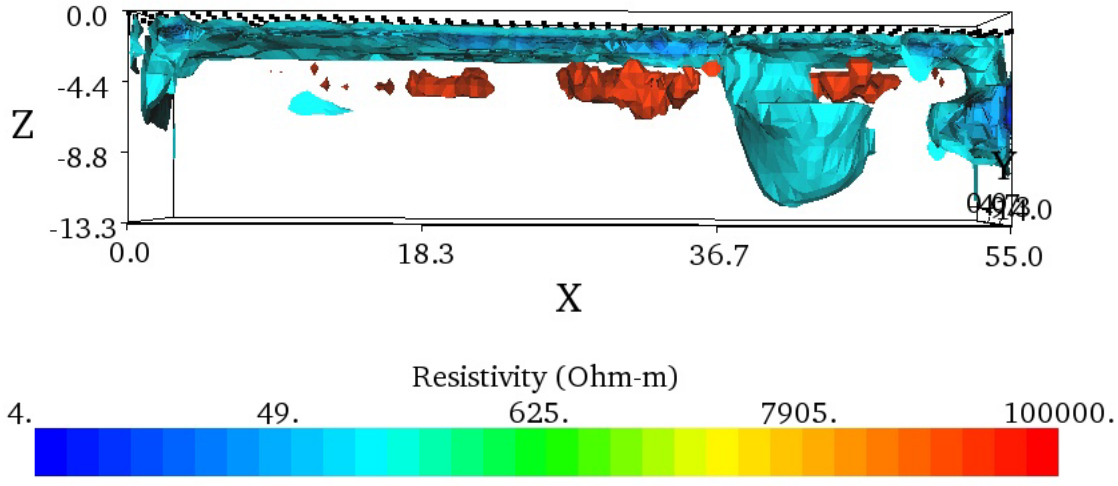

Figure 4.20: Pseudo 3D resistivity model with high resistivity (>50,000 ohm-m) and low resistivity (<125 ohm-m) areas highlighted.

Shown in Figure 4.21 is an aerial view of the project site with the location and size of anomalies identified using the Pseudo 3D resistivity analysis. These anomalies are either high resistivity, which are likely air-filled voids or low resistivity, which are likely soil filled voids. The potential air-filled voids are located under lines A-D (close to the road) with a depth between 2 and 6 meters depending on the anomaly. The potential soil-filled void is located in the middle of the lines under lines B-F with a depth between 2 and 10 meters. These void locations are similar to those identified using the 2D analyses. However, there are some differences in both the location and depth of the anomalies, which are due to the manner EarthImager processes the combined images.

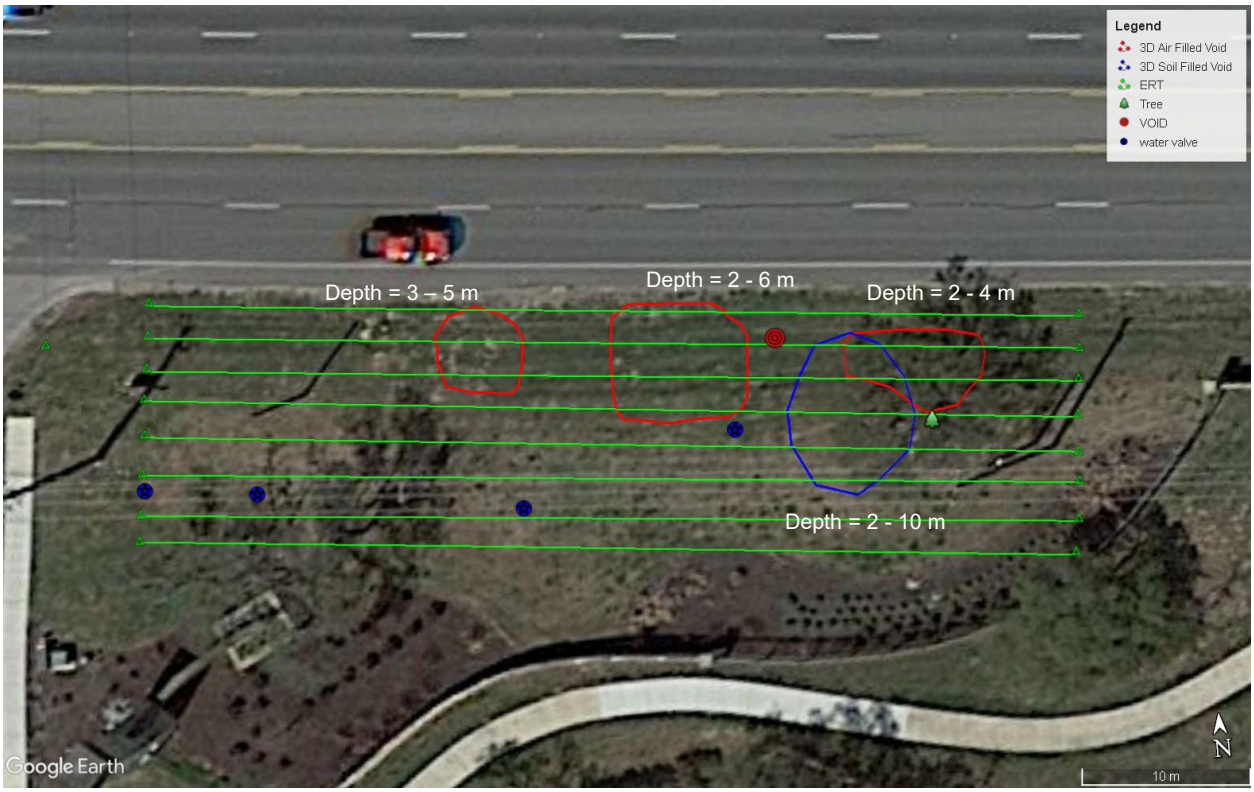

Figure 4.21: Surface map of suspected void locations based on the pseudo-3D ERT analysis.

4.1.1.4. Summary

Electrical Resistivity Tomography (ERT) was conducted to investigate possible voids along Texas State Highway 29 in Georgetown, TX. A total of nine lines were laid out on site with 8 parallel lines in the primary area of the site. Several high resistivity anomalies (possible air-filled voids) and low resistivity anomalies (possible soil-filled voids) were resolved across the site. The large

number of utilities (electric, water, irrigation, etc) likely interfered with the measurements and may have caused false anomalies at the site. These anomalies should be investigated using invasive drilling methods to determine the cause of the resistivity anomalies.

4.1.2. MASW and FWI – Field Studies (GTWN)

MASW geophone line arrays were deployed at the Georgetown site, using the same lines as the ERT surveys as shown in Figure 4.22.

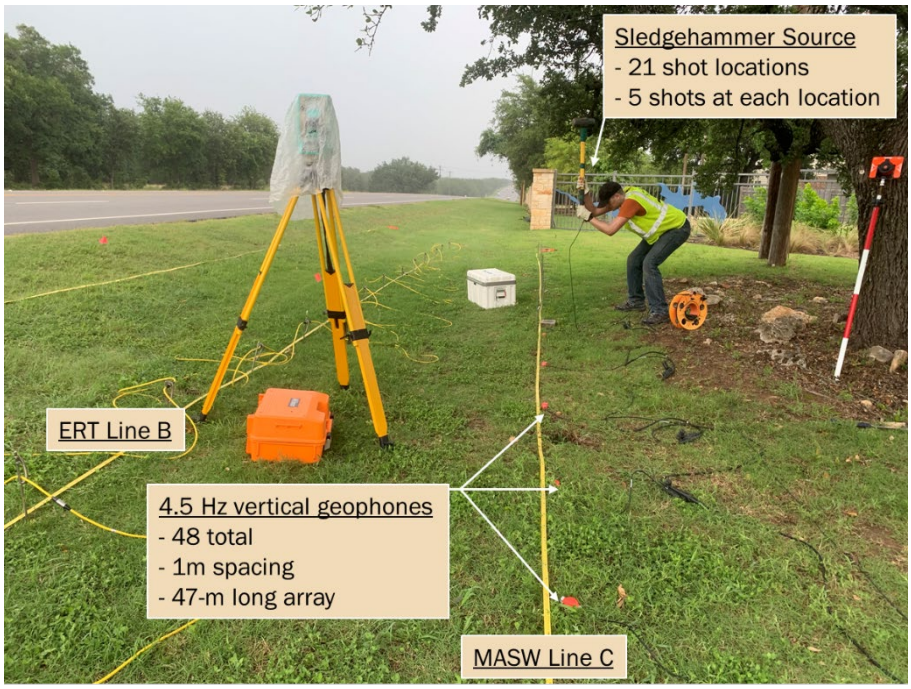

Figure 4.22: ERT and MASW survey lines at the Georgetown field experiment site.

A total of 48 4.5 Hz vertical geophones were deployed per array line at 1 m spacing for a total of 47 m-long array. We used a total of 21 shot locations, spaced 3 m apart, as shown in Figure 4.23. We used a sledgehammer as the source, and imparted 5 shots at each impact locations to improve the signal-to-noise ratio (SNR).

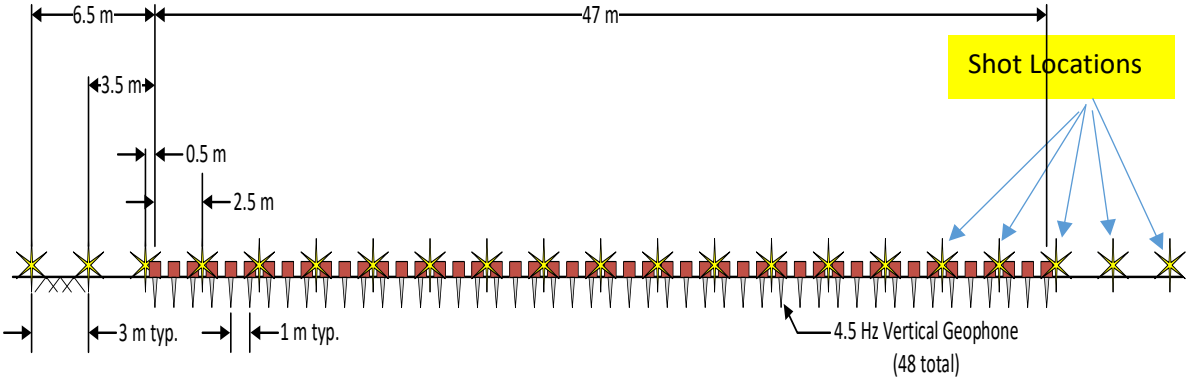

Figure 4.23: MASW geophone array showing shot locations, including offset, and geophone spacing.

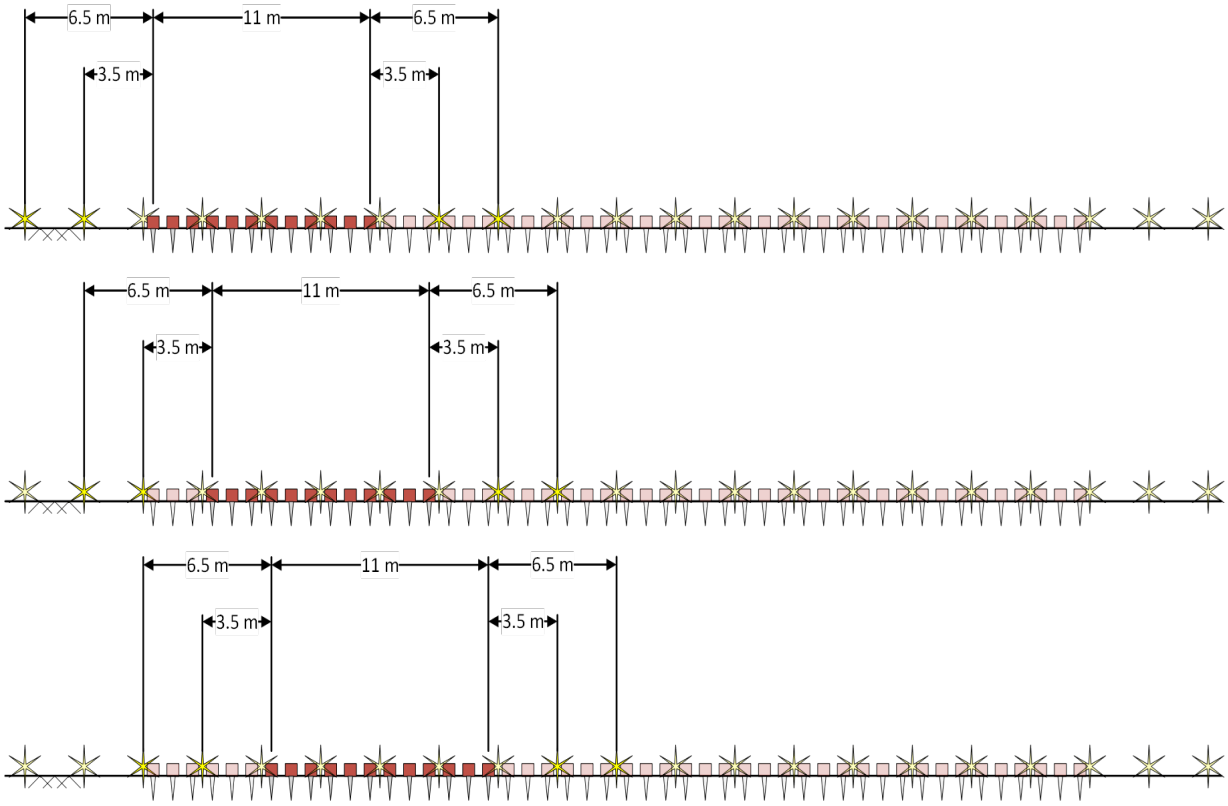

Figure 4.24: 12 geophone subarray marching scheme and associated shot locations.

We also used subarrays for pseudo-2D profiling, comprising 12 geophones at 1 m spacing, for a total subarray length of 11 m; 6 shot locations (at 0.5 m, 3.5 m, and 6.5 m off of the two ends of the subarray) were used; and each subarray was offset by 3 m; the subarray "marching" is shown in Figure 4.24.

Figure 4.25 shows subarray D1, where the source is at 6.5 m to the left of the array. Figure 4.26 shows the time traces, the SNR, and the dispersion curves resulting from the processing of subarray D1. In addition, Figure 4.26 shows the corresponding dispersion curves when the source is placed 6.5 m to the right of the subarray.

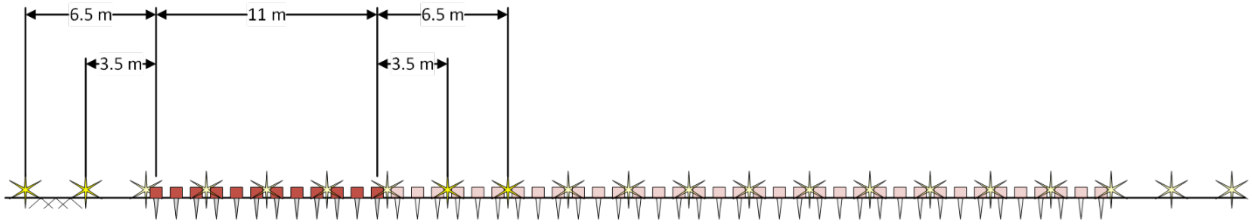

Figure 4.25: Subarray D1.

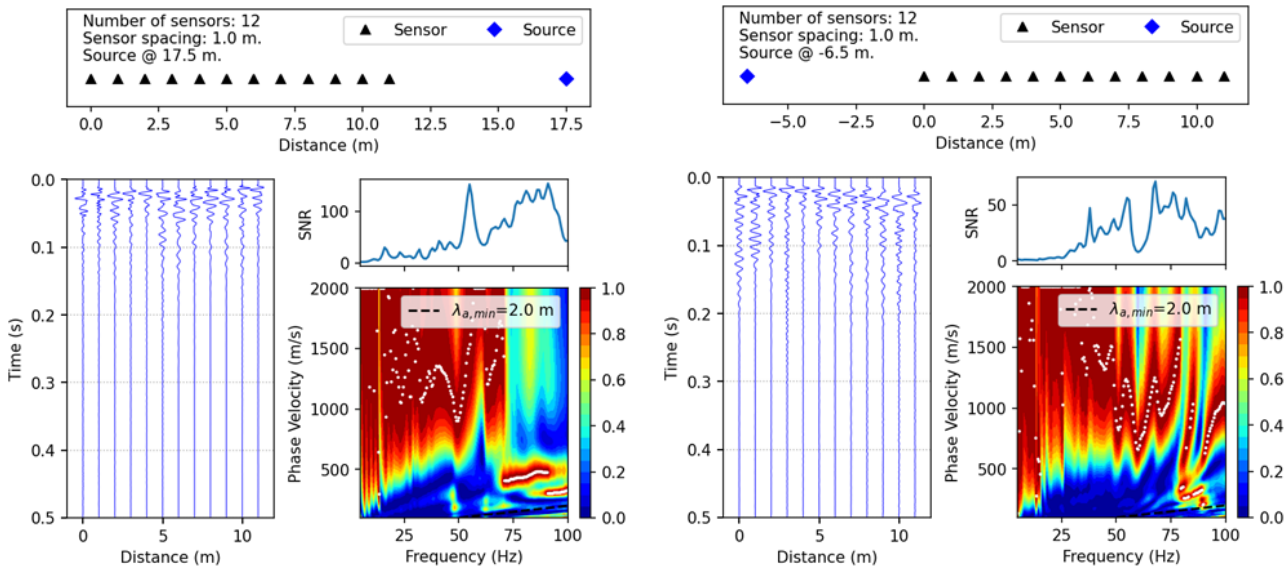

Figure 4.26: Time traces of subarray D1 geophone responses; signal-to-noise ratio; and dispersion data for two offset shot locations.

It is clear that the dispersion data are low quality or fairly noisy to be of assistance in inverting for the (presumed) layered slice of the subsurface under the array. In fact, subarray D1 is characteristic of the quality of the dispersion data resulting from the processing of other subarrays. For example, consider also subarray D8 (Figure 4.27): the resulting dispersion curves from two source locations, offset at 6.5 m to the left and to the right of the subarray are shown in Figure 4.28.

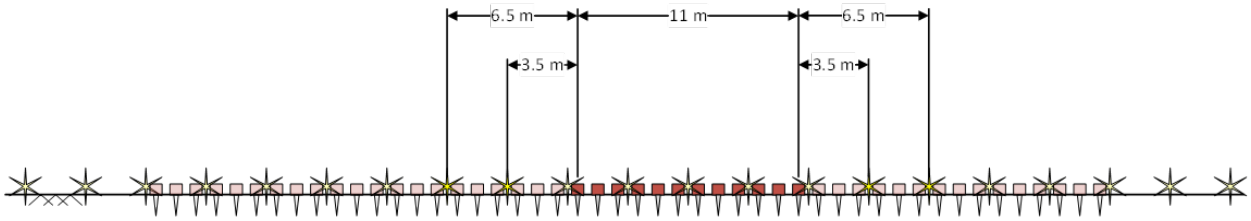

Figure 4.27: Subarray D8.

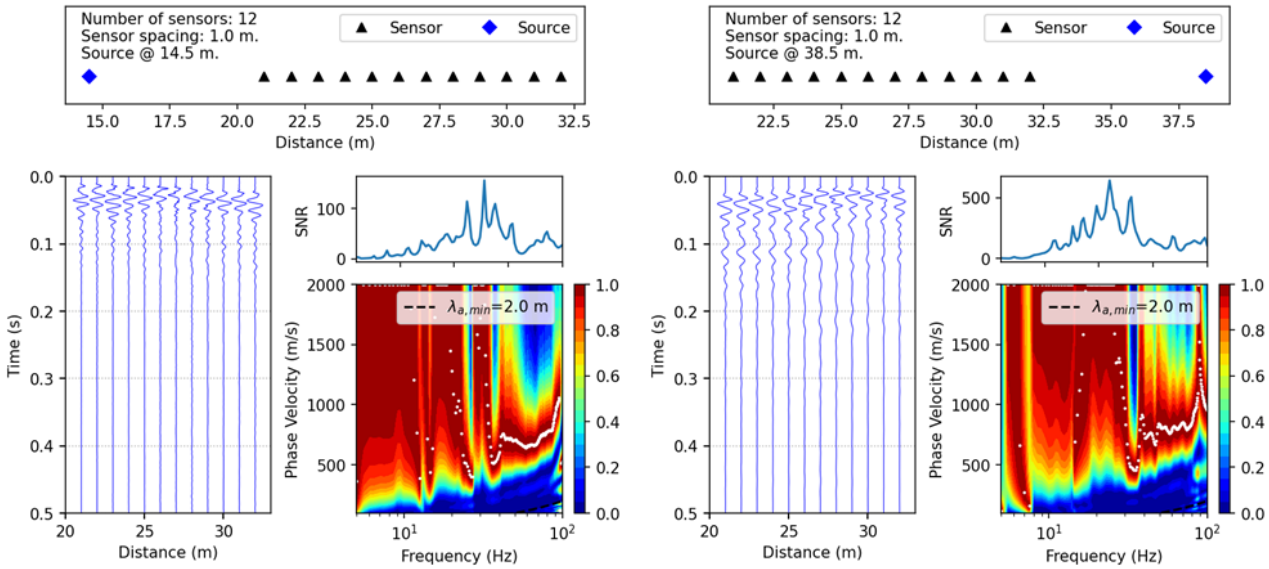

Figure 4.28: Time traces of subarray D8 geophone responses; signal-to-noise ratio; and dispersion data for two offset shot locations.

As it can be seen the experimental dispersion data cannot be processed. We note that the data collection took place during times of heavy traffic on Texas State Highway 29, just a few feet away from the array lines. We believe the noise introduced by the traffic to the data to have contributed to the low quality dispersion data.

At the same site, we also deployed a 2D surface array of geophones for FWI. The array comprised 64 4.5 Hz geophones deployed at the vertices of a 14 m by 14 m grid, with grid points spaced 2 m apart. We used 49 shot locations (5 shots per location); each source was set at the center of a grid square.

Figure 4.29: 2D FWI array at the Georgetown field experiment site; geophones are located at the grid vertices.

As previously mentioned, processing the FWI field data required the training of our research staff to the use of our in-house 3D FWI code, and that suitable modifications to the code be made, which, both, proved to be difficult to complete during the short project duration.

4.1.3. GPR – Field Studies (GTWN)

The GPR survey at Georgetown was conducted by a TxDOT contractor on July 1, 2021. Figure 4.30 depicts the GPR survey lines. We note that the GPR survey covered only a subarea of the ERT survey, as shown in Figure 4.30, starting roughly 18.5 m from the left origin of the ERT lines.

Figure 4.30: GRP scan lines at the Georgetown field experiment site.

For example, Figure 4.31 shows the subsurface resistivity map below ERT line A, where the white rectangle corresponds to scan 22 of the GPR survey, also shown in the figure.

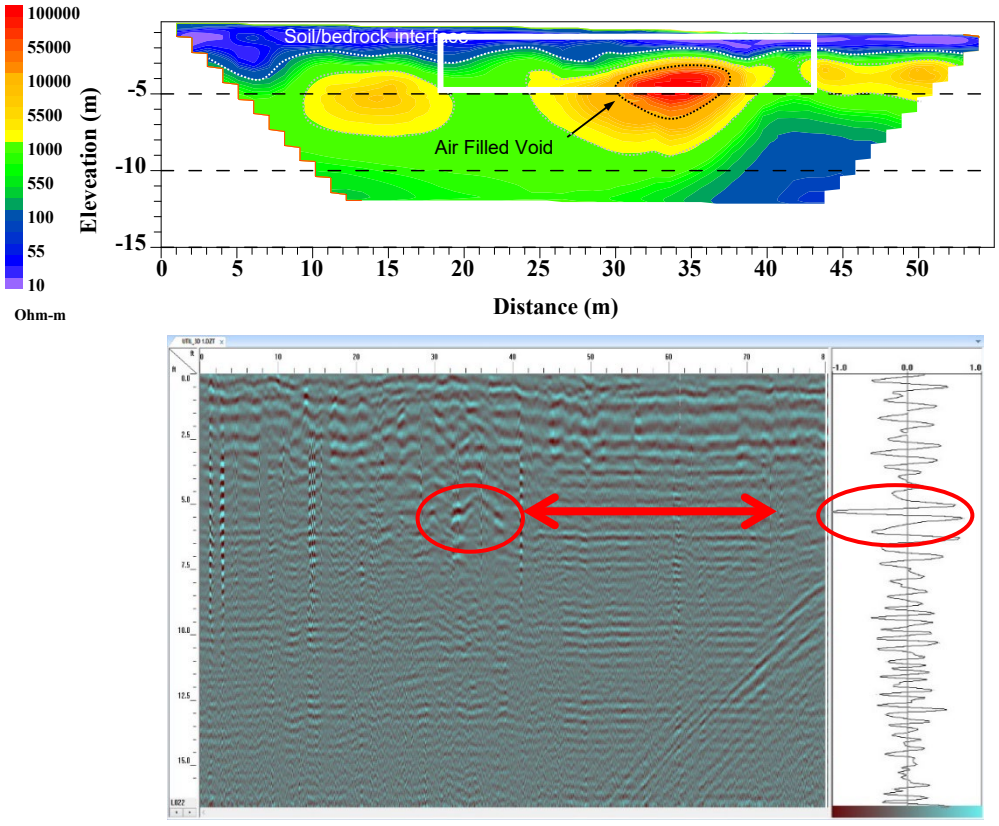

Figure 4.31: GPR radiogram (scan 22) overlapping with ERT line A (white rectangle). Possible void is highlighted in red on the radiogram. GPR void location does not match the ERT high resistivity zone.

The GPR operator noted a strong reflection in the scan 22 radiograms (dark spot), possibly indicating the presence of a void, at approximately 32.5 ft from the origin: the location corresponds to approximately 28.4 m from the origin of the ERT line. According to the ERT survey, this point may correspond to the boundary of the void identified in that location, whose center is still about 6 to 7 m to the right. Even if one were to consider the entire width of the noted reflection, from 32.5 ft to 38 ft as an indicator of a void (i.e., from 28.4 m to 30 m), the location appears shifted with respect to the ERT survey, which has placed the void between 30 m and 38 m. It is difficult to ascribe the discrepancy to one or the other method, absent verification with an invasive procedure (drilling). However, as it will become evident in the next section, where the findings from selective drilling are compared against the ERT survey, it appears that voids were found wherever the ERT survey suggested that they are.

Similarly, Figure 4.32 shows ERT line B, and the GPR scan 20 radiograms, where the operator has marked locations of likely anomalies. We note that the surface void, per the GPR, is located at 60 ft (18.3 m) from the origin of the GPR survey: the location corresponds to the 36.8 m point on the ERT line B (18.3 m + 18.5 m offset). The surface void was previously found to be at 36.5 m per the ERT survey: thus, there is near coincidence on the surface void between the two surveys. However, the agreement does not extend to other subsurface anomalies: consider for example, the operator's marks placed at 22 ft and 32.5 ft from the GPR origin. The locations correspond to points in the ERT surveys that are 25.2 m and 28.4 m from the ERT origin, respectively. There is nothing of note at 25.2 m in the ERT survey, whereas, again the 28.4 m location may indicate a void's boundary at best. We note also that the depth locations of the GPR radiogram's features do not match the ERT survey's features.

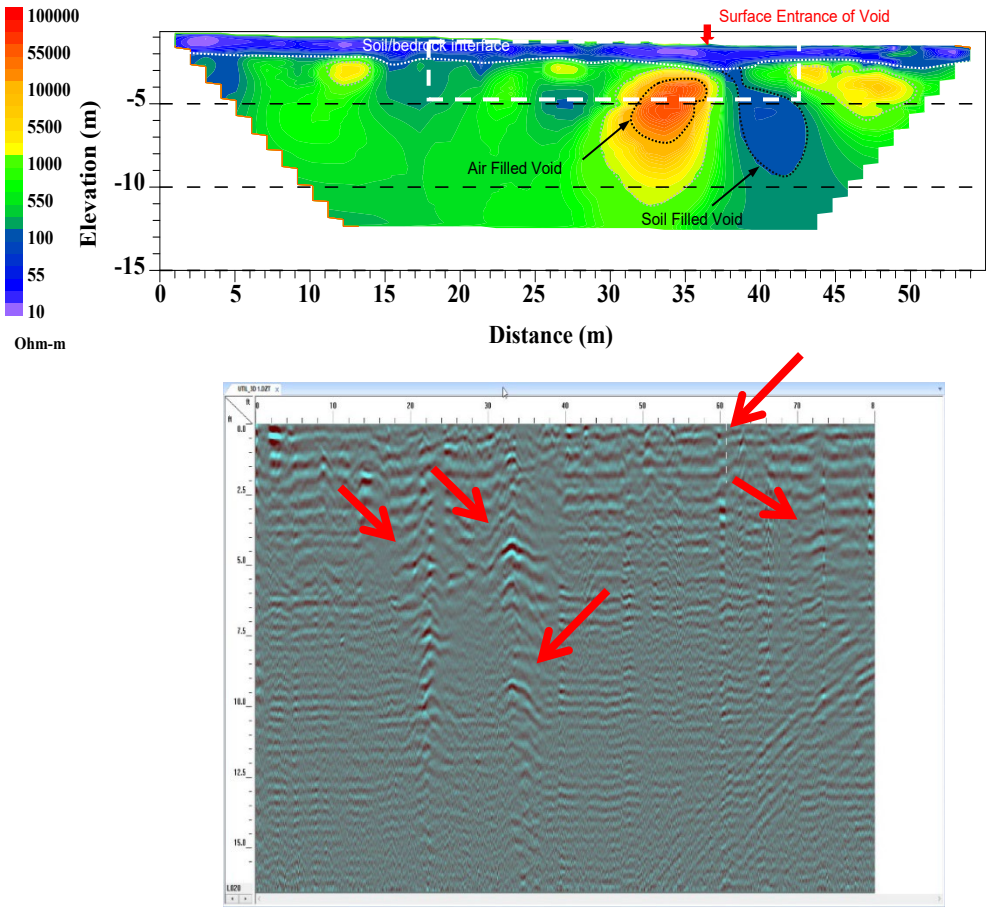

Figure 4.32: GPR radiogram (scan 22) overlapping with ERT line B (white rectangle). Possible voids and subsurface anomalies are indicated with red arrows on the GPR radiogram. In only one case (surface void – top left arrow) matches a finding in the ERT survey.

The above observations apply to the remainder of the GPR scans. Overall, there are differences between the ERT and GPR surveys

4.1.4. Verification Drilling (GTWN)

In December 2022, 5 borings (BH1, BH3, BH4, BH5, and BH6) were drilled at the Georgetown site. Standard Penetration Tests (SPT) and Texas Cone Penetration (TCP) tests were performed. A detailed report of the drill tests was submitted to TxDOT. Here, we excerpt the primary findings of the drilling report, in order to compare their findings with the geophysical tests conducted at the site. We note that the drilling occurred approximately 18 months after the geophysical surveys and changes (e.g. enlargement or filling of voids) may have occurred in the intervening period. Figure 4.33 shows the location of the boreholes relative to the ERT survey lines. In particular:

- BH1 is close to, but not on, ERT line A
- BH3 and BH6 are on ERT line A
- BH5 is on ERT lines B and X
- BH4 is between ERT lines B and C

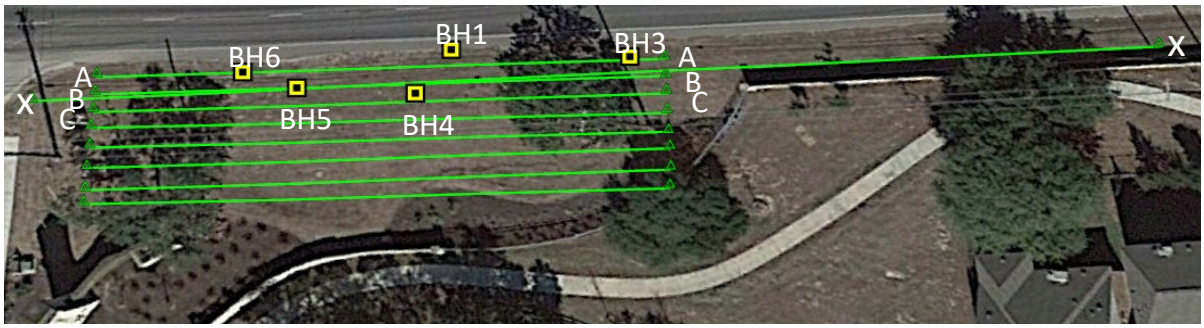

Figure 4.33: Location of boreholes relative to ERT survey lines.

Figure 4.34 depicts the subsurface resistivity map on a slice along ERT line A; it also shows the drilling logs for BH3, BH1 and BH6, all of which are close or on ERT line A. As it can be seen, the drill log at BH3 revealed a small void of approximately 1.5 ft (or 0.46 m) (vertical size), at a depth of approximately 24.5 ft (or 7.5 m). In contrast, the ERT survey at the same depth and location, though it did reveal material of high resistivity, the inverted resistivity value was not high enough for the location to be characterized as a void. At BH1, the drill log describes a fairly sizeable void of about 7 ft (or 2.1 m) (the last 1 ft is clay-filled), whereas the ERT survey revealed a void at the same location but at a somewhat different depth, with size almost double the drilling

log size, at 13.5 ft (or 4.1 m). Lastly, at BH6 neither the drilling, nor the ERT survey revealed any voids.

Figure 4.35 shows the resistivity map on a slice along ERT line B, together with the drill logs of boreholes BH5 and BH4. We note that the drilling revealed a sizeable void at BH5, approximately, 10 ft (or 3 m), starting at a depth of about 22 ft (or 6.7 m), which was not detected by the ERT survey. At BH4, both the drilling and the ERT survey revealed a void, albeit starting at a different depth and of different size (the size was 6 ft per the drilling log, and about 13 ft per the ERT survey).

Figure 4.36 shows the resistivity map on a slice along ERT line C, together with the drill logs of boreholes BH4 (recall BH4 is between ERT lines B and C). Both the drilling and the ERT survey revealed a void, albeit starting at a different depth and of different size (the size was 6 ft per the drilling log, and about 14 ft per the ERT survey).

Of interest is also the subsurface resistivity map associated with ERT line X (line X is 110 m-long, thence the deeper profiling): in effect line X surveys the same slice, albeit longer and deeper, as the slice surveyed by line A. Boreholes BH4 and BH5 are on line X, and similarly to the findings associated with ERT line A, here too the ERT survey did not reveal the void found by drilling at BH5 (Figure 4.37). Moreover, at BH4, the ERT survey revealed a void at slightly different depth than the one revealed by the ERT survey of line A.

In summary, at the 5 borings there were 4 voids found, of which 3 were also found by the ERT survey, albeit of different extent and starting depth.

Lastly, we mapped the resistivity values along the length of each of the 5 boreholes to materials and attempted to correlate the materials to the ones return by the drilling (and subsequent laboratory testing). As it can be seen in Figure 4.38, a comparison suggests that very close to the surface (3-4 ft) the ERT survey and the drilling seem to agree in most cases. But, beyond the near-surface layer, there are differences, which add to the differences related to the location and size of identified voids. In summary though, the ERT survey did successfully identify voids at the same horizontal locations as the drilling revealed. We believe that it is not prudent to use this comparison to draw conclusions; there are, at least two reasons: we believe that the ERT inversion software merits improvement in a few areas that could result in improved resolution; and, secondly, the time

difference between the ERT survey and the drilling could account for some, but not all, of the observed differences (e.g. the undetected void in BH5).

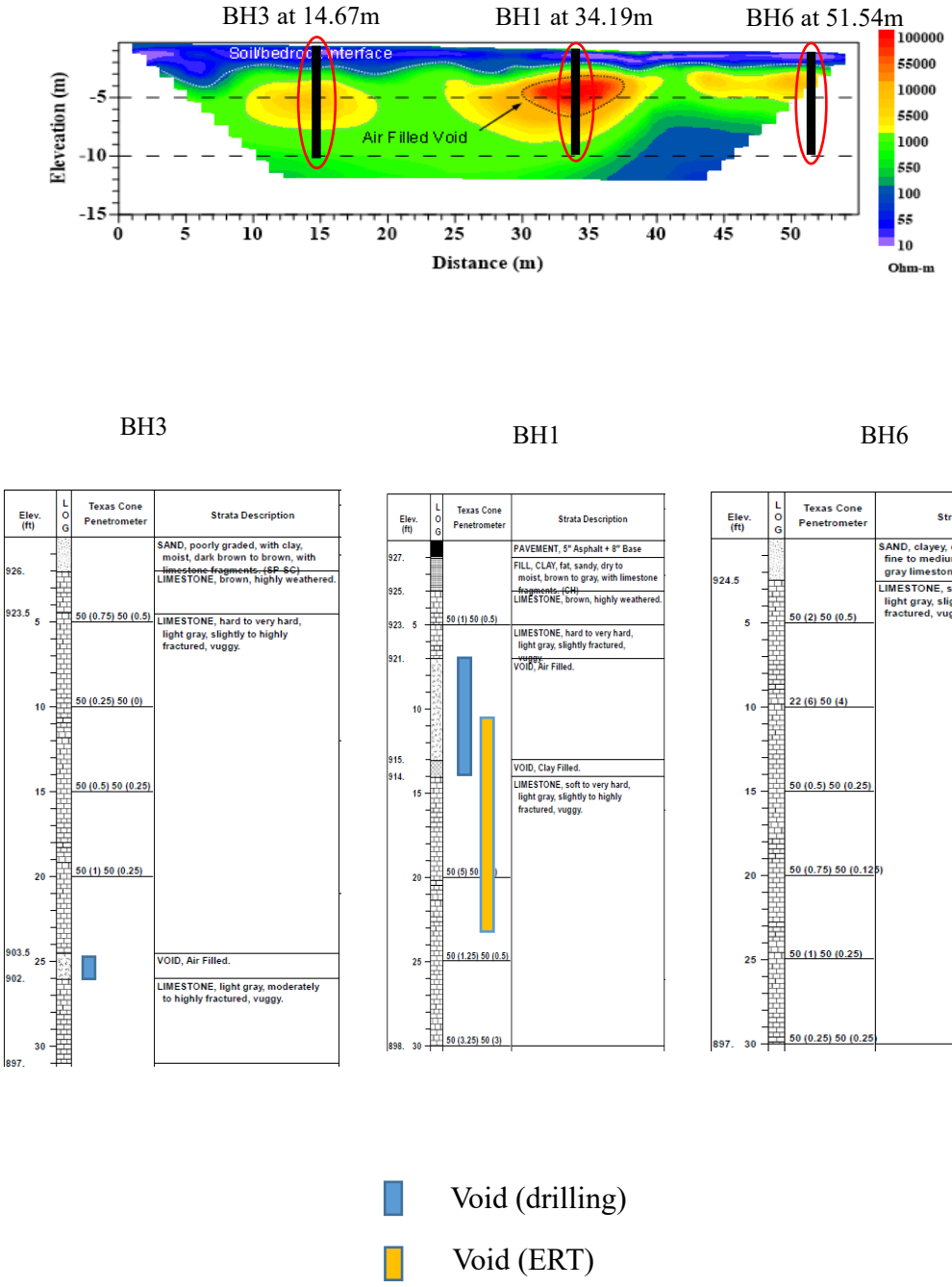

Figure 4.34: ERT line A: borehole drill logs; ERT survey with borehole locations; voids found through drilling are shown with a blue column in the drill log and are contrasted with the ERT voids shown in orange.

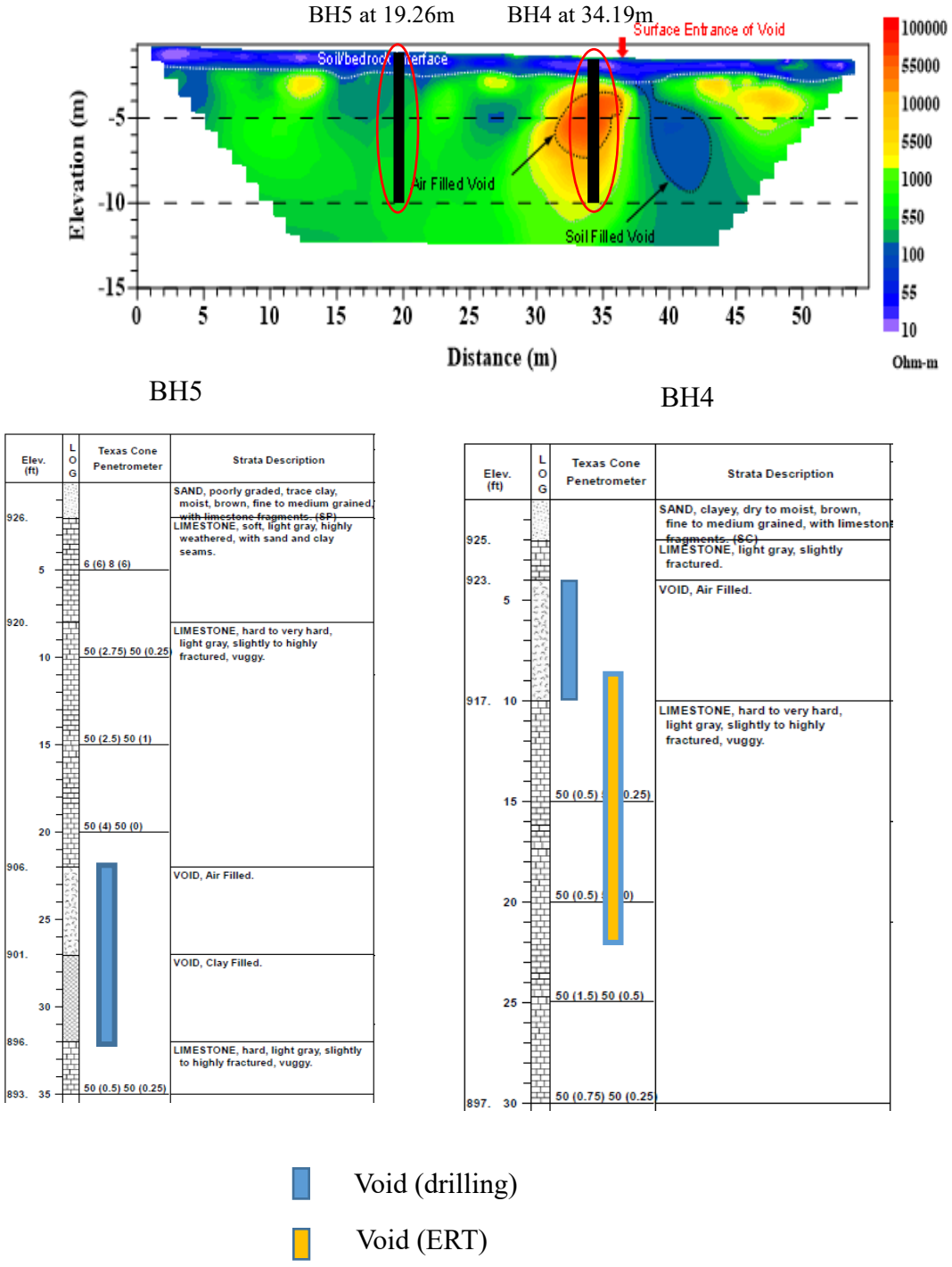

Figure 4.35: ERT line B: borehole drill logs; ERT survey with borehole locations; voids found through drilling are shown with a blue column in the drill log and are contrasted with the ERT voids shown in orange.

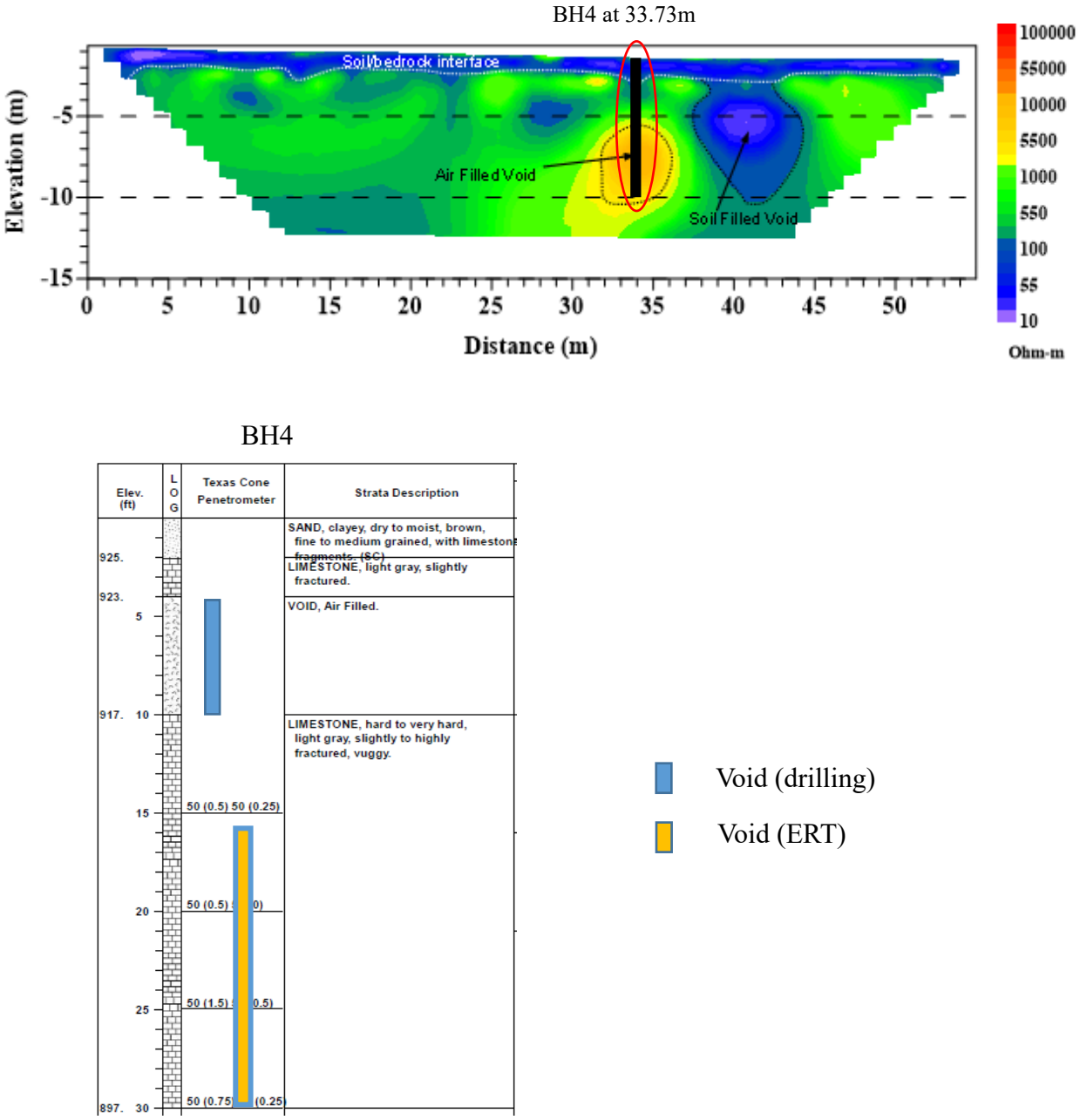

Figure 4.36: ERT line C: borehole drill logs; ERT survey with borehole locations; voids found through drilling are shown with a blue column in the drill log and are contrasted with the ERT voids shown in orange.

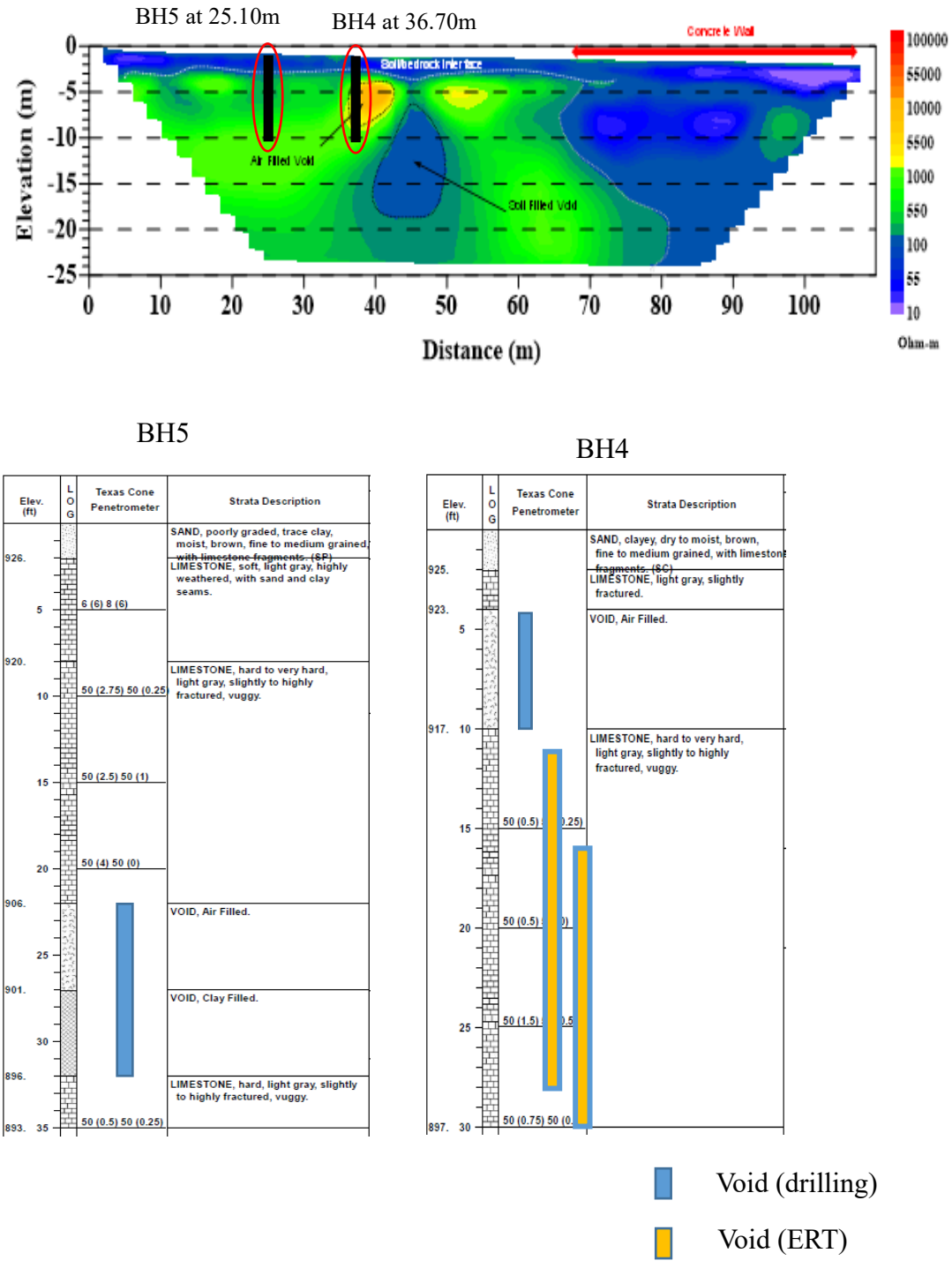

Figure 4.37: ERT line X: borehole drill logs; ERT survey with borehole locations; voids found through drilling are shown with a blue column in the drill log and are contrasted with the ERT voids shown in orange.

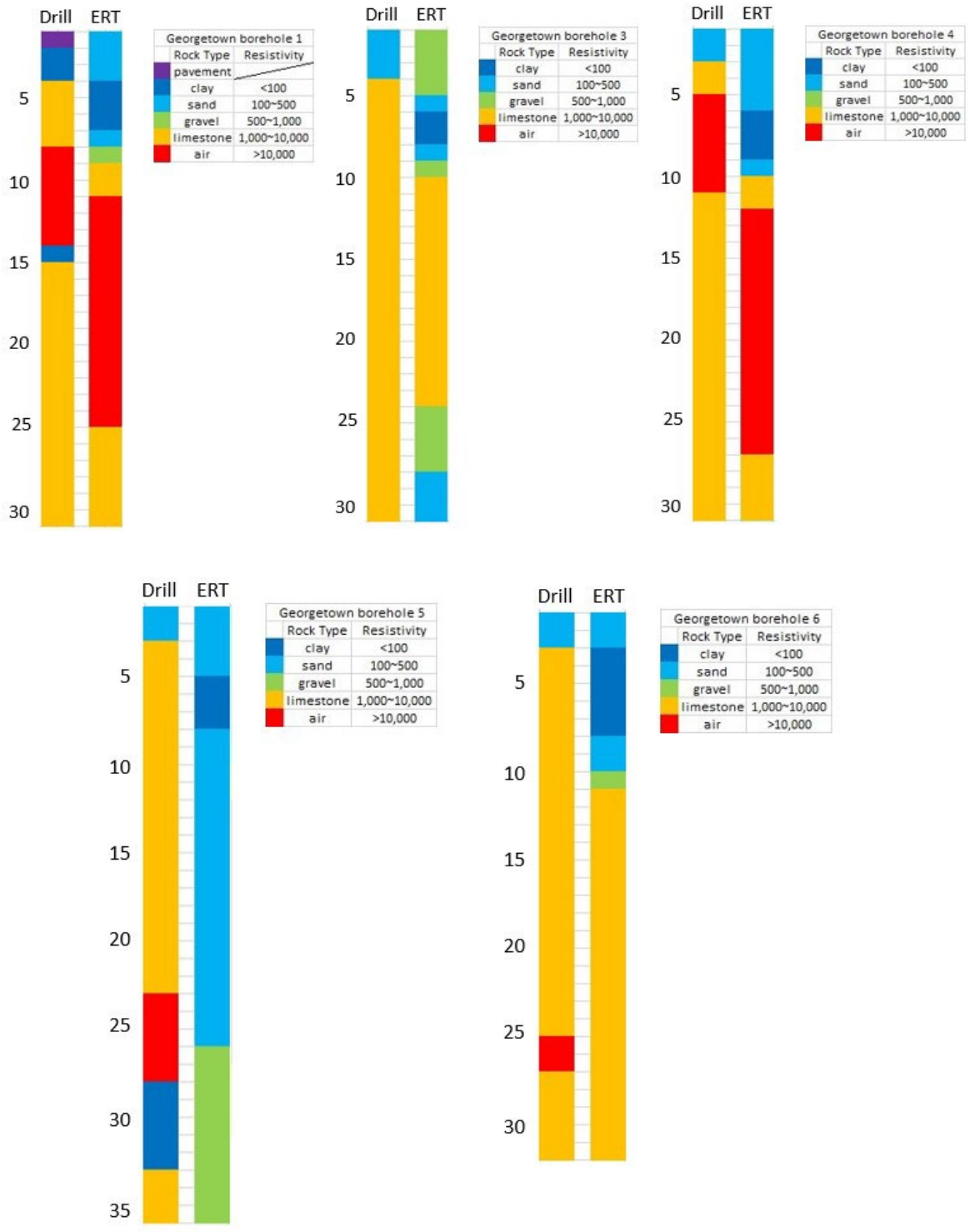

Figure 4.38: Characterization of materials using laboratory tests on cores removed from the boreholes (left column) versus ERT-based characterization.

4.2. Field Experiments at Southwest Parkway (SWPW)

At the Southwest Parkway site we deployed ERT, MASW and FWI arrays. TxDOT conducted the GPR surveys, and an independent contractor at TxDOT's direction performed the verification drilling.

4.2.1. ERT – Field Studies (SWPW)

4.2.1.1. Testing Method and Locations

Geophysical testing to investigate potential voids at the Southwest Parkway Site, TX (see Figure 4.39) was conducted using the Electrical Resistivity Tomography (ERT) method. The survey lines were located within a storm water drainage pond as shown in Figure 4.39. A surface opening (void opening) was located at the west side of the Southwest Parkway site as shown in Figure 4.40. As part of the pond's original construction, underground utilities consisting of PVC drainage pipes were buried parallel to the survey lines. PVC drainage pipes were buried under and bedded with a layer of sand and gravel. The pipes were underlined by a clay layer. A general cross section of the drainage pond is provided in Figure 4.41. Due to the interbedded layers of sand/gravel/clay and pipes, this system is expected to significantly interfere with the measured resistivity values and may lead to anomalies in the subsurface and errors in the overall results.

For the ERT surveys, eleven survey lines were conducted for the study as shown in Figure 4.39. All Lines (named A to K) are approximately South-North (zero distance on the South end of the line) with a length of 55 meters and were conducted as parallel lines with a spacing between lines of approximately 2.0 meters (see Figure 4.42-Figure 4.43). A ground photo of Line A is shown in Figure 4.44.

The ERT data were collected using an Advanced Geosciences Inc. (AGI) SuperSting R8/IP Wifi resistivity meter (Figure 4.7). For each survey, 56 surface electrodes were used with a distance between electrodes of 1.0 m. Passive electrode cables were connected to stainless steel stakes inserted 15-30 centimeters into the soil surface. The SuperSting resistivity meter controlled the injection of currents and the measurement of potentials using multiple channels. Contact resistance tests were performed before each survey and were generally less than 5000 ohm-m with some values above 6000 ohm-m indicating relatively high contact resistance at the site. Two-

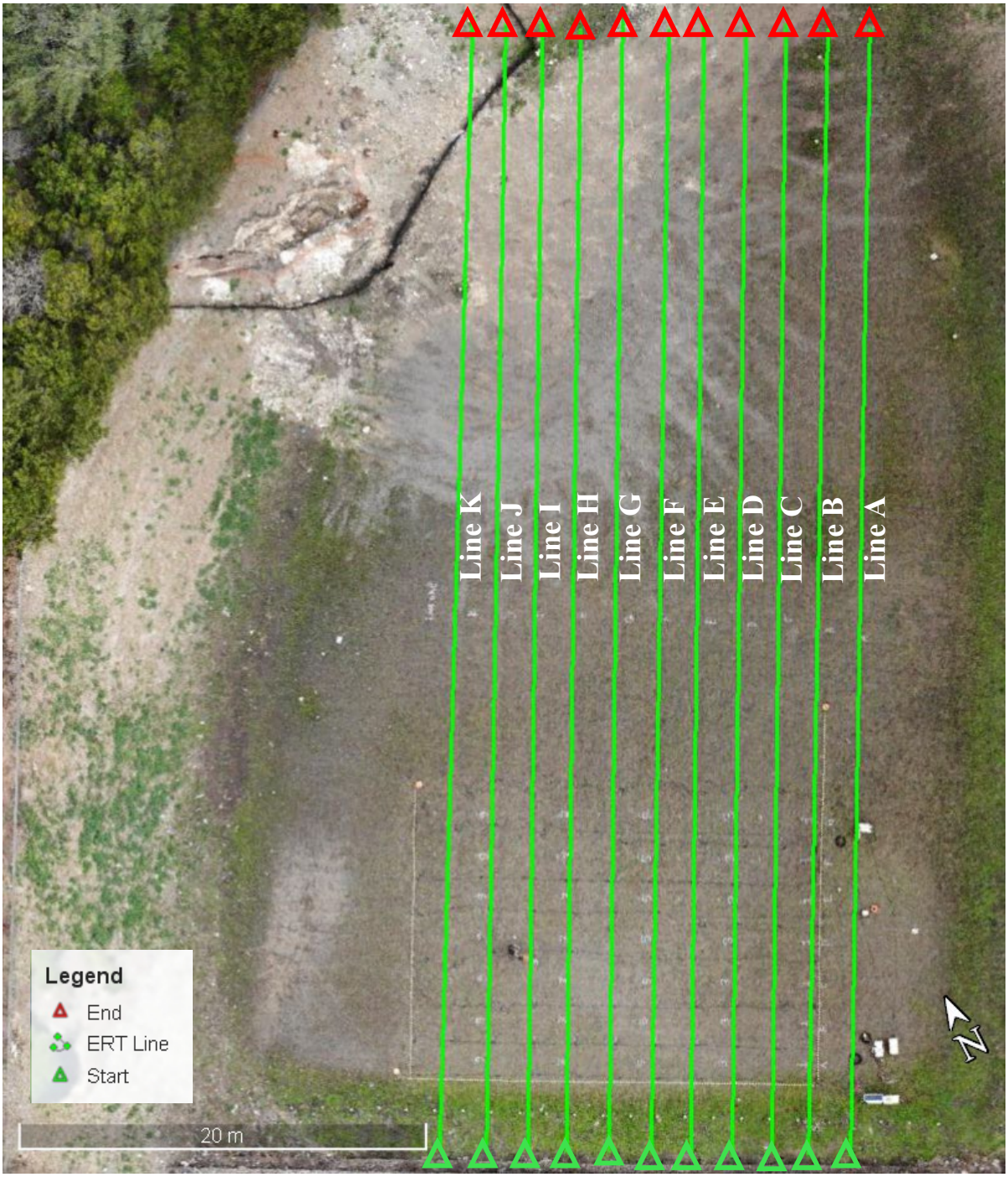

Figure 4.39: Site map of ERT testing showing the location of each ERT line.

dimensional dipole–dipole and strong gradient survey configurations were used to collect data for each survey. The relative location of each electrode was surveyed using a Nikon Total Station with

the true location of the end of each line surveyed using a Trimble Geo7x Centimeter GPS unit. More information regarding testing methods can be found in Rahimi et al. 2021 and 2018.

Figure 4.40: Surface opening in the west side of the Southwest Parkway site.

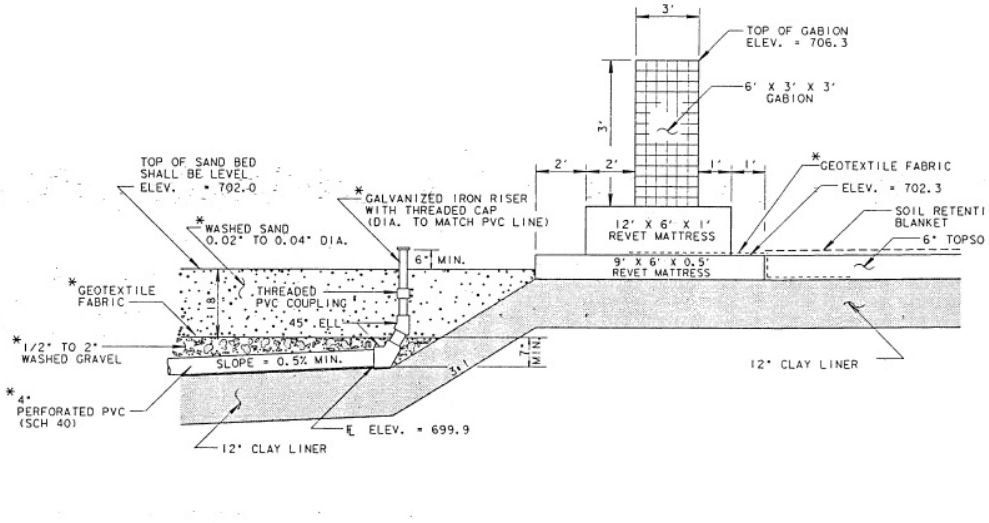

Figure 4.41: Cross section of drainage system at the Southwest Parkway site

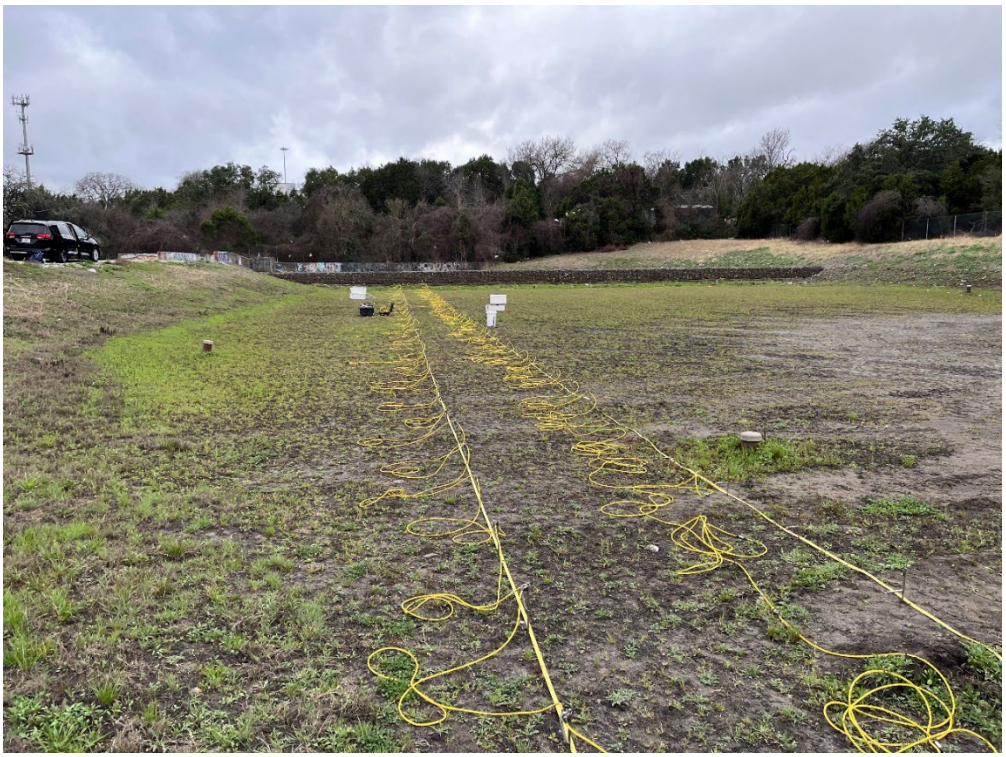

Figure 4.42: Picture of ERT equipment used for each Line.

Figure 4.43: Drone view of deployed ERT lines A-D.

Figure 4.44: Testing on ERT line A, while ERT line B is in preparation.

4.2.1.2. Data Processing

2D Data Processing

The raw ERT data sets were inverted using AGI's EarthImager2D software. This program inverts measured resistivity data into a modeled distribution of true inverted resistivity values through iterative resistivity inversion algorithms. The resulting resistivity profile represents the resistivity distribution that best fits the measured data. However, resistivity inversion is indeterminate and non-unique, where many resistivity distributions could match the measured data equally well. Standard surface processing parameters suggested from AGI were used with a smooth inversion model used for all resistivity inversions, a horizontal-to-vertical roughness factor of 0.5, a smoothness factor of 10, and a damping factor of 10. The minimum resistivity was set at 1 ohm-m and the maximum resistivity was set at 100,000 ohm-m. Electrode elevations from the total station were included in the inversions. After a preliminary inversion of each ERT profile, relative data misfit was used to remove individual points with >20-50% data misfit, based on the

assumption that resistivity for adjacent measurements should not vary greatly. Up to 20% of measured data were removed following this criterion. The misfits between measured and modeled resistivity data for each profile, as measured by the root mean square (RMS) error, were minimized in the inversions. Inversions were considered complete after eight iterations or when an RMS < 5-10% was reached, with the models converging in less than five iterations. The inversion procedure used a finite-element forward model with a Cholesky decomposition solver, six mesh divisions, and a thickness and depth factor of 1.1.

Pseudo 3D Data Processing

For the Pseudo 3D processing, the 2D raw resistivity for Lines A-K were combined in AGI's EarthImager3D software. This program was used to invert the combined resistivity data from the 2D lines. The resulting 3D resistivity model represents the resistivity distribution that best fits the measured data. However, as with 2D, 3D resistivity inversion is indeterminate and non-unique, where many resistivity distributions could match the measured data equally well. Standard surface processing parameters suggested from AGI were used with the parameters as used for the 2D data processing. Electrode elevations from the total station were included in the inversions. After a preliminary inversion, relative data misfit was used to remove individual points with >20-50% data misfit, based on the assumption that resistivity for adjacent measurements should not vary greatly. Up to 20% of measured data were removed following this criterion. The misfits between measured and modeled resistivity data for each profile, as measured by the root mean square (RMS) error, were minimized in the inversions. Inversions were considered complete after eight iterations or when an RMS < 5-10% was reached, with the models converging in less than five iterations. The inversion procedure used a finite-element forward model, two mesh divisions, and a thickness and depth factor of 1.1.

4.2.1.3. Interpretation and Results

The results of the ERT measurements for each survey line and the 3D model results are provided in this section. Please refer to Figure 4.39 for the location and orientation of each line. The elevation of each 2D cross section or model is based on the relative elevation of the site with zero elevation set as the highest measured elevation on the site.

Survey Line A

Shown in Figure 4.45 is the 2D resistivity cross section for Line A. For this cross section, a moderately resistive near surface layer (yellow and orange) is observed for the top ~1-2 meters of the subsurface, which is underlain by a low resistivity area (blue and pink) for 4-6 meters and finally another moderately resistive area (yellow and orange) from 6-11 meters deep. The shallow higher resistivity section likely indicates the sand and gravel layers which are part of the filtration pond system as shown in Figure 4.41. Also, PVC drainage pipes can be a reason for the high resistivity observed. The underlying low resistivity area is likely related to the clay layer which was under the PVC piping. Finally, the deepest layer can be an indication of bedrock. While this layering generally matches the known construction layering under the pond, the depths and thickness do not match the known depths and thickness of the site exactly. This is likely caused by the non-unique nature of the inversion process where layer thicknesses and properties are smeared across layer boundaries and highlights the issues with testing over man-made structures.

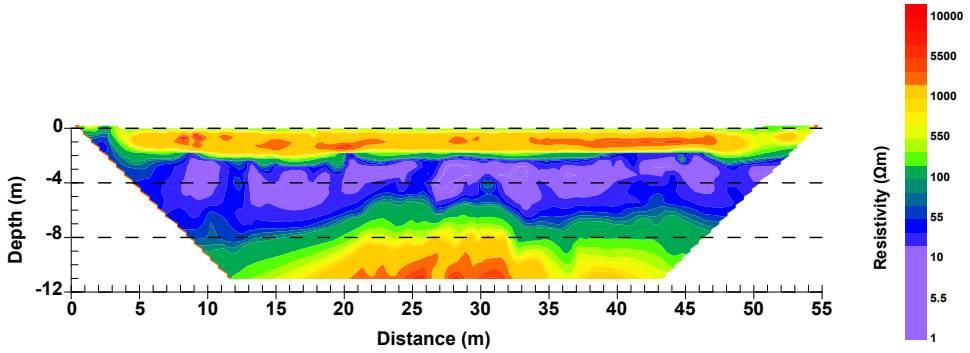

Figure 4.45: 2D cross-section of the subsurface resistivity below Line A.

Survey Line B

Shown in Figure 4.46 is the 2D resistivity cross section for Line B. For this cross section, a moderately resistive near surface area (yellow and orange) is observed for the top ~1-2 meters of the subsurface, which is underlain by a less resistive area (blue and pink) and finally with another moderately resistive (yellow and red) area. The first moderately resistive area is due to the sand and gravel layers and drainage pipes. A more resistive area is observed at 23-32 meters along the line with a depth from 4-12 meters below the surface. This area could be a rock pinnacle or a thin developing void below the surface.

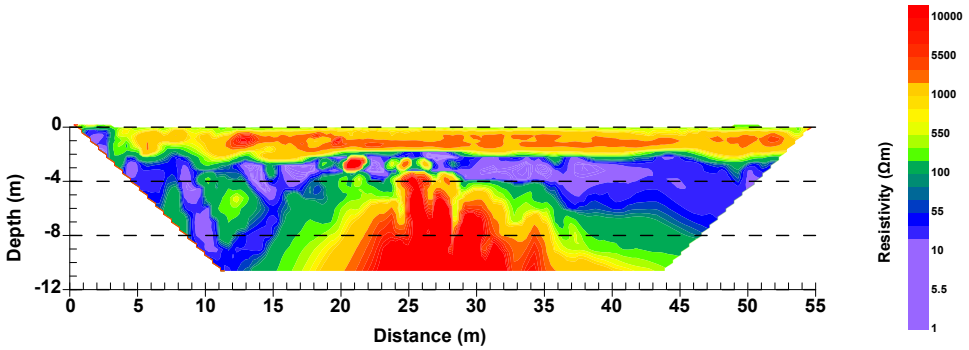

Figure 4.46: 2D cross-section of the subsurface resistivity below Line B.

Survey Line C

Shown in Figure 4.47 is the 2D resistivity cross section for Line C. Like Line A and B, a moderately resistive near surface area (yellow and orange) is observed for the top ~1-2 meter of the subsurface, which is underlain by a less resistive area (blue and pink) and another moderately resistive area (yellow and orange). The first moderately resistive area is due to the sand and gravel layers. Also, the drainage pipes can be another reason for the higher resistive area. The middle low resistivity area is probably due to clay layer with higher water content.

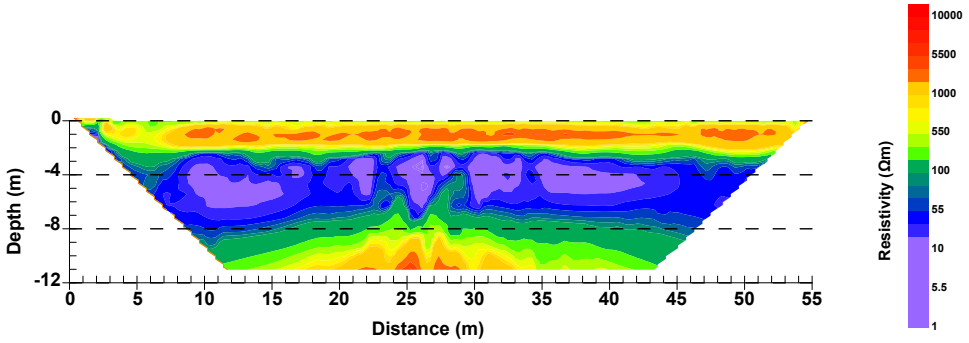

Figure 4.47: 2D cross-section of the subsurface resistivity below Line C.

Survey Line D

Shown in Figure 4.48 is the 2D resistivity cross section for Line D. Like Line A- C, a moderately resistive near surface area (yellow and orange) is observed for the top ~1-2 meter of the subsurface, which is underlain by a less resistivity area (blue and pink) and another moderately resistive area

at depth. Sand and gravel layers, clay layer and bedrock are probably the reason of these three layers, respectively.

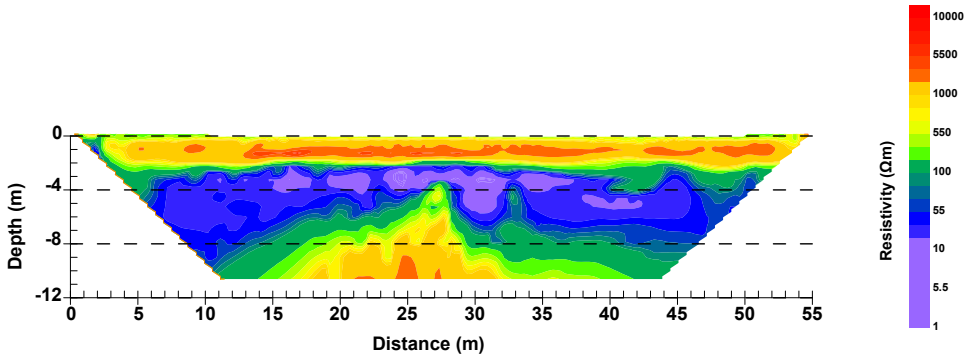

Figure 4.48: 2D cross-section of the subsurface resistivity below Line D.

Survey Line E

Shown in Figure 4.49 is the 2D resistivity cross section for Line E. Like previous lines, a moderately resistive near surface area (yellow and orange) is observed for the top ~1-2 meter of the subsurface, which is underlain by a less resistivity area (green and blue). In this section it seems the depth of the bedrock is deeper than the previous lines as only a small part of the deeper moderately resistive area is observed under the clay layers.

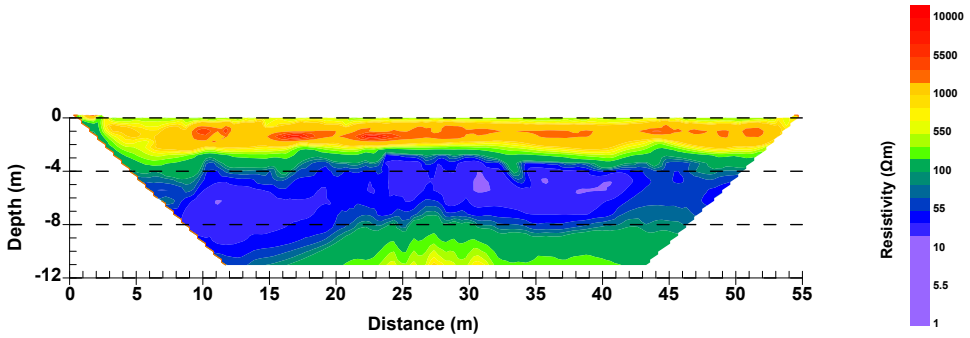

Figure 4.49: 2D cross-section of the subsurface resistivity below Line E.

Survey Line F

Shown in Figure 4.50 is the 2D resistivity cross section for Line F. Like Line A-E, a moderately resistive near surface area (yellow and orange) is observed for the top ~1-2 meter of the subsurface,

which is underlain by a less resistive area (green and blue). The thickness of the low resistive clay layer is larger for this line (about 8 meters) than lines A-D.

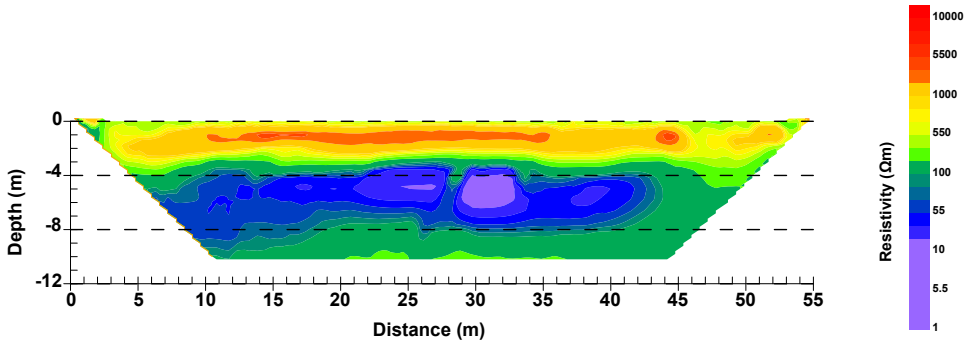

Figure 4.50: 2D cross-section of the subsurface resistivity below Line F.

Survey Line G

Shown in Figure 4.51 is the 2D resistivity cross section for Line G. Like Line A-F, a moderately resistive near surface area (yellow and orange) is observed for the top ~1-2 meter of the subsurface, which is underlain by a less resistive area (green and blue).

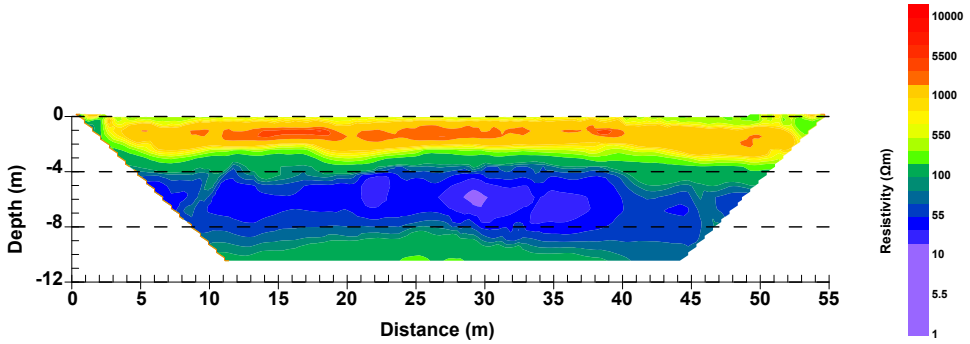

Figure 4.51: 2D cross-section of the subsurface resistivity below Line G.

Survey Line H

Shown in Figure 4.52 is the 2D resistivity cross section for Line H. Like Line F-G, a moderately resistive near surface area (yellow and orange) is observed for the top ~1-3 meter of the subsurface, which is underlain by a less resistive area (green and blue).

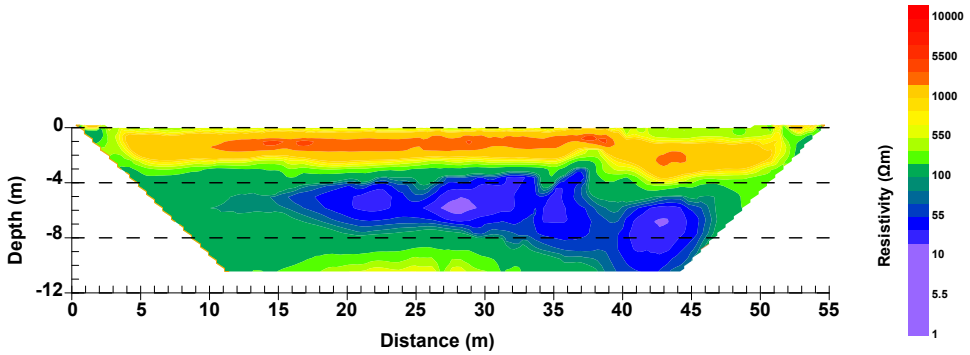

Figure 4.52: 2D cross-section of the subsurface resistivity below Line H.

Survey Line I

Shown in Figure 4.53 is the 2D resistivity cross section for Line I. A moderately resistive near surface area (yellow and orange) is observed for the top ~1-3 meter of the subsurface which is deeper after 32 meter along the line. Also, this layer is underlain by a less resistive area (green and blue). A moderately resistive area (yellow and red) is also observed along the line at 25 meters which may indicate stiffer rock in the subsurface.

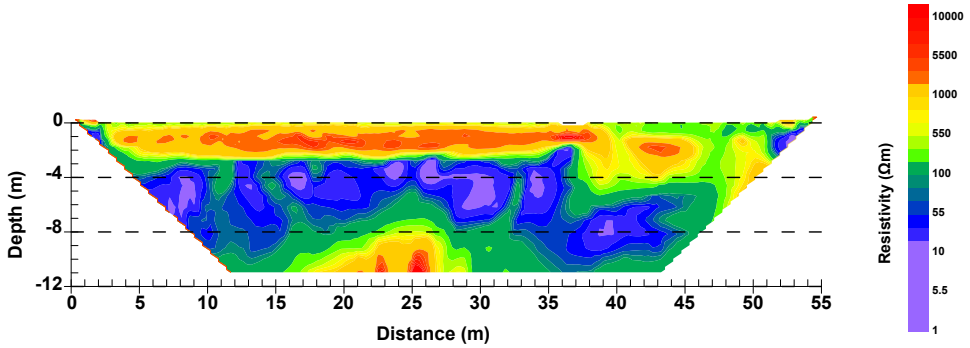

Figure 4.53: 2D cross-section of the subsurface resistivity below Line I.

Survey Line J

Shown in Figure 4.54 is the 2D resistivity cross section for Line J. Like Line A-I, a moderately resistive near surface area (yellow and orange) is observed for the top ~1-3 meter of the subsurface, which is underlain by a less resistive area (green and blue). The thickness of the low resistive area is more at the end of line and stretches to the soil surface.

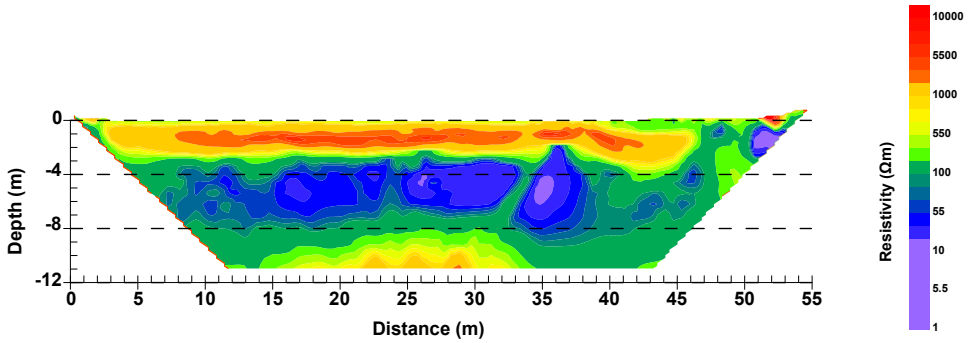

Figure 4.54: 2D cross-section of the subsurface resistivity below Line J.

Survey Line K

Shown in Figure 4.55 is the 2D resistivity cross section for Line K. Like Line J, a moderately resistive near surface area (yellow and orange) is observed for the top ~1-3 meter of the subsurface, which is underlain by a less resistive area (green and blue). The high resistivity area is replaced by the low resistivity area after 43 meters along the line, probably an indication of more saturated zone or higher clay content.

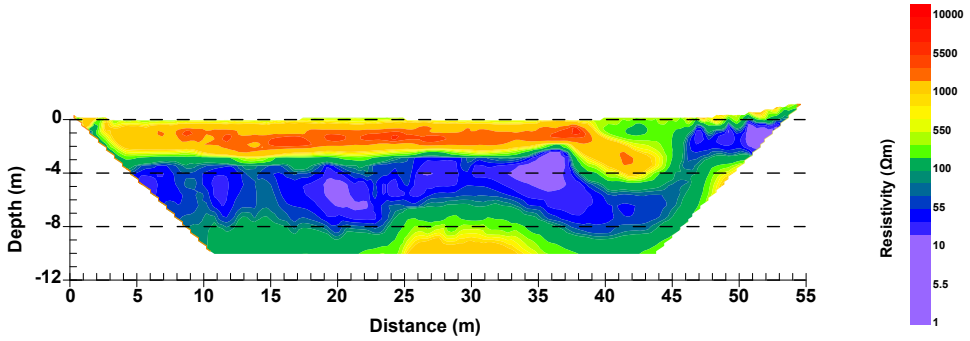

Figure 4.55: 2D cross-section of the subsurface resistivity below Line K.

Combined 2D Results

Three different layers were observed in the ERT cross sections. A near surface moderately resistive layer for the first 1-3 meter from soil surface, mostly related to the sand and gravel layers which also included the PVC drainage pipes. After this, there is a subsequent low resistivity layer 2 – 12 meters from soil surface, which could be an indication of natural high clay content soil. Finally, there is another moderately resistive area with a depth generally between 6 and 12 meters from

soil surface, which could be the bedrock layer. It seems the bedrock depth is shallower in the first lines (east side of the site) and become deeper moving toward west of the site. The only different pattern is the higher resistive zone observed in Line B but considering the shape and size of the area it seems that it could be a rock pinnacle not an air-filled void.

Pseudo 3D Results

Shown in Figure 4.56 is the pseudo 3D resistivity model for the site with the resistivity higher than 10,000 Ohm-m. These high resistivity areas are very close to the surface, showing a depth less than 2 m. These areas are singularly scattered into the site with a relatively high distance between them. Due to these reasons, it seems they cannot be air filled void, instead their locations closely match the drainage pipes at the site. Therefore, these spots considered to be drainage pipes or their projections.

Shown in Figure 4.57 is the pseudo 3D resistivity model for the site with moderate resistivity highlighted in the plot (resistivity between 5,000 Ohm-m and 10,000 Ohm-m). Depth of these high resistive areas are less than 2 meters. Due to the shallow depth of these spots and as the pseudo resistivity is not considered high enough to be an air-filled void, it is presumed these areas are related to the surface drainage system of the pond.

Shown in Figure 4.58 is the pseudo 3D resistivity model for the site with moderate resistivity (resistivity between 500 Ohm-m and 5,000 Ohm-m). The location of these moderate resistivity areas matches well with the moderate resistive areas in the previous 2D cross sections and likely represent the near surface sand and gravel layers used for covering the drainage system. Depth of this layer is less than 3 meters in all areas, which is relatively in accordance with depth of the drainage system shown in Figure 4.41. However, there is an error in the resolved depth of the drainage system likely due to the non-unique nature of the inversion process.

Finally, shown in Figure 4.59 is the pseudo 3D resistivity model for the site with low resistivity (less than 500 Ωm). This area corresponds with the clayey soil beneath the drainage system.

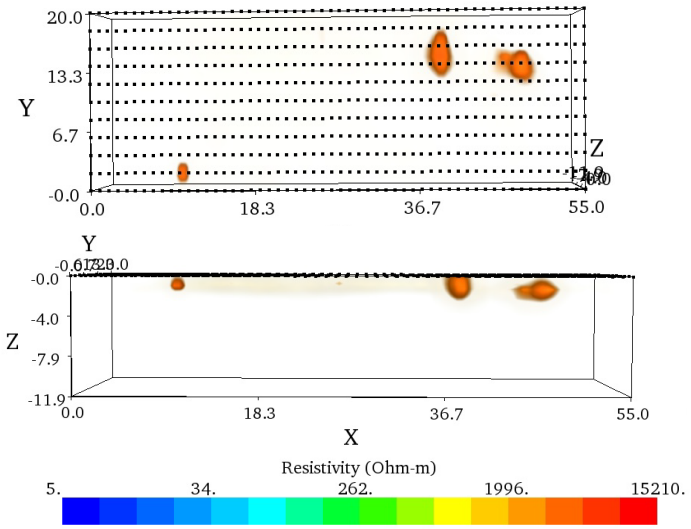

Figure 4.56: Pseudo 3D resistivity model with moderate resistivity (>10,000 Ωm) areas. Top figure is the top view and bottom figure is the profile view looking East.

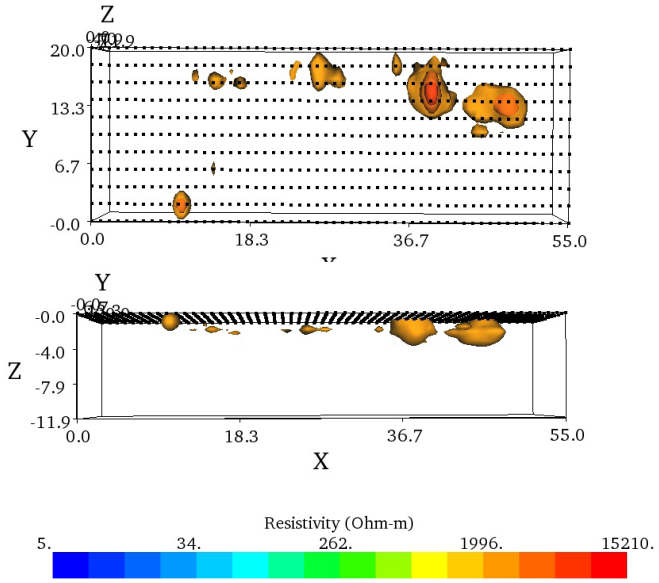

Figure 4.57: Pseudo 3D resistivity model with moderate resistivity (>5,000 Ωm, but no more than 10,000 Ωm) areas. Top figure is the top view and bottom figure is the profile view looking East.

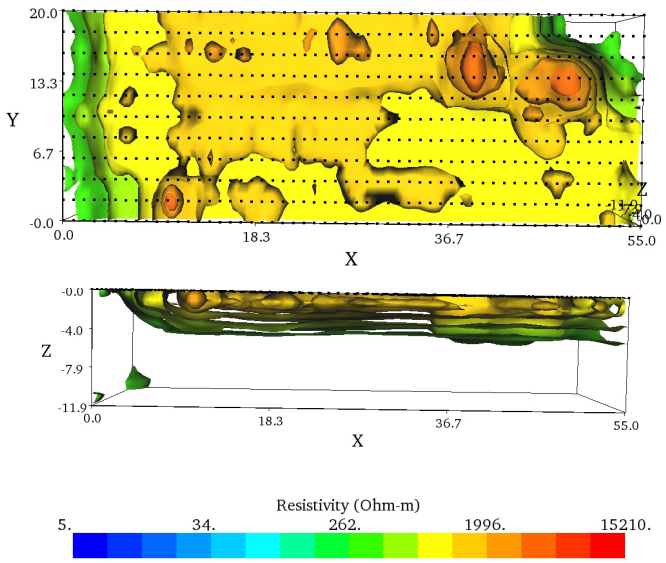

Figure 4.58: Pseudo 3D resistivity model with moderate resistivity (more than 500 Ωm and less than 5,000 Ωm) areas. Top figure is the top view and bottom figure is the profile view looking East.

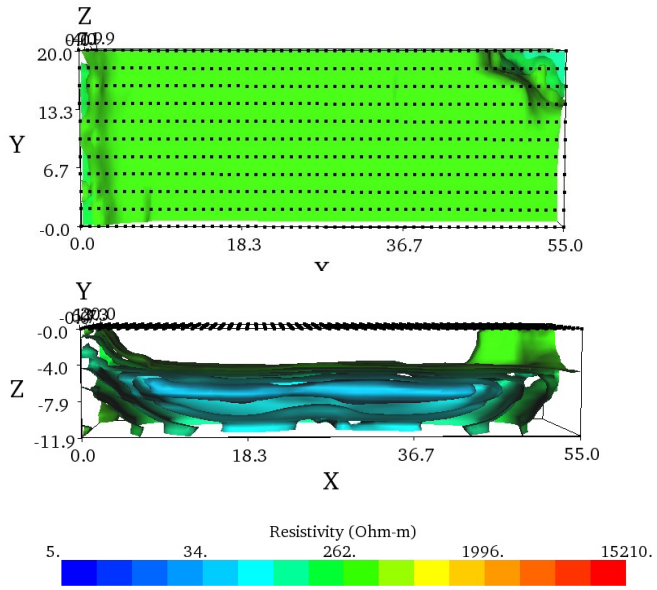

Figure 4.59: Pseudo 3D resistivity model with low resistivity (less than 500 Ωm) areas. Top figure is the top view and bottom figure is the profile view looking East.

4.2.1.4. Summary

Electrical Resistivity Tomography (ERT) was conducted to investigate possible voids at the Southwest Parkway site. A total of 11 lines were conducted on site. ERT result showed that there is a near surface moderately resistive layer at a depth about 1-2 m, followed by a low resistivity layer with a depth of 2-12 m and finally another moderate resistive layer with a depth of 6-12 m. The near surface moderate resistive layer most likely is related to the drainage gravel layer, while the deep moderate resistive layer could be an indication of the bedrock. The intermediate low resistive layer is probably the natural soil deposit composed of clay and sand. Although due to the artificial layering of the site there is difficulty for detecting anomalous zones, no indication of an air-filled void was observed.

4.2.2. MASW and FWI – Field Studies (SWPW)

MASW geophone line arrays were deployed at the Georgetown site, using the same lines as the ERT surveys as shown in Figure 4.60. A total of 11 lines were used for MASW testing (Figure 4.61). The same parameters of testing (sledgehammer source, shot locations, subarray marching, etc) that were followed at the Georgetown site, were followed here as well.

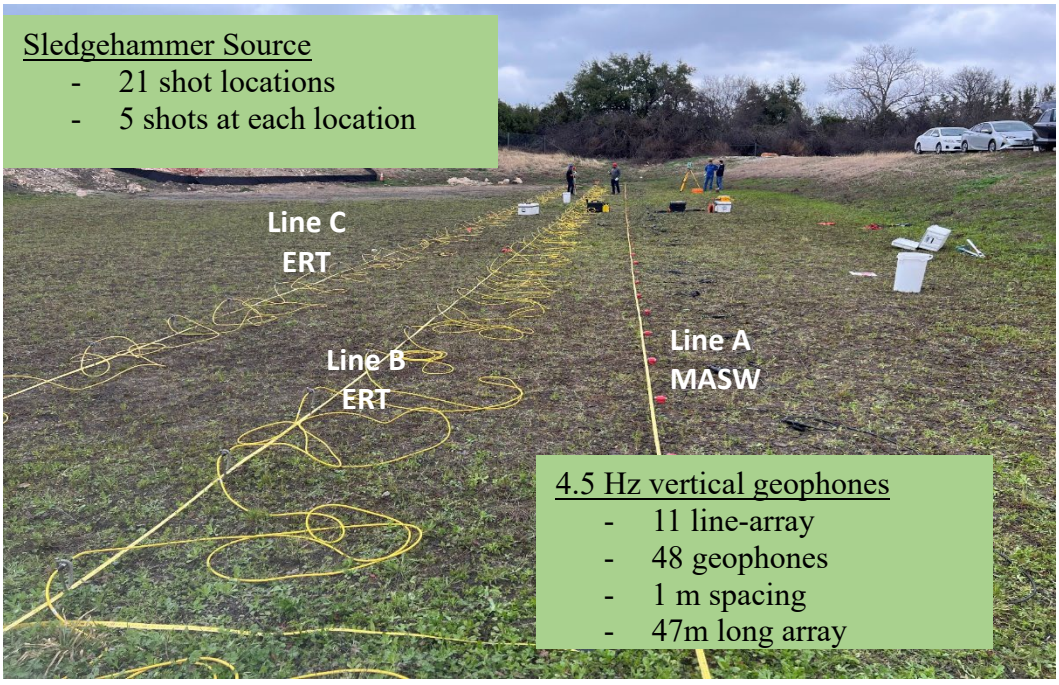

Figure 4.60: ERT and MASW survey lines at the Southwest Parkway field experiment site.

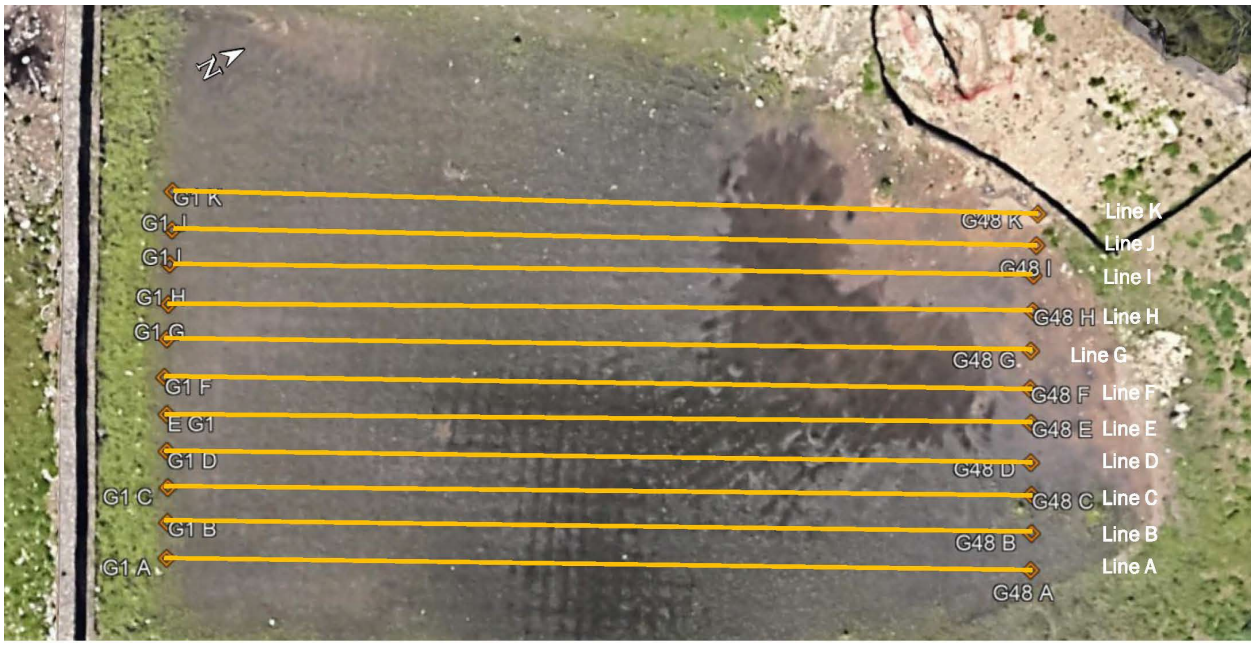

Figure 4.61: Southwest Parkway site map showing MASW array lines (A-K).

Figure 4.62 shows subarray A8, with source offsets at 6.5 m to the left and to the right of the array, while Figure 4.63 depicts the time traces, the SNR, and the experimental dispersion data corresponding to the two source locations for the subarray. As it can be seen, the dispersion data are challenging; to provide an indication of how experimental dispersion curves look like when they lead to successful inversion, Figure 4.64 shows such a case at another site. The dispersion data at the Southwest Parkway site cannot be inverted: we attribute the difficulty to strong lateral property variability at the site, which violates MASW's underlying assumptions.

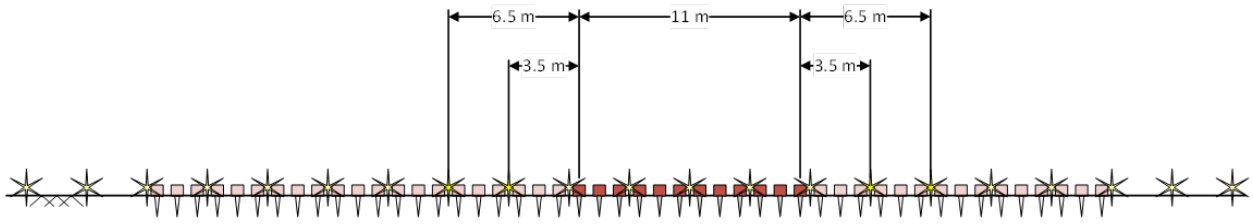

Figure 4.62: Subarray A8.

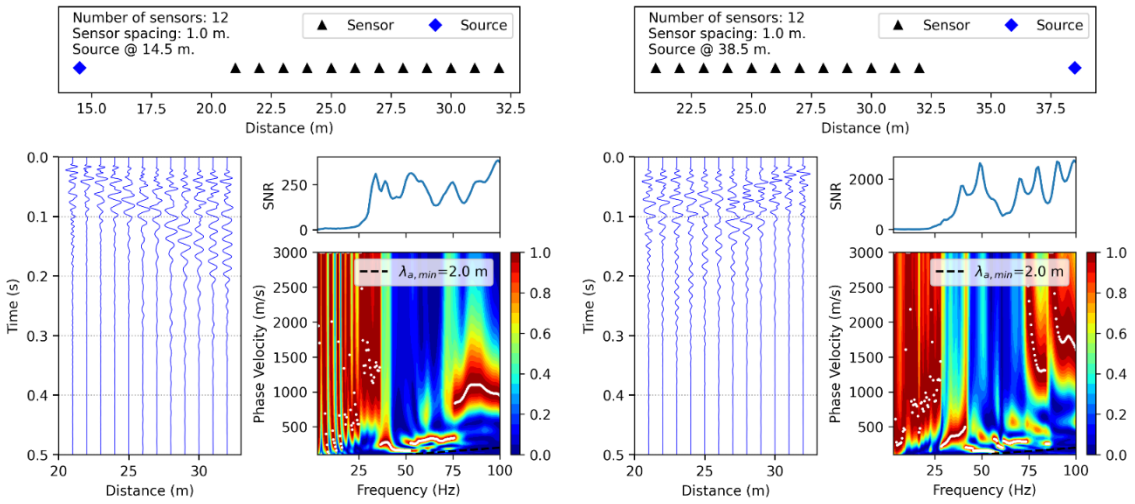

Figure 4.63: Time traces of subarray A8 geophone responses; signal-to-noise ratio; and dispersion data for two offset shot locations.

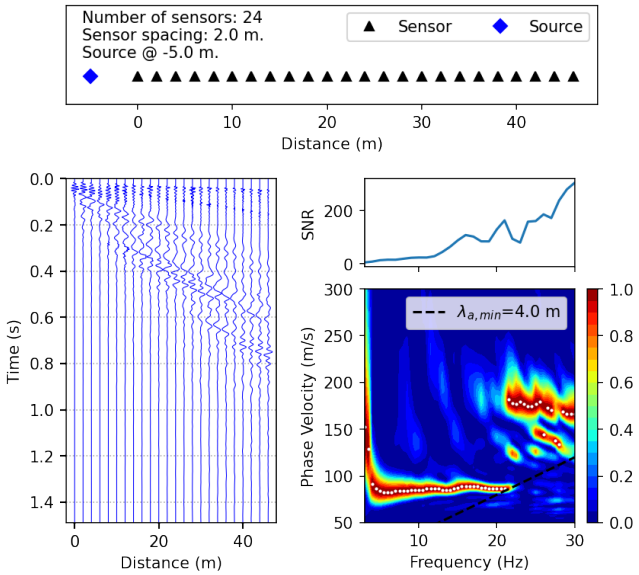

Figure 4.64: An example of invertible dispersion data from another site.

We also deployed an FWI array on a grid of 14 m by 10 m, and deployed a total of 88 geophones (Figure 4.65). As previously stated, the FWI data were not processed due to time limitations.

Figure 4.65: 2D FWI array at the Southwest Parkway field experiment site; geophones are located at the grid vertices.

4.2.3. GPR – Field Studies (SWPW)

The GPR survey at the Southwest Parkway site was conducted by TxDOT on September 8, 2022. There were 27 GPR scan lines reported, canvassing the same area that was surveyed using ERT and MASW. Overall, the GPR radiograms were unremarkable: no voids or strong subsurface anomalies were uncovered. Figure 4.66 depicts a subset of the GPR radiograms along 6 lines spanning the surveyed area.

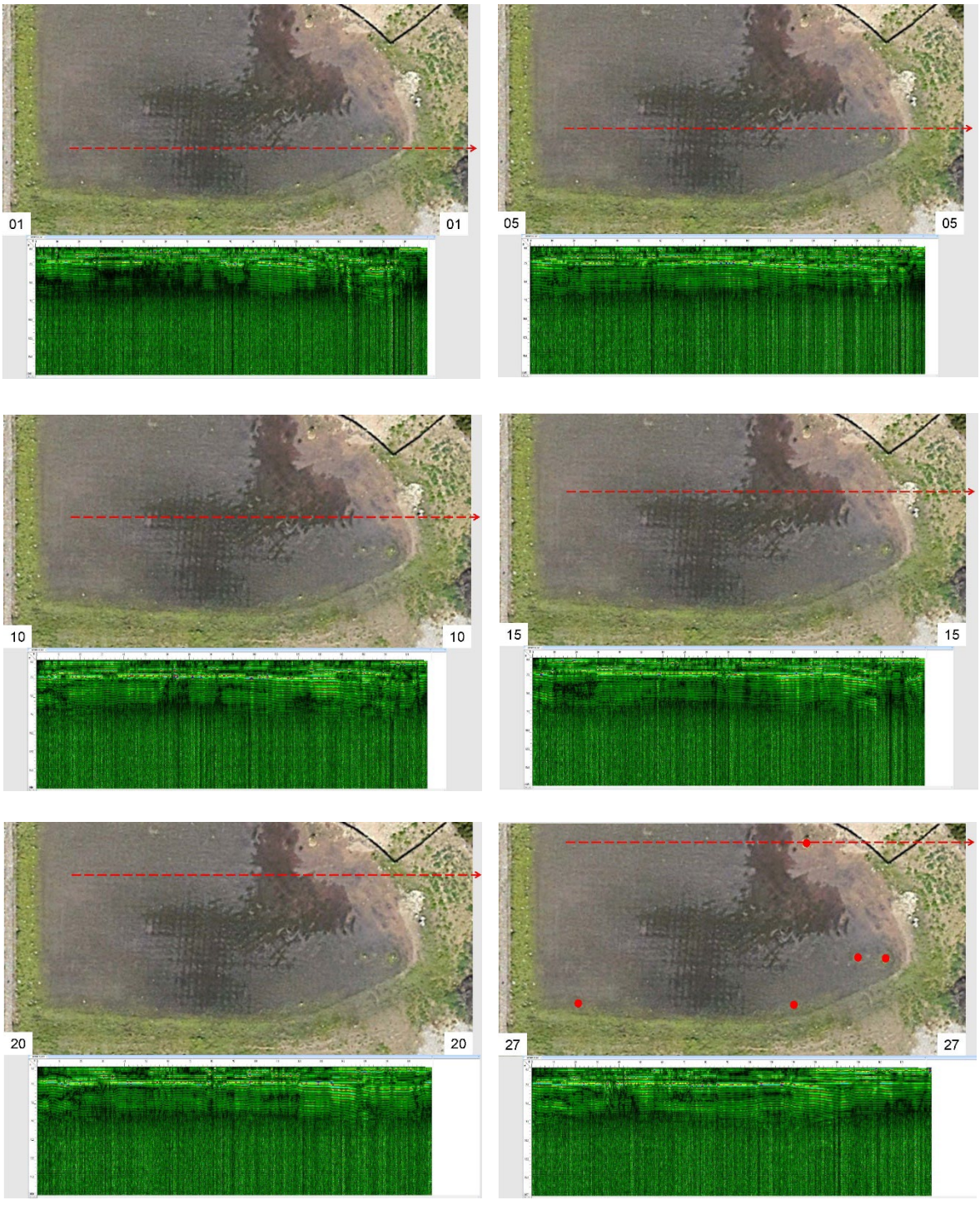

Figure 4.66: GPR radiograms (scans 1, 5, 10, 15, 20, 27) overlapping with ERT lines at the Southwest Parkway site; the scans do not reveal subsurface anomalies or voids.

4.2.4. Verification Drilling (SWPW)

In December 2022, 5 borings (BH1, BH3, BH4, BH5, and BH6) were drilled at the Southwest Parkway site. Of the 5 boreholes, only 2 (BH4 and BH5) were within the portion of the site that was studied using the geophysical methods. Figure 4.67 shows the location of the boreholes relative to the ERT survey lines. Again, the Standard Penetration Tests (SPT) and Texas Cone Penetration (TCP) tests were performed. A detailed report of the drill tests was submitted to TxDOT. Here, we focus on the two boreholes and excerpt the primary findings of the drilling report, in order to compare their findings with the geophysical tests conducted at the site. In particular:

- BH5 is close to, but not on, ERT line F
- BH4 is close to, but not on, ERT line J

Figure 4.68 depicts the subsurface resistivity map on a slice along ERT line F; it also shows the drilling log for BH5. Similarly, Figure 4.69 depicts the subsurface resistivity map on a slice along ERT line J, together with the drilling log for BH4. No voids or other subsurface inclusions were identified either by the drilling or by the ERT survey. Lastly, Figure 4.70 depicts the distribution of materials along the depth of the two boreholes as characterized by laboratory tests (left column) and by mapping the ERT resistivity onto materials (right column). The discrepancy is attributed to the inaccuracies associated with the subsurface resistivities, the mapping between resistivities and materials, and the non-uniqueness of the resistivities (two vastly different materials may share the same resistivity values).

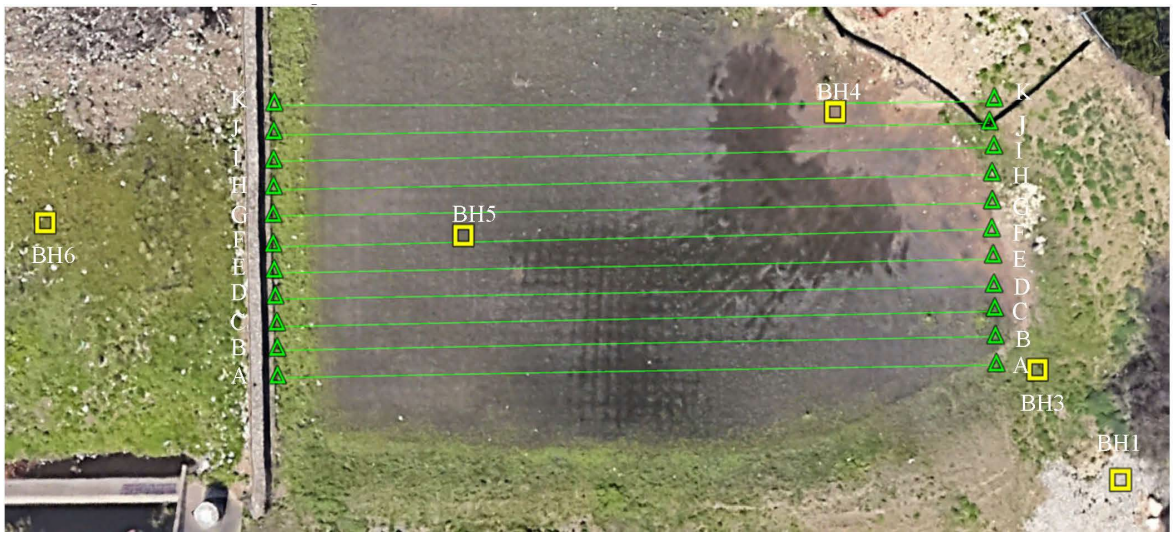

Figure 4.67: Location of boreholes relative to ERT survey lines at the Southwest Parkway site.

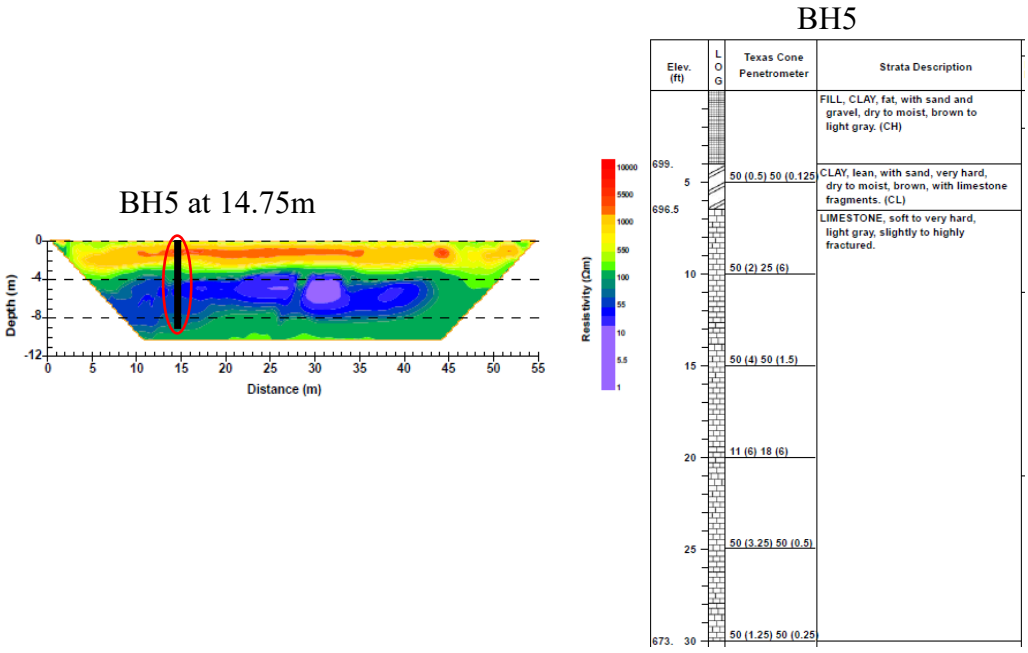

Figure 4.68: ERT line F: borehole drill logs; ERT survey with borehole locations; no were found either by drilling or though the ERT survey.

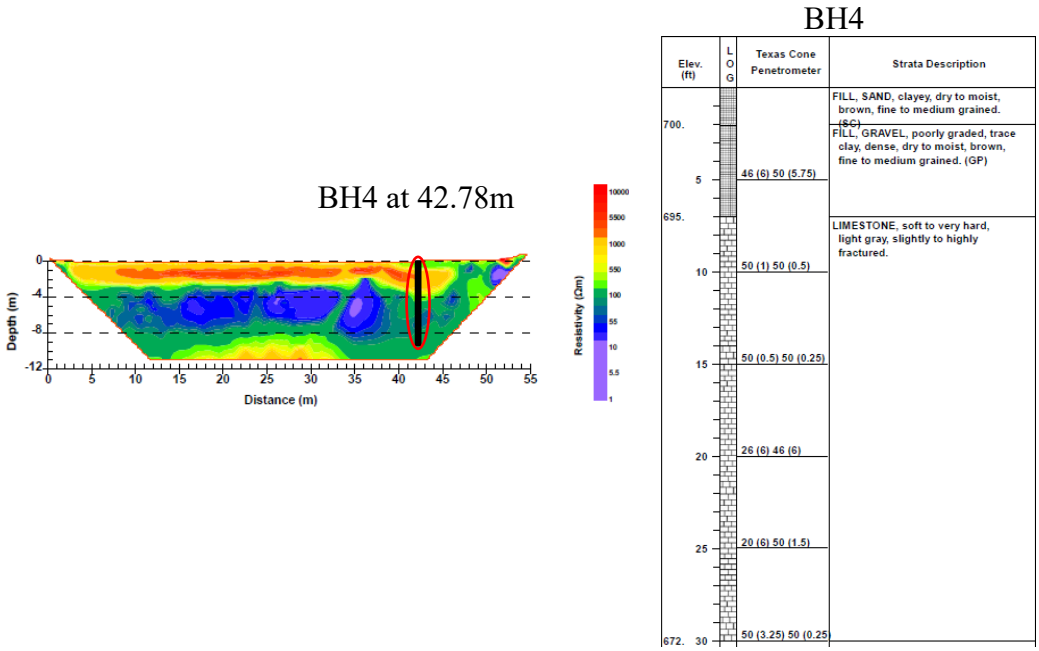

Figure 4.69: ERT line J: borehole drill logs; ERT survey with borehole locations; no were found either by drilling or though the ERT survey.

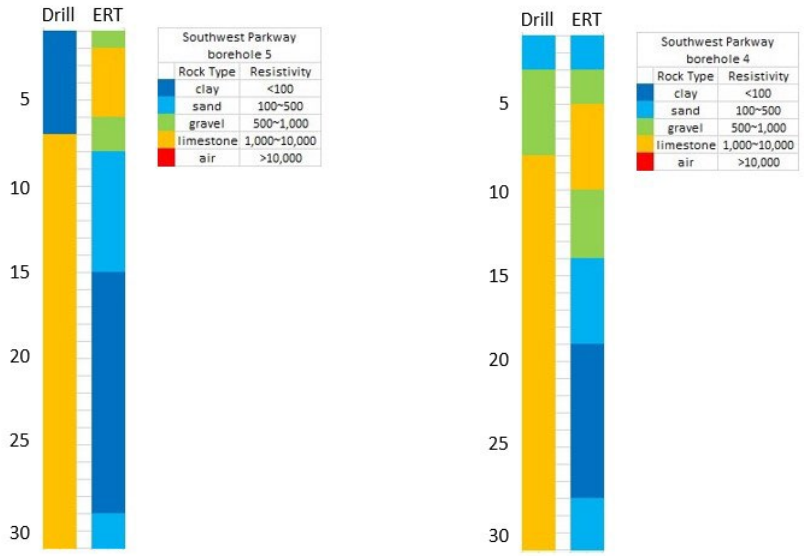

Figure 4.70: Characterization of materials using laboratory tests on cores removed from the boreholes (left column) versus ERT-based characterization.

4.3. Summary of Findings – Field Studies

The key findings from the field studies parallel those drawn from the computational studies using synthetics:

- The ERT returned subsurface images at both sites, based on staggering of 2D slices, which provided indications for the presence of voids. The location of the voids was verified through drilling. However, additional voids were revealed from drilling at locations for which the ERT had not found a void.
- While ERT was able to localize voids, the depth and extent of the voids may not be accurately recovered through ERT.
- Blind correlation of ERT resistivities to materials is challenging, without any prior information.
- Even under ideal site conditions, GPR scans are limited in penetration depth. They could provide indications of subsurface anomalies, but the interpretation is highly subjective and depends on the operator's experience. The GPR findings did not correlate well with the ERT surveys, and, by extension, with the findings of the drilling.
- MASW failed to render subsurface images at both sites: at Georgetown the data were polluted with traffic noise that made inversion impossible, while at the Southwest Parkway site, the presence of heterogeneity in the direction lateral to the array lines also resulted in difficult-to-invert dispersion data. Overall, MASW, as expected, is unsuitable for the detection of subsurface anomalies, since the very theory on which it is based assumes horizontal layering (MASW is effectively a 1D method).
- The field data were not processed using FWI.

Overall, based on these field studies, our experience, and the reviewed litereature, there is no single method among those considered that can guarantee quality subsurface imaging. Of the three methods tested in the field (ERT, MASW, GPR), ERT is the most promising.

Chapter 5. Conclusions and Recommendations

5.1. Conclusions

Subsurface imaging is a challenging problem which, to date, has not admitted a definitive solution, despite substantial advances in all aspects of relevance to the problem. Both the computational and the field studies conducted under the auspices of project 0-7071 confirmed the multifaceted difficulties associated with the detection (is there an anomaly somewhere?), localization (where exactly?), dimensioning (how big?), and characterization (what is it made of?) of subsurface anomalies.

It should be understood that for any method attempting to successfully image the subsurface, it is paramount that the underlying theory on which the method is based be consistent with the field-testing methods and with the software (i.e., the numerical implementation of the method) that is used to process the acquired sensor data. Relaxing any aspect of that tight continuum is a potential source of inaccuracies, inappropriate application, and false findings, and, indeed, this was reaffirmed in our studies (MASW).

While mindful of the need for rapid subsurface imaging in infrastructure projects, to the best of our knowledge, experience, and understanding, there is no single method that could render relatively quickly a fine resolution image of the subsurface, including anomalies, utility lines, and other buried scatterers, in terrains with topographic features, and with a subsurface of arbitrary heterogeneity. This too was reaffirmed in our studies, at least in the context of the four investigated methods.

In summary, we conclude:

- ERT has advantages because of the rapid field deployment. It is an inherently 3D imaging method, and even though robust 3D implementations seem not to be fully developed/available, it holds the best promise for relatively rapid detection (not necessarily of anomaly sizing or material characterization).
- MASW is unsuitable for anomaly detection. It is also unsuitable for subsurface imaging in the presence of heterogeneity.

- GPR may provide an indication of the presence of an anomaly, but definitive characterization of the anomaly is operator-dependent. In our field experiments, GPR scans did not produce voids at the locations where subsequent drilling confirmed their existence.
- FWI is versatile, based, at least, on the 2D computational studies. We expect the finding to hold up for 3D investigations.

5.2. Recommendations

We recommend:

- Of the four methods, and for rapid field investigations, we would suggest the use of ERT, subject to the various caveats already discussed in this report.

The present and, at a minimum, the near-term future of subsurface imaging requires the synergy of methods, and not reliance on a single method. The impetus for this is dictated by field realities, well-understood theoretical limitations, and the current momentum towards multi-physics-based imaging that is fueled by similar reasoning and advances stemming from medical imaging. To this end, we recommend development along the following directions:

- Multi-physics-based imaging
    - Joint inversion based on ERT + FWI
    - Joint inversion based on ERT + microgravity + FWI
    - Inversion based on FWI ambient noise (no need for source characterization, but the site needs to be subjected to diffuse wavefields)

The most critical component of subsurface imaging is the software backend. It is imperative that investment be made to developing software suites that are in tandem with field realities. We recommend software development for:

- 3D FWI, accounting for topographic features
- 3D ERT, accounting for topographic features
- Machine learning-based ERT+FWI inversion

If TxDOT prefers to outsource field investigations, then, in order to ascertain a process of quality contractor selection, we recommend the development of benchmark suites of synthetic subsurface

geologic formations, laden with inclusions either air-filled or soil-filled of different sizes and depths of embedment, for the purpose of exercising contractors' software capabilities in recovering the target subsurface anomalies

5.3. Value of Research

The importance of accurately assessing the composition, the properties, and the overall strength of the near-surface deposits for infrastructure projects has been recognized for hundreds of years. To date, costly and highly localized invasive procedures have dominated the near-surface characterization. Their utility is limited, for they cannot cover an entire site in detail. Thus, increasingly, the interest has been shifting to non-invasive imaging that hold the promise of mapping, and continuously monitor, the subsurface properties for entire sites. But, for non-invasive procedures to become dominant and to eventually replace invasive procedures, their reliability must be proven in the field.

The research reported herein aimed at adding clarity at what can or cannot be expected when using one of the geophysical methods of imaging under consideration by TxDOT. The comparative assessment led to a recommendation of endorsement with caution for ERT, negative recommendations for MASW and GPR, a statement of inconclusiveness for FWI, and suggestions for where future investment and research efforts should be directed. The value of the reported research lies in these recommendations, which are, at a minimum, cost-saving.

References

1. AASHTO LRFD Bridge Design Specifications, Ninth Edition, American Association of State Aki, K. (1957). “Space and time spectra of stationary stochastic wave, with special reference to microtremors.” Bulletin of the Earthquake Research Institute, 35(3):415-456.
2. Alam, Md Iftekhar. "Near-surface characterization using traveltime and full-waveform inversion with vertical and horizontal component seismic data." *Interpretation* 7. (2019): T141-T154.
3. Annan, A. Peter. "Transmission dispersion and GPR." *Journal of Environmental and Engineering Geophysics* 1.B (1996): 125-136.
4. Argote, Denisse L., et al. "Designing the underworld in Teotihuacan: Cave detection beneath the moon pyramid by ERT and ANT surveys." *Journal of Archaeological Science* 118 (2020): 105141.
5. Bharti, Abhay Kumar, et al. "Subsurface cavity detection over Patherdih colliery, Jharia Coalfield, India using electrical resistivity tomography." *Environmental Earth Sciences* 75.5 (2016): 443.
6. Boubaki, Nerouz, Albane Saintenoy, and Piotr Tucholka. "GPR profiling and electrical resistivity tomography for buried cavity detection: A test site at the abbaye de l'Ouye (France)." *2011 6th International Workshop on Advanced Ground Penetrating Radar (IWAGPR)*. IEEE, 2011.
7. Buchen, P. W., and R. Ben-Hador. "Free-mode surface-wave computations." *Geophysical Journal International* 124.3 (1996): 869-887.
8. Cardarelli, Ettore, et al. "Electrical resistivity and seismic refraction tomography to detect buried cavities." *Geophysical Prospecting* 58.4 (2010): 685-695.
9. Carrigan, Charles R., et al. "Electrical resistance tomographic monitoring of CO2 movement in deep geologic reservoirs." *International Journal of Greenhouse Gas Control* 18 (2013): 401-408.
10. Cassidy, Nigel J., Rod Eddies, and Sam Dods. "Void detection beneath reinforced concrete sections: The practical application of ground-penetrating radar and ultrasonic techniques." *Journal of Applied Geophysics* 74.4 (2011): 263-276.
11. Chen, Jianxiong, Colin A. Zelt, and Priyank Jaiswal. "Detecting a known near-surface target through application of frequency-dependent traveltime tomography and full-waveform inversion to P-and SH-wave seismic refraction data." *Geophysics* 82.1 (2017): R1-R17.
12. Claerbout, Jon F., and Francis Muir. "Robust modeling with erratic data." *Geophysics* 38.5 (1973): 826-844.
13. Cox, B. and Wood, C. (2011). Surface Wave Benchmarking Exercise: Methodologies, Results and Uncertainties, GeoRisk 2011: Geotechnical Risk Assessment and Management (C.H. Juang et al., eds.), ASCE GSP 224, pp. 845-852.
14. Crocker, J.A., Arslan, U., Vantassel, J.P., Cox, B.R. (2021). “A Computational Study on the Abilities and Limitations of the Multichannel Analysis of Surface Waves (MASW) Method for Detecting and Resolving Subsurface Anomalies,” in preparation.
15. Daniels, Jeffrey J. "Ground penetrating radar fundamentals." *Prepared as an appendix to a Report to the US EPA, Region V* (2000): 1-21.

16. Daniels, Jeffrey J., James Brower, and Francois Baumgartner. "High resolution GPR at Brookhaven National Laboratory to delineate complex subsurface targets." *Journal of Environmental and Engineering Geophysics* 3.1 (1998): 1-5.
17. Debeglia, N., Bitri, A., and Thierry, P. (2006). "Karst investigations using microgravity and MASW; application to Orléans, France." *Near Surface Geophysics*, 4(4), 215–225. https://doi.org/10.3997/1873-0604.2005046
18. Dey, Abhijit, and H. Frank Morrison. "Resistivity modeling for arbitrarily shaped three-dimensional structures." *Geophysics* 44.4 (1979): 753-780.
19. Di Prinzio, Monica, et al. "Application of GPR to the monitoring of river embankments." *Journal of Applied Geophysics* 71.2-3 (2010): 53-61.
20. Dobecki, Thomas L., and Sam B. Upchurch. "Geophysical applications to detect sinkholes and ground subsidence." *The Leading Edge* 25.3 (2006): 336-341.
21. Dolphin Jr, Lambert T., Robert L. Bollen, and George N. Oetzel. "An underground electromagnetic sounder experiment." *Geophysics* 39.1 (1974): 49-55.
22. Ellis, R. G., and D. W. Oldenburg. "Applied geophysical inversion." *Geophysical Journal International* 116.1 (1994): 5-11.
23. Fathi, Arash, et al. "Three-dimensional P-and S-wave velocity profiling of geotechnical sites using full-waveform inversion driven by field data." *Soil Dynamics and Earthquake Engineering* 87 (2016): 63-81.
24. Fathi, Arash, et al. "Three-dimensional P-and S-wave velocity profiling of geotechnical sites using full-waveform inversion driven by field data." *Soil Dynamics and Earthquake Engineering* 87 (2016): 63-81.
25. Fathi, Arash, Loukas F. Kallivokas, and Babak Poursartip. "Full-waveform inversion in three-dimensional PML-truncated elastic media." *Computer Methods in Applied Mechanics and Engineering* 296 (2015): 39-72.
26. FlashRES Universal User manual (2014) ZZ Resistivity Imaging Pty Ltd, Australia, p 36 1
27. Foti, S. "Multistation method for geotechnical characterization using suface waves Ph. D." *D dissertation, Politecnico di Torino, Italy* (2000).
28. Foti, S., Hollender, F., Garofalo, F., Albarello, D., Asten, M., Bard, P. Y., Comina, C., Cornou, C., Cox, B., Di Giulio, G., Forbriger, T., Hayashi, K., Lunedei, E., Martin, A., Mercerat, D., Ohrnberger, M., Poggi, V., Renalier, F., Sicilia, D., and Socco, V. (2018). "Guidelines for the good practice of surface wave analysis: a product of the InterPACIFIC project." *Bulletin of Earthquake Engineering*, 16(6), 2367–2420.
29. Fowler, J.C., Still, W.L., "Surface and subsurface profiling using ground-probing radar." *Geophysics* 42 (1977), 1502–1503.
30. GAVESHANA GEOSCIENCES PRIVATE LIMITED, http://ggeosciences.weebly.com/
31. Global GPR Services, http://www.global-gpr.com/gpr-technology/how-gpr-works.html. 2010
32. Goodman, Dean, et al. "Correcting for topography and the tilt of ground-penetrating radar antennae." *Archaeological Prospection* 13.2 (2006): 157-161.
33. Goodman, Dean, et al. "Correcting for topography and the tilt of ground-penetrating radar antennae." *Archaeological Prospection* 13.2 (2006): 157-161.

34. Grasmueck, M., and A. Novo. "3D GPR imaging of shallow plastic pipes, tree roots, and small objects." *2016 16th International Conference on Ground Penetrating Radar (GPR)*. IEEE, 2016.
35. Griffiths, D. H., and R. D. Barker. "Two-dimensional resistivity imaging and modelling in areas of complex geology." *Journal of applied Geophysics* 29.3-4 (1993): 211-226.
36. Groves, P., Cascante, G., Dundas, D., and Chatterji, P. K. (2011). "Use of geophysical methods for soil profile evaluation." *Canadian Geotechnical Journal*, 48(9), 1364-1377. https://doi.org/10.1139/t11-044
37. Haskell, Norman A. "The dispersion of surface waves on multilayered media." *Bulletin of the seismological Society of America* 43.1 (1953): 17-34.
38. Hu, Da, et al. "Detecting, locating, and characterizing voids in disaster rubble for search and rescue." *Advanced Engineering Informatics* 42 (2019): 100974.
39. Irnaka, Theodosius Marwan, et al. "Towards 3D 9C Elastic Full Waveform Inversion of Shallow Seismic Wavefields-Case Study Ettlingen Line." *81st EAGE Conference and Exhibition 2019*. Vol. 2019. No. 1. European Association of Geoscientists & Engineers, 2019.
40. Ismail, A., Denny, F. B., and Metwaly, M. (2014). "Comparing continuous profiles from MASW and shear-wave reflection seismic methods." *Journal of Applied Geophysics*, 105, 67-77. https://doi.org/10.1016/j.jappgeo.2014.03.007
41. Ivanov, J. M., Miller, R. D., Park, C. B., and Ryden, N. (2003). "Seismic search for underground anomalies," *SEG Technical Program Expanded Abstracts* : 1223-1226. https://doi.org/10.1190/1.1817502
42. Ivanov, J., Miller, R. D., Lacombe, P., Johnson, C. D., and Lane Jr., J. W. (2006). "Delineating a shallow fault zone and dipping bedrock strata using multichannel analysis of surface waves with a land streamer." *Geophysics*, 71(5), A39-A42. https://doi.org/10.1190/1.2227521
43. Ivanov, J. M., Johnson, C. D., Lane Jr., J. W., Miller R. D., and Clemens, D. (2009). "Near-surface evaluation of Ball Mountain Dam, Vermont, using multi-channel analysis of surface waves (MASW) and refraction tomography seismic methods on land-streamer data." In: *SEG Technical Program Extended Abstracts*, 1454-1458. https://doi.org/10.1190/1.3255123
44. Ivanov, J. M., Miller, R. D., and Peterie, S. (2016). "Detecting and delineating voids and mines using surface-wave methods in Galena, Kansas," *SEG Technical Program Expanded Abstracts* : 2344-2350. https://doi.org/10.1190/segam2016-13967007.1
45. Jazayeri, Sajad, et al. "Reinforced concrete mapping using full-waveform inversion of GPR data." *Construction and Building Materials* 229 (2019): 117102.
46. Jeng, Yih, and Chih-Sung Chen. "Subsurface GPR imaging of a potential collapse area in urban environments." *Engineering Geology* 147 (2012): 57-67.
47. Johnston, Brian, et al. "Detecting voids within a historical building façade: A comparative study of three high frequency GPR antenna." *Journal of Cultural Heritage* 32 (2018): 117-123.
48. Jun Won, Kang. "Characterization of Near-Surface Road Cavity Using an Elastic Wave Full-Waveform Inversion Method." (2017).
49. Kallivokas, L. F., et al. "Site characterization using full waveform inversion." *Soil Dynamics and Earthquake Engineering* 47 (2013): 62-82.

50. Kallivokas, L. F., et al. "Site characterization using full waveform inversion." *Soil Dynamics and Earthquake Engineering* 47 (2013): 62-82
51. Kang, Jun Won, and Loukas F. Kallivokas. "The inverse medium problem in heterogeneous PML-truncated domains using scalar probing waves." *Computer Methods in Applied Mechanics and Engineering* 200.1-4 (2011): 265-283.
52. Karray, Mourad, et al. "Assessment of deep compaction of the Péribonka dam foundation using "modal analysis of surface waves"(MASW)." *Canadian Geotechnical Journal* 47.3 (2010): 312-326.
53. Kasprzak, Marek, and Artur Sobczyk. "Searching for the void: improving cave detection accuracy by multi-faceted geophysical survey reconciled with LiDAR DTM." *Zeitschrift für Geomorphologie, Supplementary Issues* 61.2 (2017): 45-59.
54. Kausel, Eduardo, and Ralf Peek. "Dynamic loads in the interior of a layered stratum: an explicit solution." *Bulletin of the Seismological Society of America* 72.5 (1982): 1459-1481.
55. Kemna, Andreas, et al. "Imaging and characterisation of subsurface solute transport using electrical resistivity tomography (ERT) and equivalent transport models." *Journal of Hydrology* 267.3-4 (2002): 125-146.
56. Khaheshi Banab, Kasgin, and Dariush Motazedian. "On the efficiency of the multi-channel analysis of surface wave method for shallow and semi-deep loose soil layers." *International Journal of Geophysics* 2010 (2010).
57. Knopoff, L. "A matrix method for elastic wave problems." *Bulletin of the Seismological Society of America* 54.1 (1964): 431-438.
58. Kofman, Lev, Amit Ronen, and Sam Frydman. "Detection of model voids by identifying reverberation phenomena in GPR records." *Journal of Applied geophysics* 59.4 (2006): 284-299.
59. Krysiński, Lech, and Jacek Sudyka. "GPR abilities in investigation of the pavement transversal cracks." *Journal of Applied Geophysics* 97 (2013): 27-36.
60. Kucukcoban, Sezgin, and Loukas F. Kallivokas. "Mixed perfectly-matched-layers for direct transient analysis in 2D elastic heterogeneous media." *Computer Methods in Applied Mechanics and Engineering* 200.1-4 (2011): 57-76.
61. LaBrecque, D.J., Morelli, G., Ramirez, A., Dailey, W, and Lundegard, P. "Occam's inversion of 3D ERT data: Proceedings of the International Symposium on Three-Dimensional Electromagnetics." *Ridgefield*, CT (1995): 471-477.
62. LaBrecque, Douglas J., and Xianjin Yang. "Difference inversion of ERT data: A fast inversion method for 3-D in situ monitoring." *Journal of Environmental & Engineering Geophysics* 6.2 (2001): 83-89.
63. Lai, Wallace Wai-Lok, Xavier Derobert, and Peter Annan. "A review of Ground Penetrating Radar application in civil engineering: A 30-year journey from Locating and Testing to Imaging and Diagnosis." *Ndt & E International* 96 (2018): 58-78.
64. Loke, Meng Heng, Ian Acworth, and Torleif Dahlin. "A comparison of smooth and blocky inversion methods in 2D electrical imaging surveys." *Exploration geophysics* 34.3 (2003): 182-187.
65. Luo, Tess XH, and Wallace WL Lai. "GPR pattern recognition of shallow subsurface air voids." *Tunnelling and Underground Space Technology* 99 (2020): 103355.
66. Luo, Tess XH, and Wallace WL Lai. "GPR pattern recognition of shallow subsurface air voids." *Tunnelling and Underground Space Technology* 99 (2020): 103355.

67. Mahvelati, S. and Coe, J. T. (2017). “The use of two-dimensional (2D) Multichannel Analysis of Surface Waves (MASW) testing to evaluate the geometry of an unknown bridge foundation.” In*: Geotechnical Frontiers,* Orlando, FL, United States, 657-666. https://doi.org/10.1061/9780784480441.069
68. Marquardt, Donald W. "An algorithm for least-squares estimation of nonlinear parameters." *Journal of the society for Industrial and Applied Mathematics* 11.2 (1963): 431-441.
69. Martínez-Pagán, P., et al. "The electrical resistivity tomography method in the detection of shallow mining cavities. A case study on the Victoria Cave, Cartagena (SE Spain)." *Engineering Geology* 156 (2013): 1-10.
70. McMechan, George A., and Mathew J. Yedlin. "Analysis of dispersive waves by wave field transformation." *Geophysics* 46.6 (1981): 869-874.
71. Menke, William. *Geophysical data analysis: Discrete inverse theory*. Academic press, 2018.
72. Miller, R. D., Anderson, T. S., Ivanov, J., Davis, J. C., Olea, R., Park, C., Steeples, D. W., Moran, M. L., and Xia, J. (2003). “3-D characterization of seismic properties at the smart weapons test range, YPG.” In: *SEG Technical Program Expanded Abstracts*, 1195-1198. https://doi.org/10.1190/1.1817493
73. Miller, Richard D., et al. "Multichannel analysis of surface waves to map bedrock." *The Leading Edge* 18.12 (1999): 1392-1396.1
74. Miller, Timothy W., et al. "Effects of soil physical properties on GPR for landmine detection." *Fifth international symposium on technology and the mine problem*. 2002.
75. Mohamed, Adel ME, et al. "Site-specific shear wave velocity investigation for geotechnical engineering applications using seismic refraction and 2D multi-channel analysis of surface waves." *NRIAG Journal of Astronomy and Geophysics* 2.1 (2013): 88-101.
76. Monte, Lorenzo Lo. *Radio frequency tomography for underground void detection*. University of Illinois at Chicago, 2009.
77. Nazarian, Soheil, Kenneth H. Stokoe II, and W. Ronald Hudson. *Use of spectral analysis of surface waves method for determination of moduli and thicknesses of pavement systems*. No. 930. 1983. 1
78. Neal, Adrian. "Ground-penetrating radar and its use in sedimentology: principles, problems and progress." *Earth-science reviews* 66.3-4 (2004): 261-330.
79. Neal, Adrian. "Ground-penetrating radar and its use in sedimentology: principles, problems and progress." *Earth-science reviews* 66.3-4 (2004): 261-330.
80. Nguyen, Trung Dung, and Khiem T. Tran. "Site characterization with 3D elastic full-waveform tomography Geotechnical site characterization with 3D FWI." *Geophysics* 83.5 (2018): R389-R400.
81. Nguyen, Trung Dung, Khiem T. Tran, and Michael McVay. "Evaluation of unknown foundations using surface-based full waveform tomography." *Journal of Bridge Engineering* 21.5 (2016): 040160131.
82. Nolan, J. J., Sloan, S. D., Broadfoot, S. W., Mckenna, J. R., and Metheny, O. M. (2011). “Near-surface void identification using MASW and refraction tomography techniques.” In: *SEG Technical Program Expanded Abstracts 2011*, 1401-1405. *Society of Exploration Geophysicists.*

83. Obi, Jeremiah Chukwunonso. "The use of electrical resistivity tomography (ERT) to delineate water-filled vugs near a bridge foundation." (2012).
84. Olayinka, Abel I., and Ugur Yaramanci. "Assessment of the reliability of 2D inversion of apparent resistivity data [Link]." *Geophysical Prospecting* 48.2 (2010): 293-316.
85. Park, C. B. (2005). "MASW – Horizontal resolution in 2D Shear-velocity (Vs) Mapping." Kansas Geological Survey, Lawrence, KS, United States, KGS Open-file Report, 2005.
86. Park, Choon B., et al. "Multichannel analysis of surface waves (MASW)—active and passive methods." *The leading edge* 26.1 (2007): 60-64.
87. Park, Choon Byong, Richard D. Miller, and Jianghai Xia. "Imaging dispersion curves of surface waves on multi-channel record." *SEG Technical Program Expanded Abstracts 1998*. Society of Exploration Geophysicists, 1998. 1377-1380.
88. Park, C. B., Miller, R. D., and Xia, J. (1999). "Multichannel analysis of surface waves." *Geophysics*, 64(3), 800–808. https://doi.org/https://doi.org/10.1190/1.1444590
89. Park, Choon Byong. "Characterization of geotechnical sites by multi-channel analysis of surface waves (mcasw)." KGS Fall 95 (1995): 141-148.1
90. Parker Jr, E. Horry, and Robert B. Hawman. "Multi-channel Analysis of Surface Waves (MASW) in karst terrain, southwest Georgia: Implications for detecting anomalous features and fracture zones." *Journal of Environmental and Engineering Geophysics* 17.3 (2012): 129-150.
91. Pipan, M., et al. "High resolution GPR imaging and joint characterization in limestone." *Near Surface Geophysics* 1.1 (2003): 39-55.
92. Proakis, John G. *Digital signal processing: principles algorithms and applications*. Pearson Education India, 2001.
93. Rahimi, S., Wood, C. M., Coker, F., Moody, T., Bernhardt-Barry, M., and Mofarraj Kouchaki, B. (2018). "The combined use of MASW and resistivity surveys for levee assessment: A case study of the Melvin Price Reach of the Wood River Levee." *Engineering Geology*, 241, 11–24. https://doi.org/10.1016/j.enggeo.2018.05.009
94. Ryden, Nils, and Choon Byong Park. "Fast simulated annealing inversion of surface waves on pavement using phase-velocity spectra." *Geophysics* 71.4 (2006): R49-R58.1
95. Samouëlian, Anatja, et al. "Electrical resistivity survey in soil science: a review." *Soil and Tillage research* 83.2 (2005): 173-193.1
96. Sasaki, Yutaka. "3-D resistivity inversion using the finite-element method." *Geophysics* 59.12 (1994): 1839-1848.
97. Schwab, F. A., and L. Knopoff. "Fast surface wave and free mode computations." *Methods in Computational Physics: Advances in Research and Applications*. Vol. 11. Elsevier, 1972. 87-180.
98. Sensors and Software, "Technical Manual 25: Pulse- EKKO 100 Run. User's Guide v1.2." *Sensors and Software* (1999a), Ontario.
99. Sensors and Software, "Technical Manual 29: PulseEKKO Tools. User's Guide v2.0." *Sensors and Software* (1998), Ontario.
100. Sloan, S. D., Nolan, J. J., Broadfoot, S. W., McKenna, J. R., Metheny, O. M. (2013). "Using near-surface seismic refraction tomography and multichannel analysis of surface waves to detect shallow tunnels: A feasibility study," *Journal of Applied Geophysics*, Vol. 99, pp. 60-65. https://doi.org/10.1016/j.jappgeo.2013.10.004

101. Sloan, S. D., Schwenk, J. T., Stevens, R. H., and Butler, B. W. (2015). "Hazard assessment and site characterization at an oil and gas well site using surface wave methods," *SEG Global Meeting Abstracts* : 114-117. https://doi.org/10.1190/iceg2015-032
102. Smith, James A., et al. "Tunnel detection at Yuma Proving Ground, Arizona, USA—Part 2: 3D full-waveform inversion experimentsTunnel detection at YPG—Part 2: 3D FWI." *Geophysics* 84.1 (2019): B95-B108.
103. Stokoe, Kenneth H., et al. "Characterization of geotechnical sites by SASW method." *Geophysical characterization of sites*. 1994. 1
104. Sullivan, Brian, Khiem T. Tran, and Brian Logston. "Characterization of abandoned mine voids under roadway with land-streamer seismic waves." *Transportation Research Record* 2580.1 (2016): 71-79.
105. Suto, K. and Kristinof, R. (2014). "An MASW survey to assess flood damaged road – A case history." In: Symposium on the Application of Geophysics to Engineering and Environmental Problems, Boston, MA, United States. https://doi.org/10.4133/SAGEEP.27-143
106. Tarantola, Albert, and Bernard Valette. "Generalized nonlinear inverse problems solved using the least squares criterion." *Reviews of Geophysics* 20.2 (1982): 219-232.
107. Tarantola, Albert. "Inverse problem theory: Methods for data fitting and model parameter estimation." *Elsevier*, 1987
108. Thomson, William T. "Transmission of elastic waves through a stratified solid medium." *Journal of applied Physics* 21.2 (1950): 89-93.
109. Topp, G. Clarke, James L. Davis, and AP. Annan. "Electromagnetic determination of soil water content: Measurements in coaxial transmission lines." *Water resources research* 16.3 (1980): 574-582.
110. Tran, Khiem T., et al. "Detection of Embedded Anomalies Using 2-D Full Seismic Waveform Tomography." *Geo-Congress 2014: Geo-characterization and Modeling for Sustainability*. 2014.
111. Tran, Khiem T., et al. "Seismic Waveform Tomography at Test Site with Open Chimneys." Transportation Research Record 2433.1 (2014): 10-17.
112. Tran, Khiem T., et al. "Sinkhole detection using 2D full seismic waveform tomography." *Geophysics* 78.5 (2013): R175-R183.
113. Ungureanu, Constantin, et al. "Use of electric resistivity tomography (ERT) for detecting underground voids on highly anthropized urban construction sites." *Procedia engineering* 209 (2017): 202-209.
114. Van Der Merwe, Andria, and Inder J. Gupta. "A novel signal processing technique for clutter reduction in GPR measurements of small, shallow land mines." *IEEE transactions on geoscience and remote sensing* 38.6 (2000): 2627-2637.
115. Vantassel, J.P., Cox, B.R. (2021). "SWinvert: A workflow for performing rigorous 1D surface wave inversions." *Geophysical Journal International.* https://doi.org/10.1093/gji/ggaa426
116. Wolke, R., and H. Schwetlick. "Iteratively reweighted least squares: algorithms, convergence analysis, and numerical comparisons." *SIAM journal on scientific and statistical computing* 9.5 (1988): 907-921.
117. Xia, Jianghai, Richard D. Miller, and Choon B. Park. "Estimation of near-surface shear-wave velocity by inversion of Rayleigh waves." *Geophysics* 64.3 (1999): 691-700.

118. Xia, J., Chen, C., Li, P. H., and Lewis, M. J. (2004). “Delineation of a collapse feature in a noisy environment using a multichannel surface wave technique.” *Geotechnique*, 54(1), 17-27. https://doi.org/10.1680/geot.2004.54.1.17
119. Xu, Xingxin, et al. "GPR detection of several common subsurface voids inside dikes and dams." *Engineering Geology* 111.1-4 (2010): 31-42.
120. Yang, Xianjin, and Doug J. LaBrecque. "Stochastic inversion of 3D ERT data." *Symposium on the Application of Geophysics to Engineering and Environmental Problems 1998*. Society of Exploration Geophysicists, 1998.
121. Yi, Myeong-Jong, et al. "Three-dimensional imaging of subsurface structures using resistivity data." *Geophysical Prospecting* 49.4 (2001): 483-497.
122. Yoon, S., and Rix, G. J. (2009). “Near-Field effects on array-based surface wave methods with active sources.” *Journal of Geotechnical and Geoenvironmental Engineering*, 135(3). https://doi.org/10.1061/(ASCE)1090-0241(2009)135:3(399)
123. Zhang, Shuang X., et al. "Apparent phase velocities and fundamental-mode phase velocities of Rayleigh waves." *Soil Dynamics and Earthquake Engineering* 23.7 (2003): 563-569.1
124. Zhao, Wenke, Emanuele Forte, and Michele Pipan. "Texture attribute analysis of GPR data for archaeological prospection." *Pure and Applied Geophysics* 173.8 (2016): 2737-2751.
125. Zhao, Wenke, et al. "Advanced GPR imaging of sedimentary features: integrated attribute analysis applied to sand dunes." *Geophysical Journal International* 213.1 (2018): 147-156.
126. Zhou, Wanfang, B. F. Beck, and J. B. Stephenson. "Reliability of dipole-dipole electrical resistivity tomography for defining depth to bedrock in covered karst terranes." *Environmental geology* 39.7 (2000): 760-766.
127. Zywicki, D.J. (1999). Advanced signal processing methods applied to engineering analysis of seismic surface waves. Ph.D. Dissertation, School of Civil and Environmental Engineering, Georgia Institute of Technology, Atlanta, GA